

# DEPARTMENT OF GEOSCIENCE

## MS Thesis Defense

**TITLE: Sensitivity of Imaging to Seismic Anisotropy-Maljamar-Vacuum Field, NM**

**NAME: Marija Djordjevic**

**RESEARCH COMITEE: Advisor: Kurt J. Marfurt**

Members: John Castagna, De Hua Han and Kevin Bishop (BHP)

### **Abstract**

Although anisotropy has been recognized by rock physicists for almost a century, the simpler, isotropic earth model has served us well in imaging the subsurface. Recently our ability to estimate isotropic velocities has advanced to the point where the secondary, anisotropic effects become important. Anisotropic effects become more important with larger angles of wave propagation as measured from the earth's surface. For shallow targets, such as the Grayburg seen at 0.7 s in the Maljamar survey acquired in the Delaware Basin, NM, 'long offset' is defined as 3350m where the isotropic stretch-mute would normally be applied.

Overburden anisotropy may be either intrinsic (due to anisotropic shales), or effective (due to heterogeneous velocity layered overburden). Little attention has been paid to anisotropy in the Permian and Delaware Basins. The Maljamar survey is most challenging to process, being plagued with strong ground roll, air waves, and head waves, all of which are backscattered in 3-D. Velocities are very difficult to pick, and the estimation of the anisotropic parameter ? even more difficult.

The major impact of accounting for anisotropy is to increase the fold of the data in the shallow target, thereby increasing the signal to noise and the vertical and lateral resolution of the resulting image.

I quantify this improved lateral resolution through a suite of time and horizon slices through the seismic and attribute volumes.

# 1. INTRODUCTION

## 1.1. Maljamar-Vacuum Field

Maljamar-Vacuum field is positioned on the northwest shelf of the Delaware Basin, in Lea County, southeast New Mexico (Figure 1.1). The entire area is part of the Permian Basin of Southeastern New Mexico and West Texas (Roche, 1997).

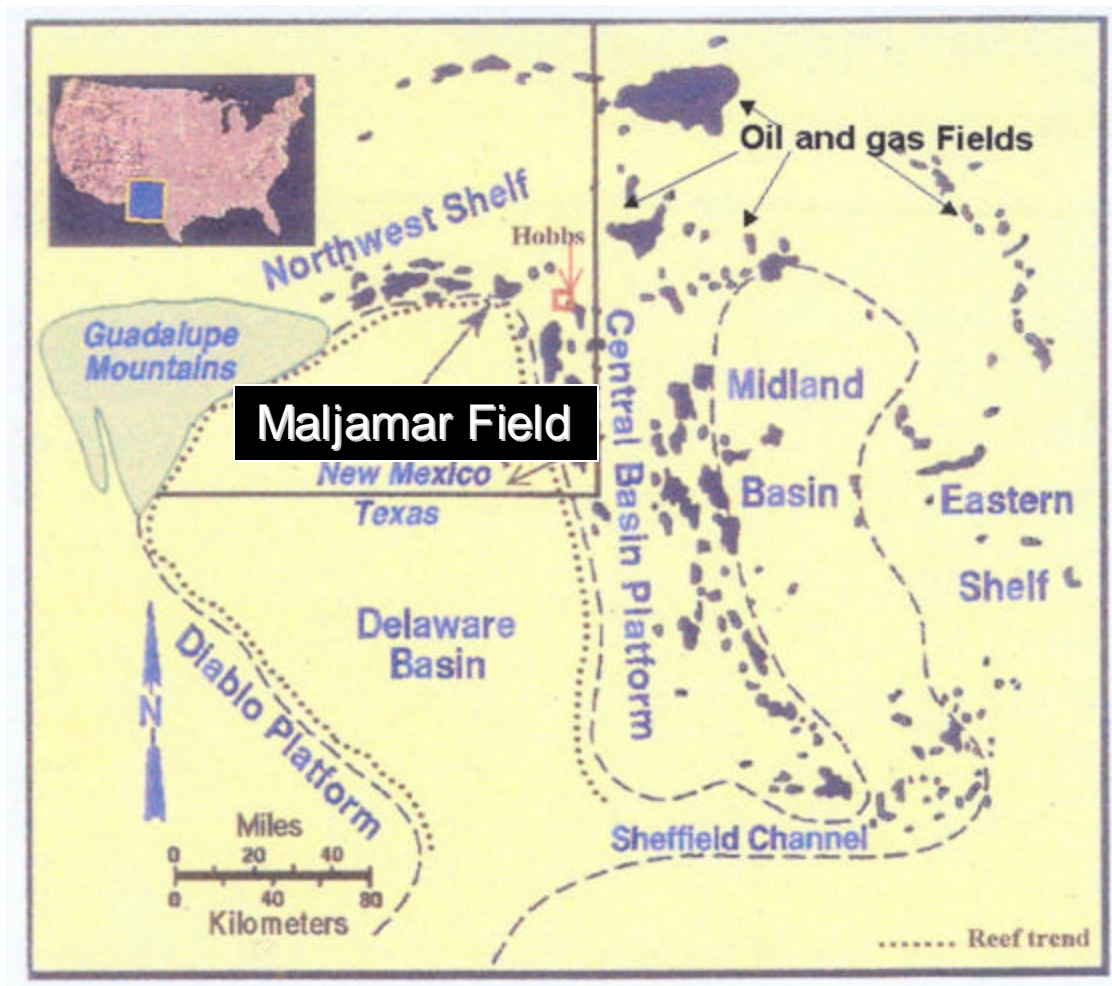


**FIG. 1.1.** Regional map showing geological location of Maljamar-Vacuum field and structural provinces of the Permian Basin. Black spots indicate oil and gas fields producing from the different units in the Permian basin (after Acuna, 2000).

Maljamar-Vacuum field belongs to larger system of oil fields in the Permian basin. It was discovered in 1929 by Socony Vacuum Oil Company. Production began in 1937 (Pranter, 2004, Amaral, 2001) and by 1994 the field produced the 600 MMBO and 800 BCFG from 2400 completions (Blaylock, 1999). Due to improvements in recovery technology, Texaco decided to implement two CO<sub>2</sub> injection programs along with time-lapse multicomponent seismic surveys; one in 1995 and another in 1998. This method proved effective in the secondary recovery (Amaral, 2001).

The field sediments are mainly Paleozoic carbonates with periodic siliciclastic and evaporate deposition dating from Ordovician through Permian age with the thickness exceeding 9 km in the Southern Delaware Basin (Roche, 1997). The majority of the production from Maljamar-Vacuum field comes from the Permian carbonates located in structures, most common by closed folds caused by the late Permian deformation. The producing structure, predominantly Guadalupian dolomites in the Grayburg and San Andres Formations (Figure 1.2) are covered with almost undeformed Permian and Mesozoic formations. The Grayburg-San Andres interval has a maximum gross pay of 200 m in thickness and produces from depths of 1.1-1.4 km. (Blaylock, 1999, Hills, 1984).

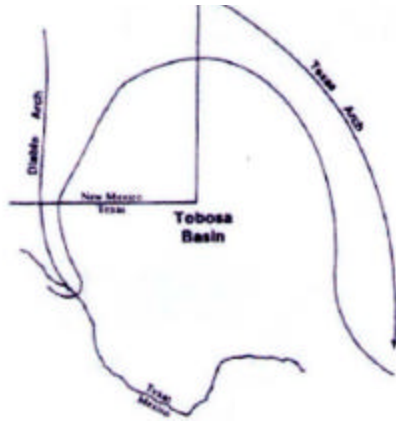
Era	Period	Epoch	Formation		General Lithology	Approximate Thickness (ft)		
			Northwest Shelf	Delaware Basin				
Paleozoic	Permian	Ochoan	Dewey Lake		Redbeds / Anhydrite	200–400		
			Rustler		Halite	100		
			Salado		Castile Anhydrite	Halite / Anhydrite	1000	
		Guadalupian	Artesia Group	Capitan	Tansill	Bell Canyon	Anhydrite / Dolo.	200
					Yates		Ss Sh / Anhydrite	200
					Seven Rivers		Dolomite / Anhydrite	500
					Queen		Goat Seep	Sandy Dolomite / Anhydrite / Shale
			Grayburg	Delaware Mountain Group	Cherry Canyon	Dolomite / Anhy. / Shale / Sandstone	300	
			<b>San Andres</b>			Dolomite / Anhydrite	1500	
			Glorieta			Brushy Canyon	Sandy Dolomite	100
			Leonardian	Yeso	Victoria Peak	Bone Spring	Dolo. / Anh. / Ss.	1500
		Abo				Dolo. / Anh. / Sh.	1000	
		Wolfcampian		Wolfcamp		Limestone / Dolo.	0–1500	
		Pennsylvanian	Virgilian	Cisco		Limestone / Ss.	0–1250	
			Missourian	Canyon		Limestone / Sh.		
	Des Moinesian		Strawn		Limestone / Ss.	0–750		
	Atokan		Bend		Lime / Ss. / Sh.	0–1250		
	Morrowan		Morrow		Lime / Ss. / Sh.			
	Mississippian				Limestone / Sh.	0–800		
	Devonian				Dolomite / Chert	0–1200		
	Silurian		Fusselman		Dolomite / Chert			
	Ordovician	Upper	Montoya		Dolomite / Chert	0–400		
		Middle	Simpson		Lime / Ss. / Sh.	0–200		
Lower		Ellenburger		Dolomite	0–400			
Cambrian				Sandstone				

FIG. 1.2. Stratigraphic column of the main geologic formations at or near Maljamar-Vacuum field. Red dots represent predominant producing structures (after Pranter et al., 2004).

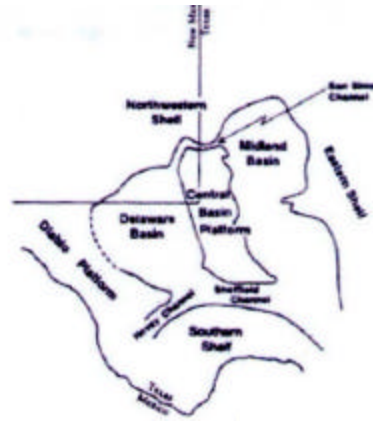
## 1.2. Structure and tectonics

The structure of Maljamar-Vacuum field is influenced by the structural history of the Permian Basin. From Ordovician through Devonian period during the minimum tectonic activity, this area was a shallow marine sea known as Tobosa basin (Figure 1.3a) and it extended along the southwest margin of the North American plate.

(a) Early Paleozoic



(b) Early Permian



(c) Late Permian

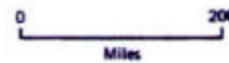
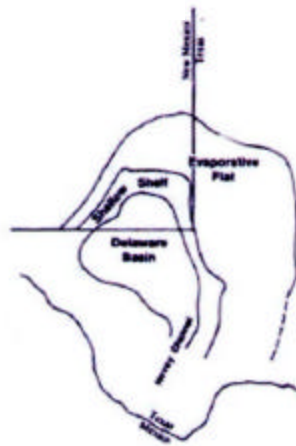


**FIG. 1.3.** Evolution of Permian Basin, from Early Paleozoic to the Late Permian (after Amaral, 2001).

During this period, carbonates, shales and clastic sediments were cyclically deposited in the basin. The presence of transgressions and regressions is seen as unconformities in wellbores, surface outcrops and seismic sections (Roche, 1997). The early Mississippian was characterized by the presence of slight uplift and erosion. The most important fact is the repeated accumulation of large amounts of organic-rich materials in the deep, poorly ventilated, marine basin. The Ordovician Simpson Group and the Mississippian Woodford Shale, 30-200 m thick, became the source rocks for the hydrocarbons in the area (Amaral, 2001).

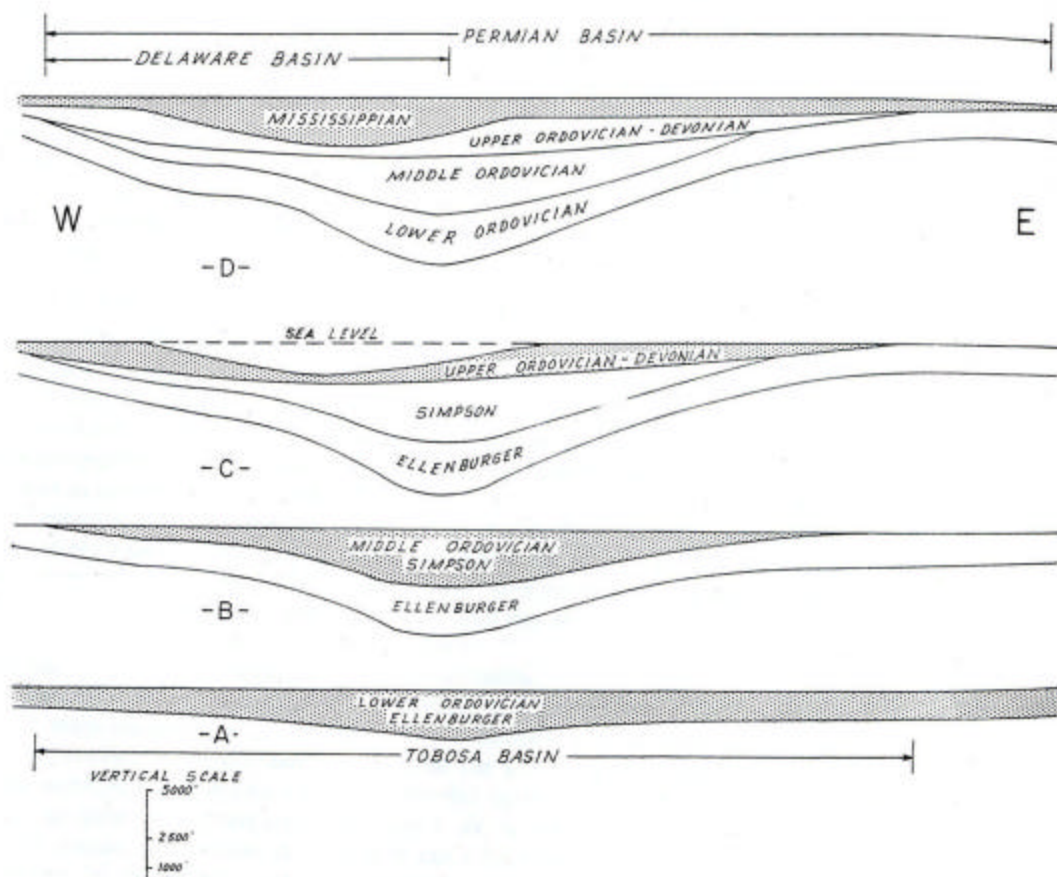


**FIG. 1.4.** Cross-section of the Permian Basin (after Adams, 1965).

The late Paleozoic was a time of great change in sedimentation, beginning with carbonate deposition during the Middle Mississippian and significantly increased tectonic

activity during the Late Mississippian and Pennsylvanian. By late Mississippian the Tobosa basin had up to 2 km of sediments on its deepest parts (Adams, 1965) (Figure 1.4). The South American plate converged with the southern margin of the North American plate. Pennsylvanian compressional forces from the southwest raised the Central Basin ridge along the steeply dipping reverse faults at the axis of Tobosa basin, forming secondary basins known as the Delaware and Midland Basins (Figure 1.3b). After that point, the Pre-Mississippian Tobosa Basin was destroyed (Talley, 1997). A northwest-southeast trending fault zone separated the Delaware Basin and Central Basin Platform and extended as a strike slip fault with right lateral movement into the Maljamar-Vacuum Field area (Figure 1.5). Pennsylvanian tectonic activity increased the number of well-defined carbonate shelves along the Delaware Basin margins controlled by extensive fault planes with left lateral and vertical displacement (Talley, 1997).

The relative changes in the sea level, tectonism and siliciclastic input dictated the cyclic regime of sedimentation. In contrast to the thin amounts of sediments from Pennsylvanian period, Permian accumulated 2.5 km of deposited sediments. A great many thin limestones were deposited during the early Permian (Wolfcamp) and a large amount of organic material was preserved. The middle Permian (Leonardian) saw a continuation of deposition of fine grained clastic sediments and thinner sandstone beds, particularly in the central parts of the Delaware basin. In restricted lagoons evaporate deposition was starting to develop. By the end of the middle Permian (Leonardian), Wolfcamp beds were deeply buried (900 m) and the production of kerogen began.

During the late Permian, new space for sediments became available in the Delaware Basin area through regional subsidence and tilting towards the axis of the old Tobosa Basin (Figure 1.3c) (Amaral, 2001). This period was marked with 300 m thick sediments of Guadalupian sands and silts rich in preserved organic content. Earlier Permian deposited materials were already transformed to hydrocarbons. The major reservoir in Maljamar-Vacuum field comes from Guadalupian sediments, particularly the San Andres Formations, carbonate shelf composed of dolomites interbedded with dolomitic siltstones (Amaral, 2001). The Ochoan, the last sequence in the Permian, is characterized by limestones and dolomites, later capped by fine red clastics.

At the end of the Permian, the Delaware basin was filled with evaporate, forming an almost impermeable 600 m thick sedimentary blanket which cut off vertical fluid migration, such that most of the fluids escaped laterally into the existing traps.

The end of the Paleozoic saw the end of large deformations in the Permian Basin. However, the late Permian carbonates and evaporates are evidence of the intense faulting and folding during the Pennsylvanian and Early Permian. The circulation of saturated brines from the evaporate lagoons helped develop dolomitization.

The significant tectonic activity throughout the Permian created a pattern of faulting and fractures which facilitated diagenesis and hydrocarbon migration. (Roche, 1997, Hills, 1984, Amaral, 2001). The presence of faulting in the Guadalupian age had a big impact on the present day reservoir condition of the Permian Basin San Andres formation. Evidence of karstification was found in cores and seismic data (Talley, 1997).

The sediments deposited during the periods after the Permian comprises terrestrial clastics derived from Triassic subsidence, such as lower Cretaceous sandstones and limestones and upper Cretaceous shale and flagstone (Amaral, 2001).

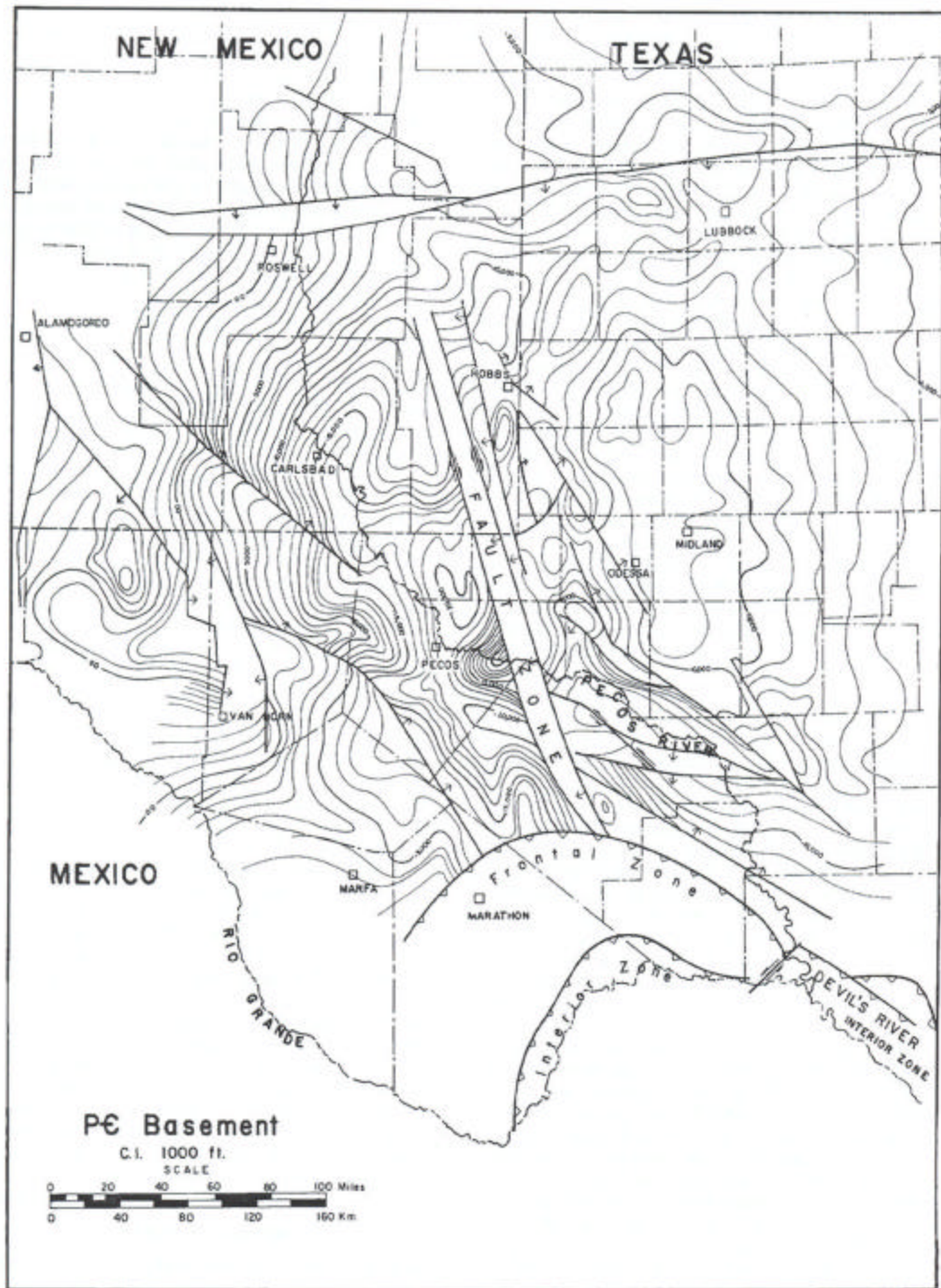


FIG. 1.5. Contour map showing present configuration of Precambrian basement (after Hills, 1984).

### 1.3. Previous work and motivation

The Permian Basin contains complex tectonic structures rich in hydrocarbons and it has long been a prime target for the oil industry. There has been considerable research devoted to this area, especially from the Colorado School of Mines in connection with their Reservoir Characterization Project addressing secondary recovery of the field. Roche (1997) did time-lapse, multi-component, 3D seismic characterization of a San-Andres shallow shelf carbonate reservoir, Talley (1997) worked on San Andres formation attribute analysis and he investigated S wave anisotropy. DeVault and Mattocks (1998) worked on 3D seismic prestack multicomponent analysis and shear wave influence on anisotropy from the borehole. Acuna (2000) published work about the water flood monitoring and 4D multicomponent seismic characterization, Wehner (2000) and others published an article about dynamic reservoir characterization which explained how fractures introduced seismic anisotropy into a reservoir. Galikeev and Ota (2001) worked on attribute analysis of the field and integrated seismic analysis of the Atoka formation, while Amaral (2001) concentrates on shear wave azimuthal AVO analysis. All of the mentioned authors: Talley, Amaral, Wehner and Mattocks investigated anisotropy due to the fracturing induced by CO<sub>2</sub> injection. Since, Vacuum field is characterized and by presence of shale, my idea is to examine what the influence of vertical transverse isotropy (VTI) has on seismic imaging and velocity estimation.

The idea of this thesis is not to try some new techniques for processing, but to get better results with more accurate velocity analysis, on the basis of provided data. In particular I will try to improve the lateral resolution by including the influence of VTI.

Due to large amount of noise, reflections are very often masked, especially on the near offsets. The most recent reprocessing on the part of the particular field that I am working on was undertaken by Geotrace for ConacoPhilips. The area is very noisy and the correct velocity is very difficult to pick.

## 1.4. Data

The seismic volume that forms the basis of this thesis was provided to AGL by ConocoPhillips. It is a 3D land seismic survey acquired over Maljamar-Vacuum Field by Dawson Geophysical in spring 1994 and covers approximately 900 km<sup>2</sup>. The western part of the survey is labeled as Maljamar. The Maljamar survey represents a regional overview of the Permian shelf margin at Vacuum. We do not have enough reliable well information to establish an accurate velocity model of the area. The first processing was done by Fairfield Industries in 1999. The eastern part of the data set was reprocessed recently by a contractor achieving good results (Clinton, 2005) but it did not include the Maljamar part.

The survey was shot using a vibroseis source and recorded 3 s of two way travel time sampled at 2 ms. The seismic data grid was laid out with North-South crosslines and East-West inlines. Source lines are perpendicular to the receiver lines. Each source line is half the distance between station and is offset from the receiver lines by 34 m. Source line direction is East-West with the source line spacing of 470 m, while receiver lines are perpendicular heading North-South with 403 m spacing (Figure 1.6 and Figure 1.7). The nominal fold was 36 with a CDP bin size of 34 x 34 m. The survey consisted of a total of 58 receiver lines/ 8779 receivers and 34 source lines/7100 sources, with 252-864 active channels for any give source. The data acquisition parameters are listed in Table 1.1 (Clinton, 2005).

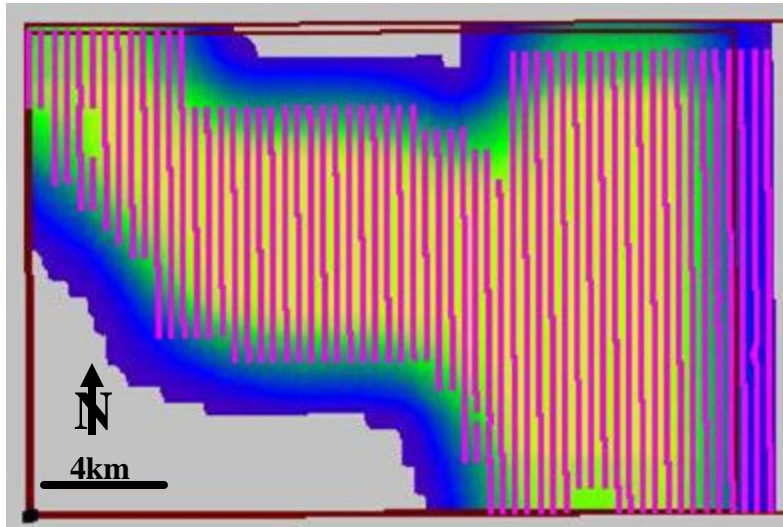


FIG. 1.6. Receiver positions of Maljamar-Vacuum survey.

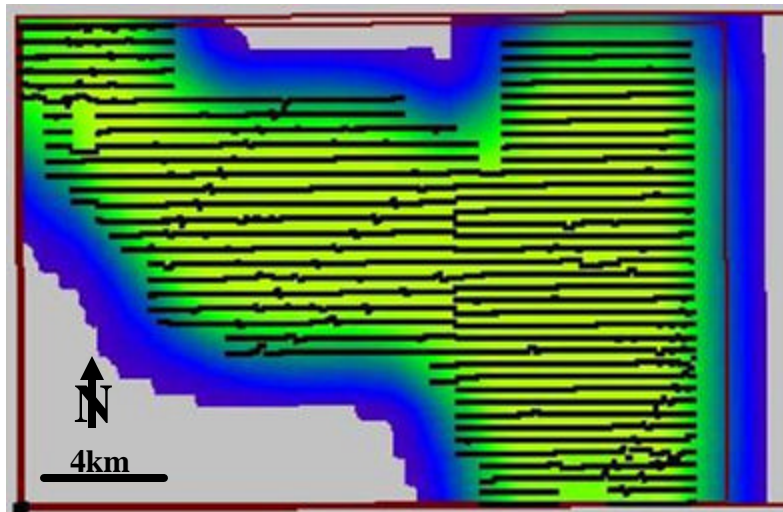


FIG. 1.7. Shot positions of Maljamar-Vacuum survey.

Shot interval in m	67
Group interval in m	67
Receiver line spacing in m	403
Shot line spacing in m	470
Bin size in m	34
Fold of coverage	36
Sampling interval in ms	2
Maximum time in ms	3072
Number of prestack traces	5142132
Data volume in gigabytes	34
Number of channels	252-864
Source	Vibrators
Sweep length in s	12
Sweep frequency in Hz	8-90

**Table 1. 1.** Data Acquisition Parameters.

My biggest challenge in reprocessing this data set was the incomplete shot/receiver (S/R) header information. The seismic data were delivered to the AGL on two SEG Y tapes together with the observer logs on the microfiche. It was claimed that the data came with the geometry, but the headers contained only X and Y coordinates of shots and receivers, shot and CDP numbers and CDP inlines and crosslines. This resulted in many unsuccessful attempts to load the data into Focus. The geometry problem was not solved, although employees from ConocoPhillips told me that they did not encounter any problems when they loaded the same data set onto their system (Clinton, 2005). This is because ConocoPhillips software does not require the inline, crossline and bin numbers that Paradigm's Focus software does. I am deeply indebted to the Research & Development Group from Paradigm Geophysical who helped solve this geometry problem. The results of this multi-month effort are images of the receiver (Figures 1.6) and source (Figures 1.7) locations. I display the fold map of the survey in Figure 1.8.

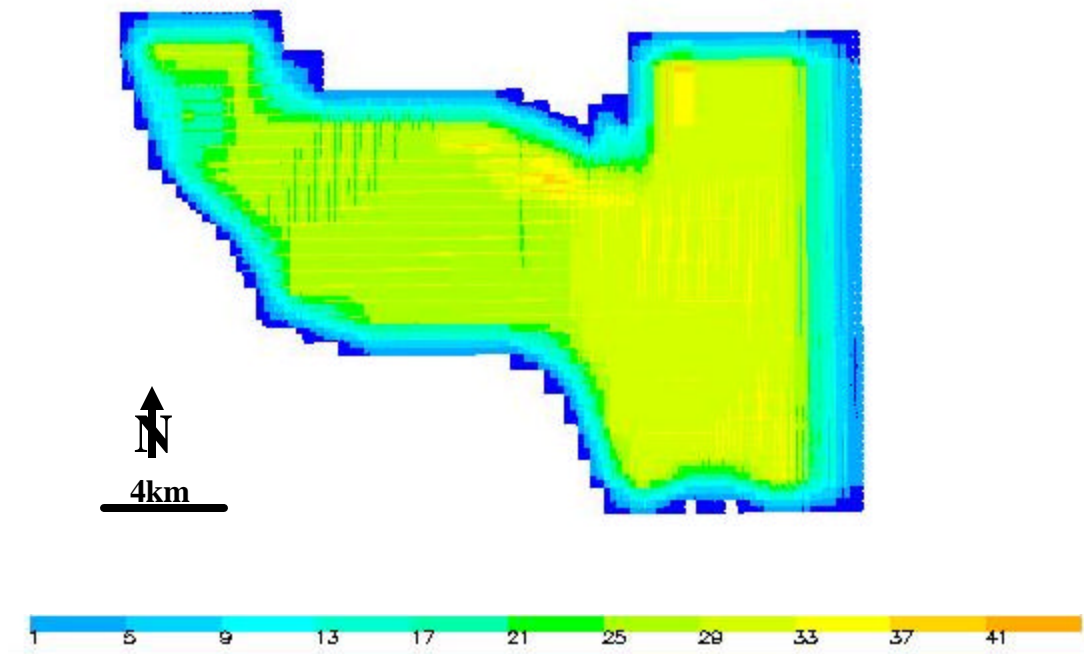


FIG. 1.8. Maljamar-Vacuum fold map.

## **2. SEISMIC DATA PROCESSING**

### **2.1. Introduction**

The basic purpose of this chapter is to highlight all steps in the processing flow that were applied on the Maljamar-Vacuum 3D data set. The processing flow was implemented using the Focus 2D/3D/DISCO and Geodepth seismic processing packages made available to UH by Paradigm Geophysical. These algorithms were augmented by the Colorado School of Mines Seismic UNIX (SU) and the Stanford University's Stanford Exploration Project (SEP) suite of routines. While it is common for graduate students to reprocess 2D data with commercial software and 3D data with specialized university software to highlight a key development like migration, it is uncommon for graduate students to process a complete 3D survey from definition of geometry through to interpretation. Indeed, most 3D processing is done by processing specialists, either in an oil company, or more commonly, in a service company. In my case, I needed to master geometry QC, 3-D time processing, prestack migration, data loading, modern attribute calculation and seismic interpretation.

Since the major goal of my thesis is to evaluate the impact of seismic velocity analyses on 3D interpretation, and on vertical and lateral resolution in particular, I have taken care to document my processing flow so that other students can follow exactly what was done to the data.

The most important processes in the processing sequences of this field, as in the most of the land data, were: static corrections, noise reduction and amplitude recovery. I show my flow in Table 2.1.

<b>General Processing Sequences</b>	<b>Details of Application</b>
Geometry preparation	Assigning the geometry
Shot gathers and CMP gathers	Checking spherical divergency and datum statics, surface consistent deconvolution, filtering of ground roll
Velocity analysis (100 x 100 CMP's)	AGC, filter, supergathers
Residual static corrections	
Velocity analysis (50 x 50 CMP's)	
Anisotropy velocity	3D supergathers, fx decon, filtering, muting, picking of ?
Prestack isotropic migration	
Prestack anisotropic migration	
Volumetric attribute calculation	Coherence, curvature
Data loading	Conversion of formats, load into Geoframe
Interpretation	Pick Grayburg and other key horizons

**Table 2.1.** Work flow.

## **2.2. Preprocessing**

The first challenge in the Maljamar-Vacuum dataset was the fact that that I did not have enough information about the processing already applied to the data prior to delivering it to the AGL. The operator obtained a copy of the prestack data. However, details of the processing flow were lost due to tape format changes, company mergers and personnel change. In order to find out what was applied, I had to test different parameters.

### 2.2.1. Spherical Divergence

The first thing I noted when I plotted the data (Figure 2.1) was the fact that wave strength did not decrease with time, due to geometric spreading, absorption and loss at interfaces by reflection (Sheriff, 1984). The shot gathers on deeper events have even stronger amplitudes. My conclusion is that a gain recovery function was applied to correct for the amplitude effects of spherical wavefront divergence (Yilmaz, 2001).

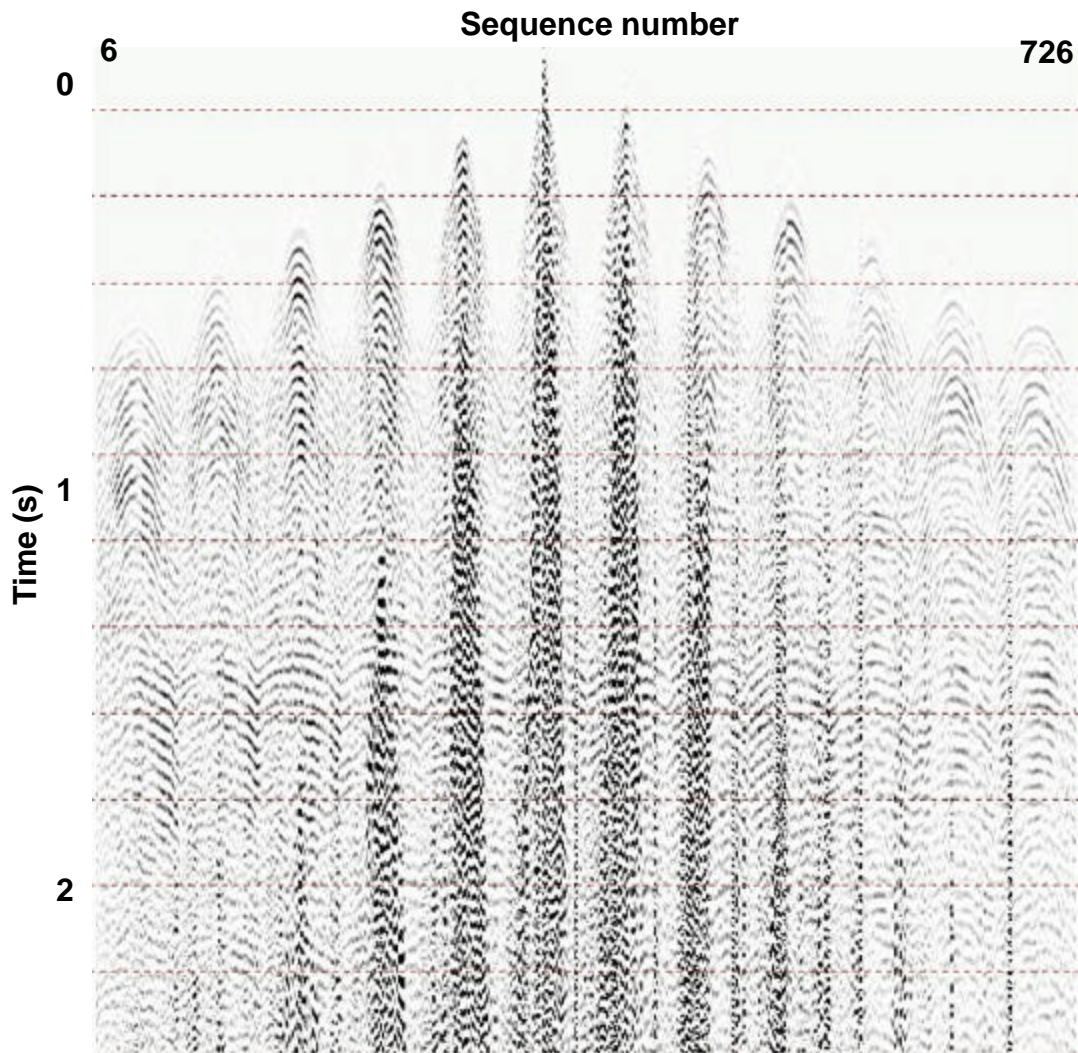


**FIG. 2.1.** “Raw” shot gather with applied spherical divergence.

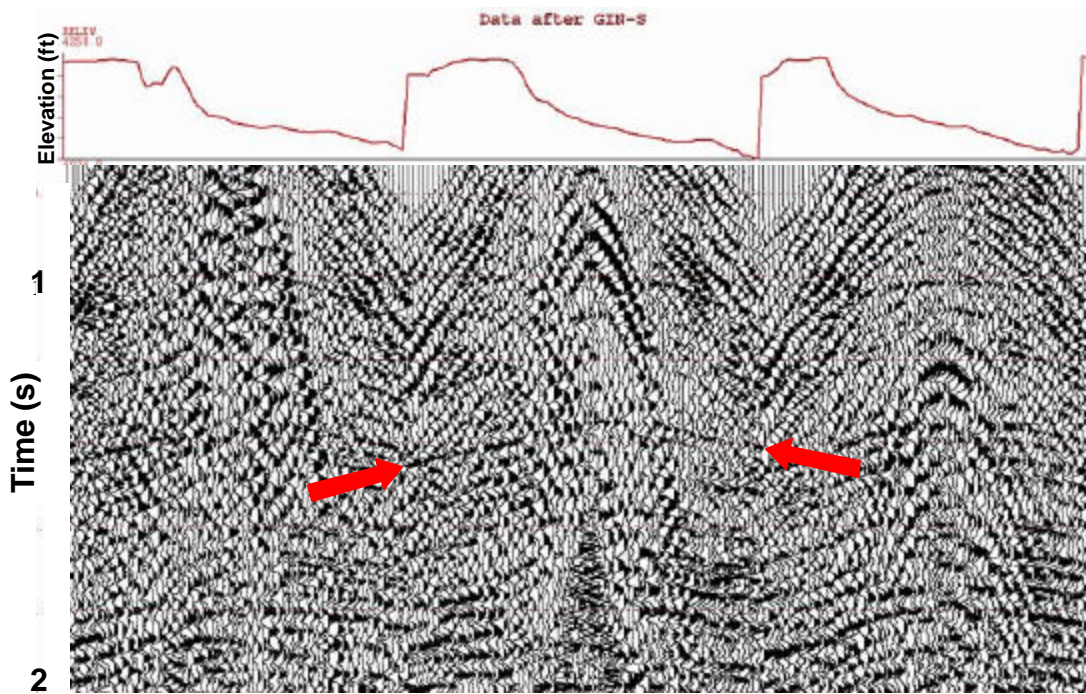
### 2.2.2. Geometry

The next step was to merge the field geometry with the seismic data coordinates of shots and receivers that should be stored on the headers. The rule is that any change of the geometry should be reported in the observer log, but I did not have any of that information (Yilmaz, 2001). I attempted to define the geometry database, even with additional help from friends and colleagues at Paradigm Geophysical I encountered problems in receiver gathers and applying surface consistent statics. Clearly, my geometry was still wrong. As Yilmaz says: “Many types of processing problems arise from setting up the field geometry incorrectly”. I firmly attest to this truth. At the end of the “day” (figuratively speaking, in actuality it was several months), Edip Baysal and his colleagues at Paradigm Geophysical were able to write some clever “one-off” code to reconstruct the missing information.

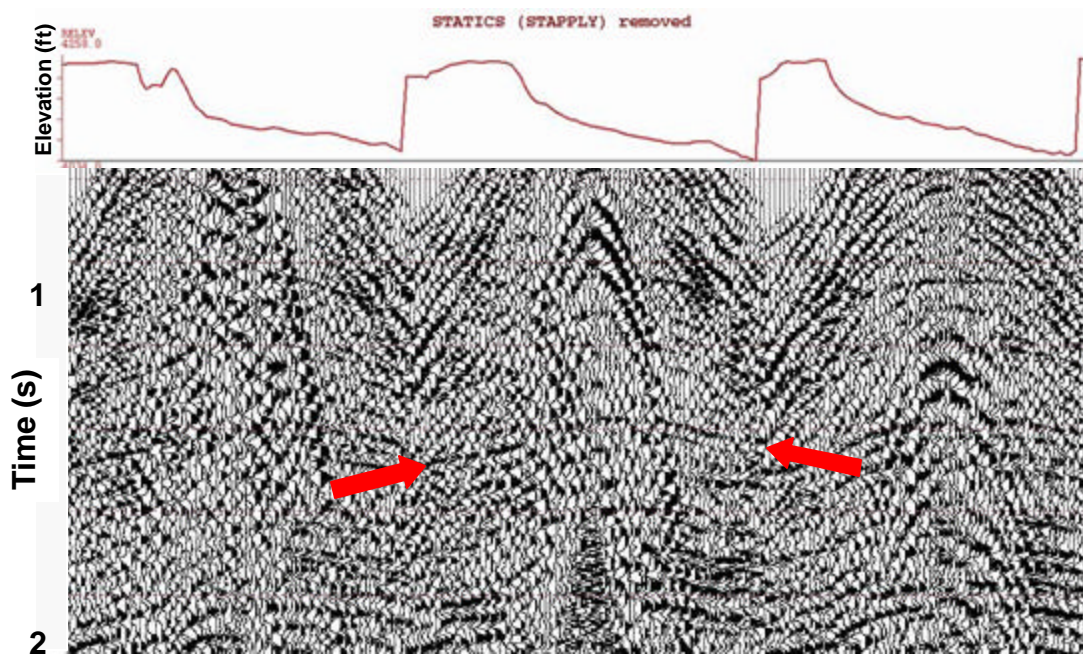
### 2.2.3. Datum Corrections

Since reflection travel times are influenced by near-surface distortions (Yilmaz, 2001), it is important for land data processing to apply the static corrections on the data before continuing with further processing. Sheriff (1984) defines statics as “corrections applied to seismic data to compensate for the effects of variations in elevation, weathering thickness, weathering velocity, or reference to a datum”. For time processing, the travel times should be reduced to a common datum level (Yilmaz, 2001). The accuracy and quality of stacking velocity computations and CMP sections depends very much on these time corrections (Taner et al., 1974).

The data headers from Maljamar-Vacuum field contained information about the datum static corrections in the range of 30-40 ms, and according to the SEG-Y standards, the header value for total statics should be 0 if no static has been applied (Barry et al., 1974). Also, when I compare the data from a shot gather with and without the static value, we can see the correlation with the surface elevation (Figure 2.2). For this reason, I deduced that the datum statics had already been applied.



(a)



(b)

**FIG. 2.2.** Shot gather (a) with and (b) without statics applied. Note how the reflection indicated by arrow is more continuous and hyperbolic on (a).

### 2.3. Common Midpoint Sorting

Signal enhancement and noise suppression is the main goal in seismic processing. Data redundancy using the multiple ground coverage method provides the leverage (Neidell et al., 1980) and is necessary for accurate velocity determination.

Seismic data acquisition is done in shot-receiver coordinates, while many seismic data processes are carried out in midpoint-offset coordinates (Figure 2.3).

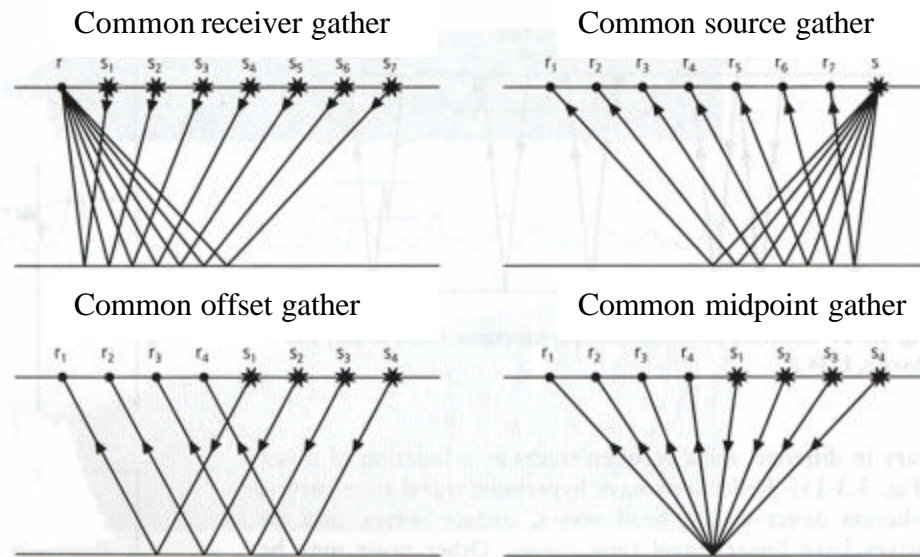
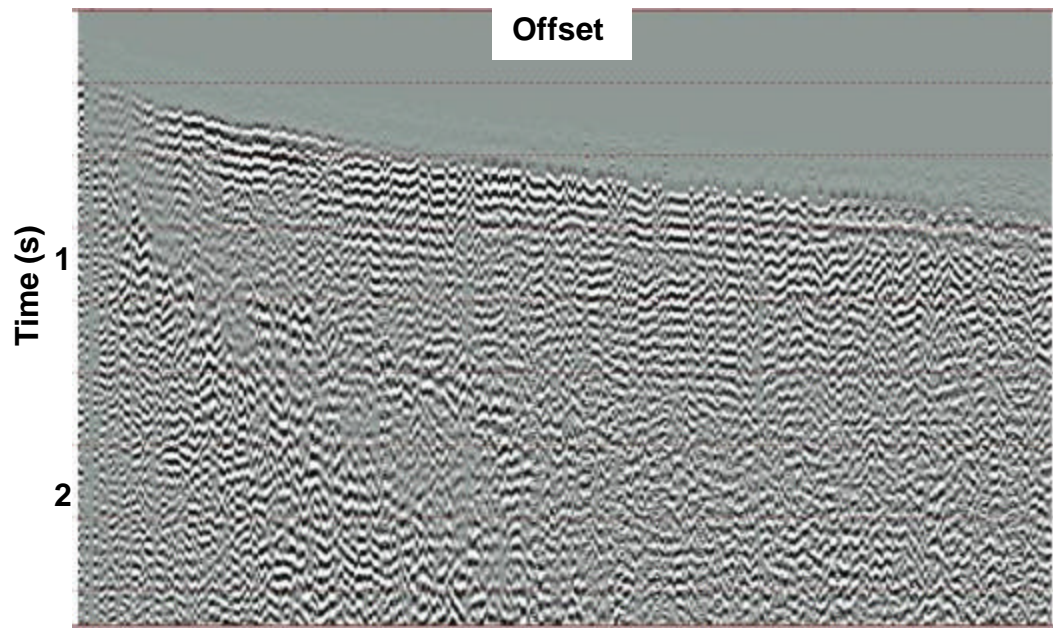


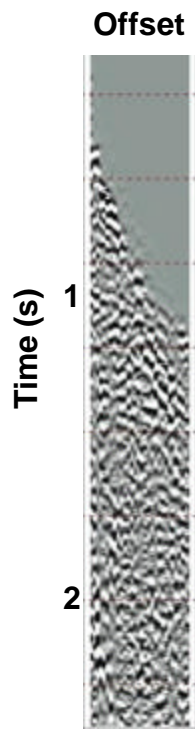
**FIG. 2.3.** Different kind of sorting the traces (after Stein et al., 2003).

To achieve the coordinate transformation, based on the field geometry, each trace is assigned to the midpoint location, halfway between the source and the receiver in the flat-layered geometry, and the traces with the same midpoint location are grouped together to form a common midpoint, or CMP, gathers. This process is called sorting. CMP gathers, consisting of a set of traces with different offsets, sample the same subsurface point and thus enhance the strength of reflected arrivals (Yilmaz 2001, Stein et al., 2003).

In the Maljamar-Vacuum survey each CMP gather contains approximately 36 different traces (the fold=36). I sorted the data from shot to CMP gathers (Figure 2.4).



(a)



(b)

**FIG. 2.4.** Sorting from a representative (a) shot gather to a representative (b) CMP gather.

## 2.4. Velocity analysis

I used conventional semblance analysis (Taner et al., 1969) of CMP gathers to estimate velocity. Stacking velocity determination works on common mid point trace gathers defined using Dix's hyperbolic move-out equation:

$$t_x^2 = t_0^2 + x^2/V_{nmo}^2, \quad (2-1)$$

where:  $t_x$  = two-way arrival time,

$t_0$  = two-way normal incidence time,

$X$  = offset distance, and

$V_{nmo}$  = stacking velocity.

For each guess of  $V_{nmo}$ , the data are vertically shifted by a time  $t_x$ , after which the semblance is calculated across all traces in the gathers within a vertical analysis window (Figure 2.5). These semblance "spectra" are plotted and picked by the seismic processor.

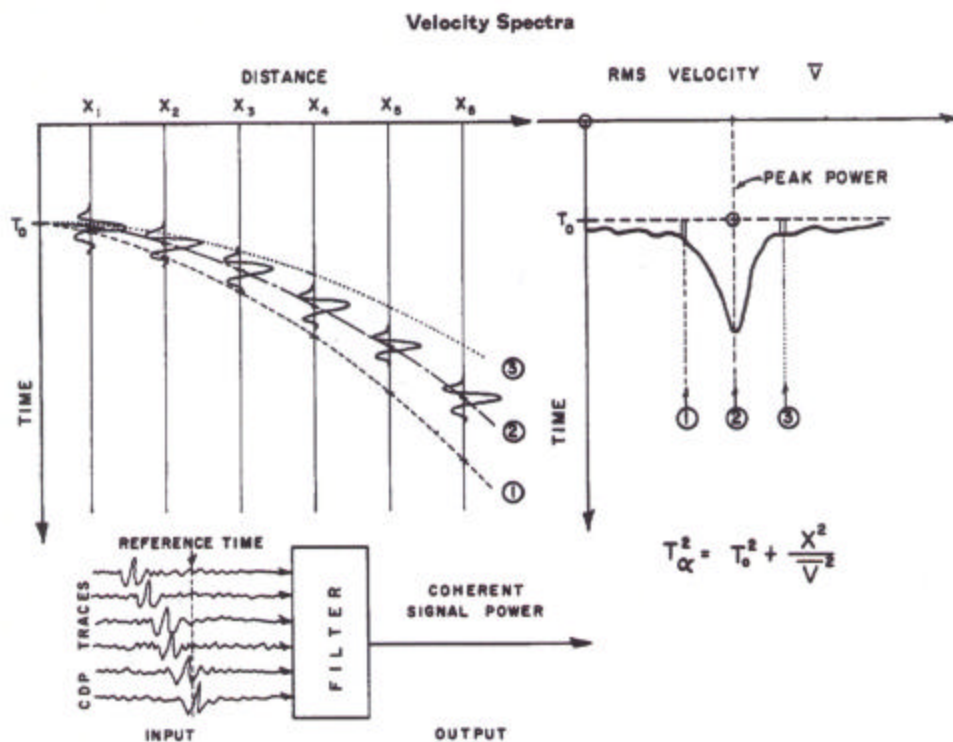


FIG. 2.5. Semblance analysis (after Taner et al., 1969).

We use a velocity spectra display to determine the velocity function that provides optimum stacking. For QC purpose, we compare the original brute stacked section with the one containing picked gathers. If we note some primary reflections are missing, then either the spectra were interpreted incorrectly or there was some other mistake during the processing. The most important fact is that it is good to obtain the strong spectral response only in the very close vicinity of the reflection position (Stein et al., 2003, Sherwood, 1972).

After resorting the data from common shot to CMP gathers, I picked velocities on a coarse grid of 100 x 100 CMP's in the inline/crossline direction. My CMP gathers were contaminated by noise and it was sometimes very difficult to recognize the reflection arrivals. In order to improve the signal-to-noise ratio each supergather contains information from 20 adjacent CDP bins. The resolution quality of the velocity spectra was not satisfactory. Figure 2.6 shows the quality of one of the gathers I used in my coarse grid velocity analysis. I used these velocities to generate a brute stack to provide guidance for improvements in subsequent steps. Red arrows on Figure 2.6 show various flattened reflections including the target zone.

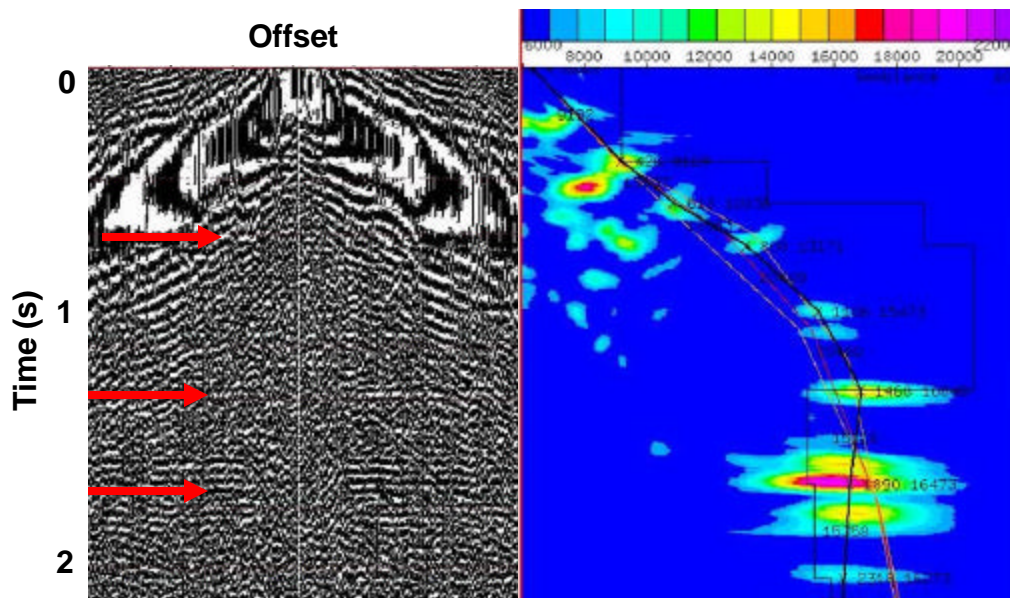


FIG. 2.6. CDP supergather (800 traces) after velocity analysis with NMO applied.

## 2.5. Deconvolution

Deconvolution is designed to compress the source waveform to approximate a spike and therefore improves the temporal resolution between closely spaced reflections (Yilmaz, 2001, Stein et al., 2003).

The Maljamar survey was acquired using vibroseis. The vibroseis trace,  $x(t)$ , can be defined as a combination of several different time sequence effects:

$$x(t) = r(t)*e(t)*s(t)+n(t) , \text{ where: } r(t)= \text{ the earth's reflectivity,} \quad (2-2)$$

$e(t)=$  the earth attenuation,  
 $s(t)=$  the input sweep,  
 $n(t)=$  random noise, and  
\* denotes convolution.

Crosscorrelation of  $x(t)$  with the time reversed sweep  $s(-t)$  deconvolves the sweep from the previous equation leaving the desired reflectivities:

$$r(t)*e(t) \sim [r(t)*e(t)*s(t)+n(t)]*s(-t). \quad (2-3)$$

The advantage of the crosscorrelation of the noise with the time inverse of the sweep,  $s(-t)$ , is the reduction of random noise outside the frequency range of the sweep. Crosscorrelation of the sweep with itself compresses the sweep to a zero-phase Klauder wavelet:

$$k(t)=s(t)*s(-t). \quad (2-4)$$

The earth attenuation,  $e(t)$ , has a minimum phase nature (Brittle, 2001).

Because of the mixed phase embedded wavelet, I have decided to test two deconvolutions. Wavelet shaping (WSHAPE in Focus) does not require knowledge about the phase of the source wavelet. Spectral balancing (SPEQ in Focus) can be used to provide a zero phase deconvolution.

I applied wavelet shaping in a surface consistent manner, which is designed to preserve relative amplitude of the data. The WSHAPE algorithm applies a cepstral domain wavelet shaping filter to all traces of a common shot or common receiver ensemble. Because of the large contrast that existed among the amplitudes of adjacent traces in the field (Figure 2.7a) I used wavelet shaping in combination with a scaling program that

equalizes seismic trace amplitudes within the specified time gates (Appendix B) (Figure 2.7b). Prior to application of scaling I applied a gain of 500 ms. As we can see from Figure 2.7, strong and weak amplitude variations in Figure 2.7a appears less severe on Figure 2.7b.

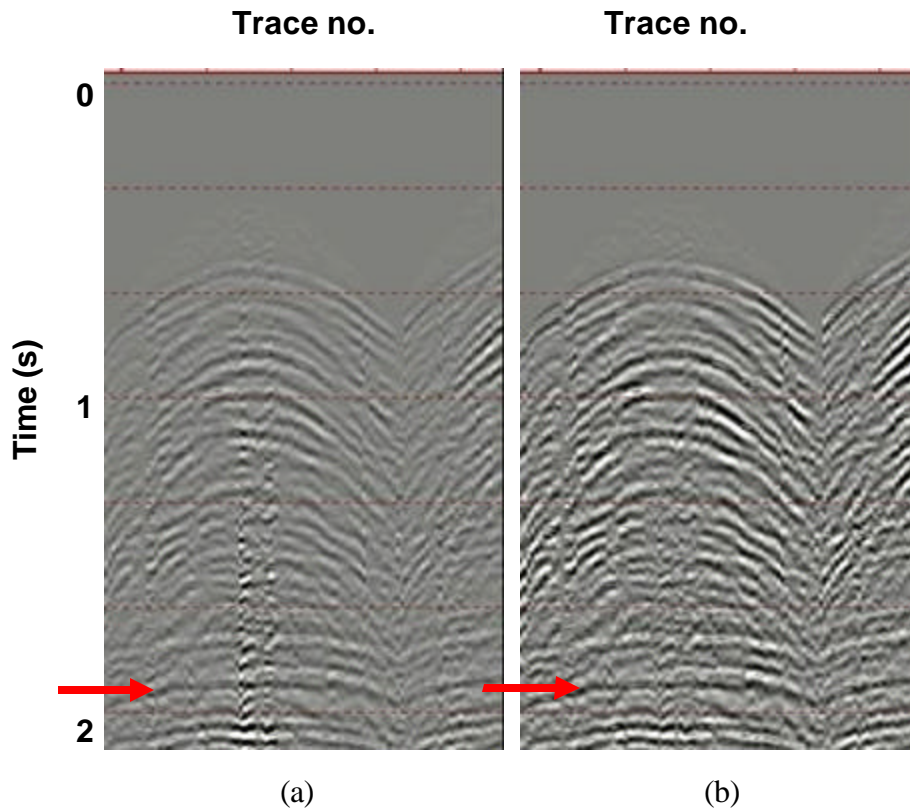


**FIG. 2.7.** Shot gather a) before and b) after balancing using a running window of 1s.

Figure 2.9b demonstrates that wavelet shaping removed the strong influence of the near offset noise cone. As a QC measure, I generated the stacked sections shown in Figures 2.9c and d. The reflections indicated by arrows are “sharper” after shaping. I evaluated the SPEQ flow in a similar manner. SPEQ broadens the spectrum of the data and provides the time-variant, zero-phase spectral balancing using a sliding AGC gate (Focus Help, 2005). This method provided much better results on the entire survey than WSHAPE, including

the amplitude balancing (Figure 2.10). The reflector energy is stronger and the noise is better suppressed than the images shown in Figures 2.9a and c. I compare these two flows on Figure 2.11. Figure 2.8 just gives the position of the stacks for the above testing and Appendix B has all the parameters that I used for both of the deconvolution processes.

All subsequent images will be built on data processed by spectral balancing.

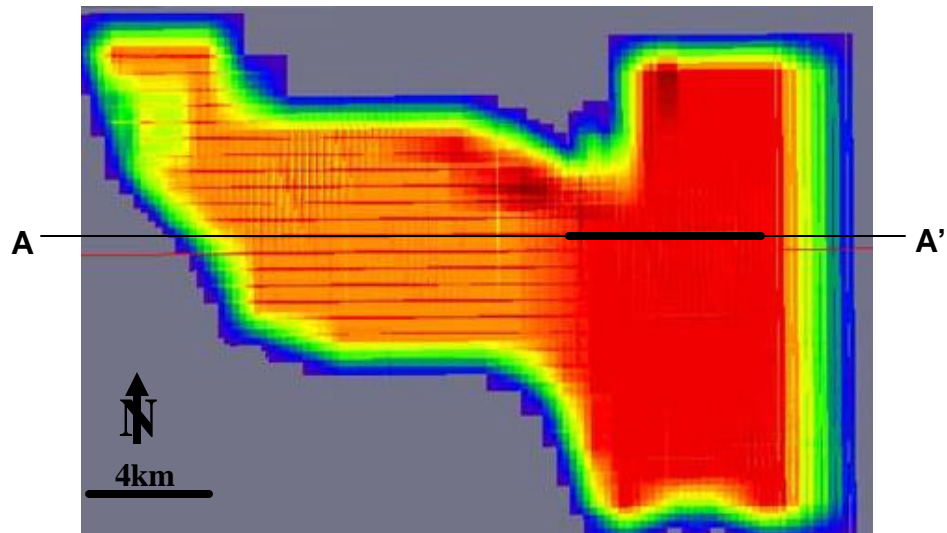


**FIG. 2.8.** Stack position from the Figures 2.9, 2.10, 2.11.

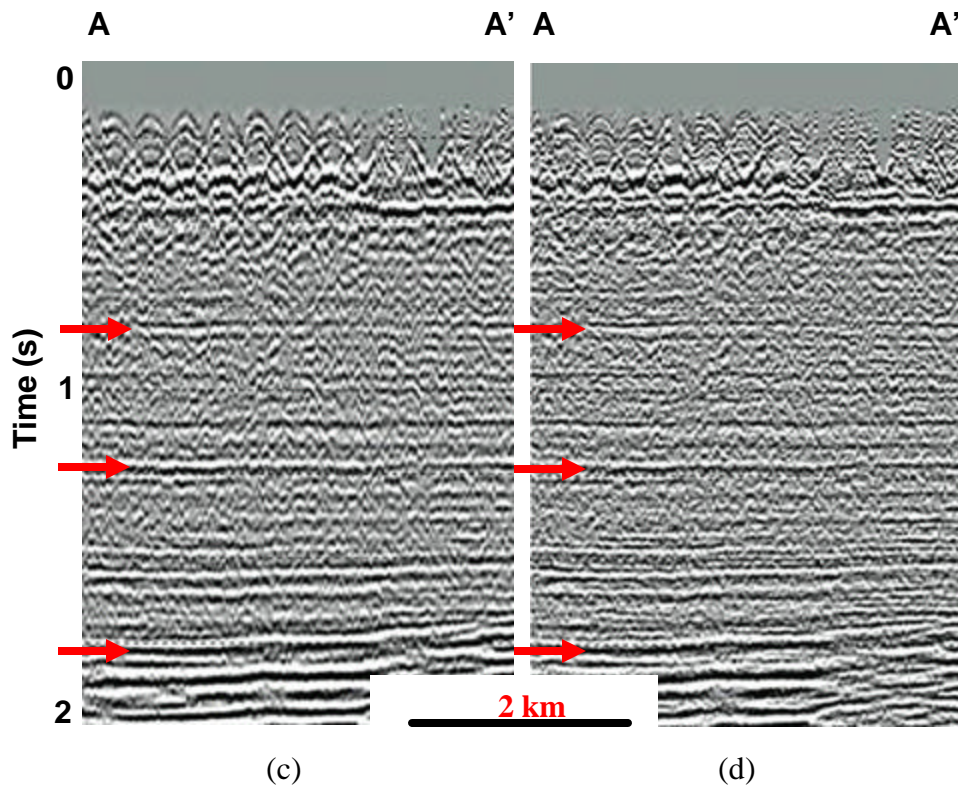
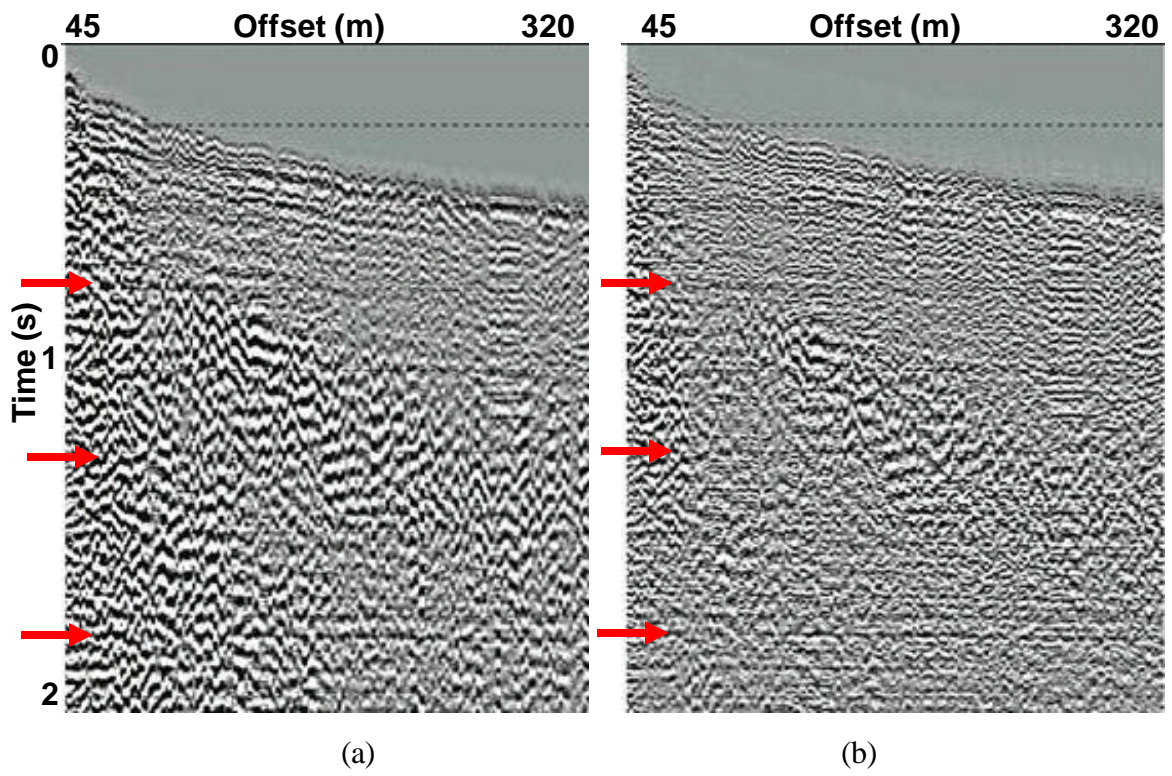
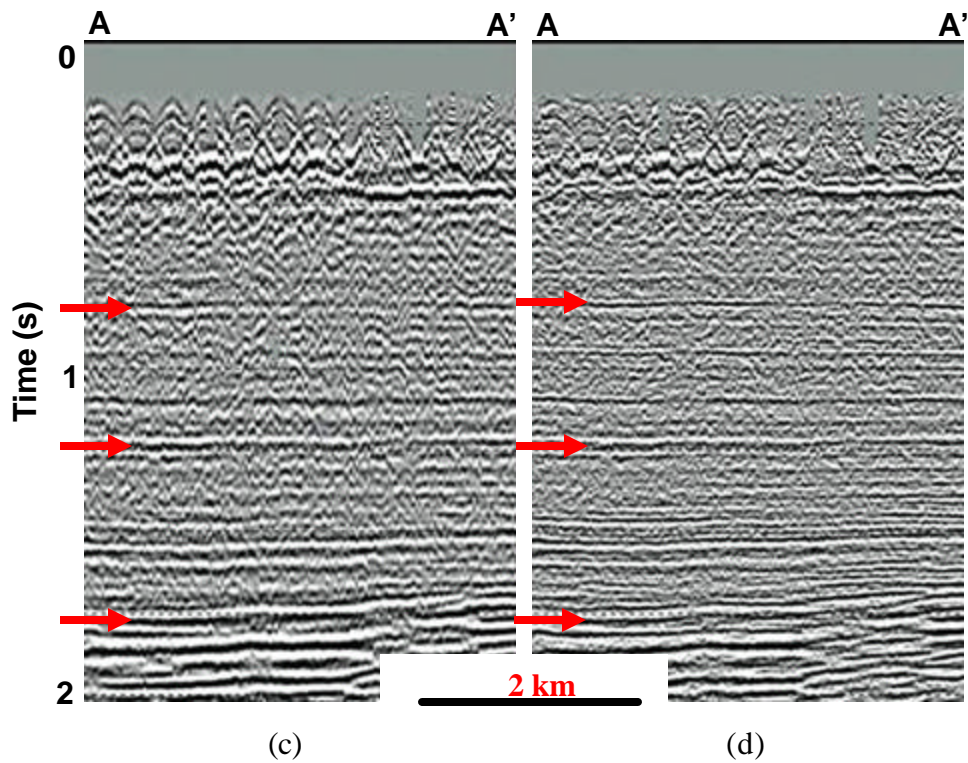
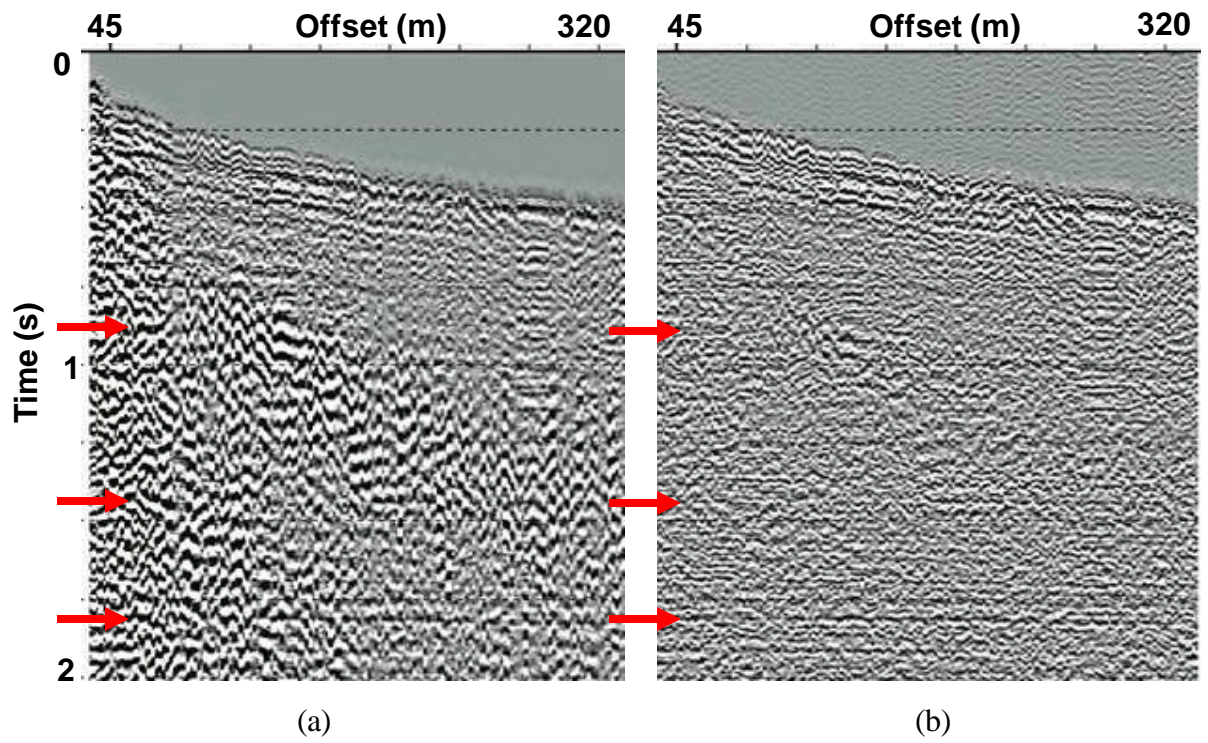
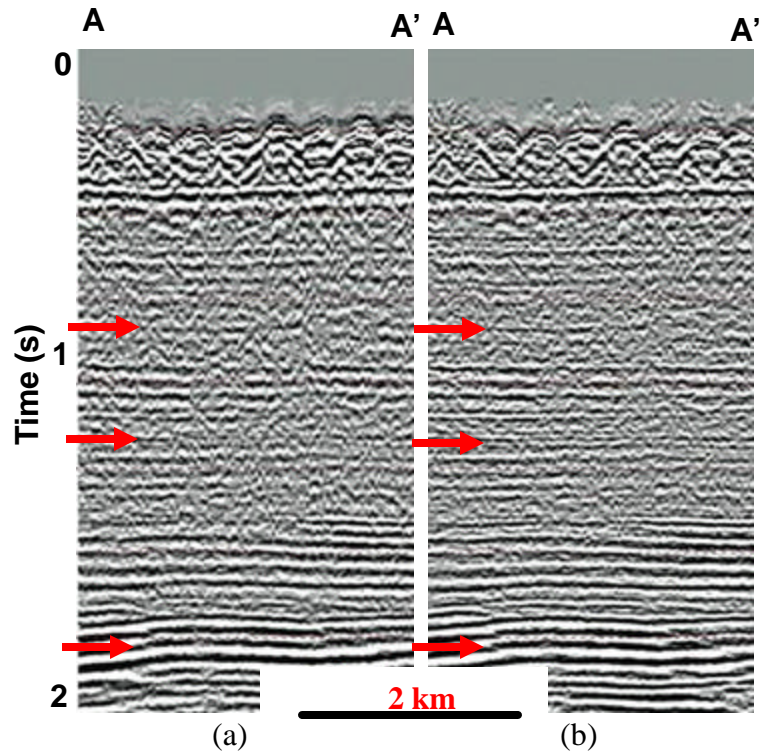


FIG. 2.9. Shot gather (a) with (b) without WSHAPE and brute stack (c) before (d) after WSHAPE application. The red arrows on (b) and (d) show increased resolution of events.



**FIG. 2.10.** Comparison of the shot gather: (a) before and (b) after SPEQ. Brute stack (c) before and (d) after SPEQ application. The red arrows on (b) and (d) highlight “sharper” continuous reflections.



**FIG. 2.11.** Comparison of the brute stack with (a) WSHAPE versus (b) SPEQ. (b) is less “wormy” and better focused compared to (a). Reflections indicated by arrows are more continuous.

## 2.6. Residual Statics

Residual static corrections represent uniform shifts in time applied to traces in order to compensate for time delays in the near-surface. Like wavelet shaping, these delays are applied to sources and receivers in a surface consistent manner. In order to correct for surface effects the reflection events on the different traces of the raw data are time shifted. The time shift is calculated using crosscorrelation computations in order to derive the best alignment for the traces of each CMP. Since the data are already adjusted for the “field statics” of measured elevation and weathering zone effects, residual statics measure relatively small misalignments. These time-shifts will degrade the wavelet character and

bandwidth during stack. Mathematically, we can write the time anomaly for the  $i^{\text{th}}$  trace as:

$$\Delta t_i = S(s_i) + G(g_i) + Y(y_i) + R(y_i)h_i^2, \quad (2-5)$$

where:  $S(s_i)$  = shot station static correction,

$G(g_i)$  = geophone station static correction,

$Y(y_i)$  = midpoint station structure term,

$R(y_i)$  = midpoint station residual NMO correction, and

$h_i$  = shot-receiver offset.

The power of the stacked section is highest when all the traces are aligned with no relative static time shifts (Ronen et al., 1985).

In order to obtain the pilot traces with highly improved S/N ratio for later crosscorrelation, I first generated a brute stack of the spectral balanced data, followed by an F-xy spatial prediction filter. This filter is used to reduce random noise and can be very effective in removing noise from the data before stacking it. F-xy decon can be applied before statics or even before deconvolution (Grimm et al., 2003). The F-xy decon filter assumes locally planar events such that the Fourier amplitudes of the traces are predictable in all spatial directions as a combination of adjacent trace amplitudes. The prediction filter has a rectangular shape with predicted trace at the center. The filter coefficients are estimated from correlation estimates made within a moving rectangular window of traces (Chase, 1992).

I applied the fxy filter after spectral balancing on the stacked data and used this volume with enhanced S/N ratio as pilot trace for each CMP gather. The correlations are made for time windows selected on the basis of estimated S/N quality (Wiggins, 1976). As seen in Figure 2.12, reflection arrivals on the pilot volume look much more coherent than those of the brute stack with spectral balancing. However, there is also an obvious reduction in frequency content when F-xy is applied.

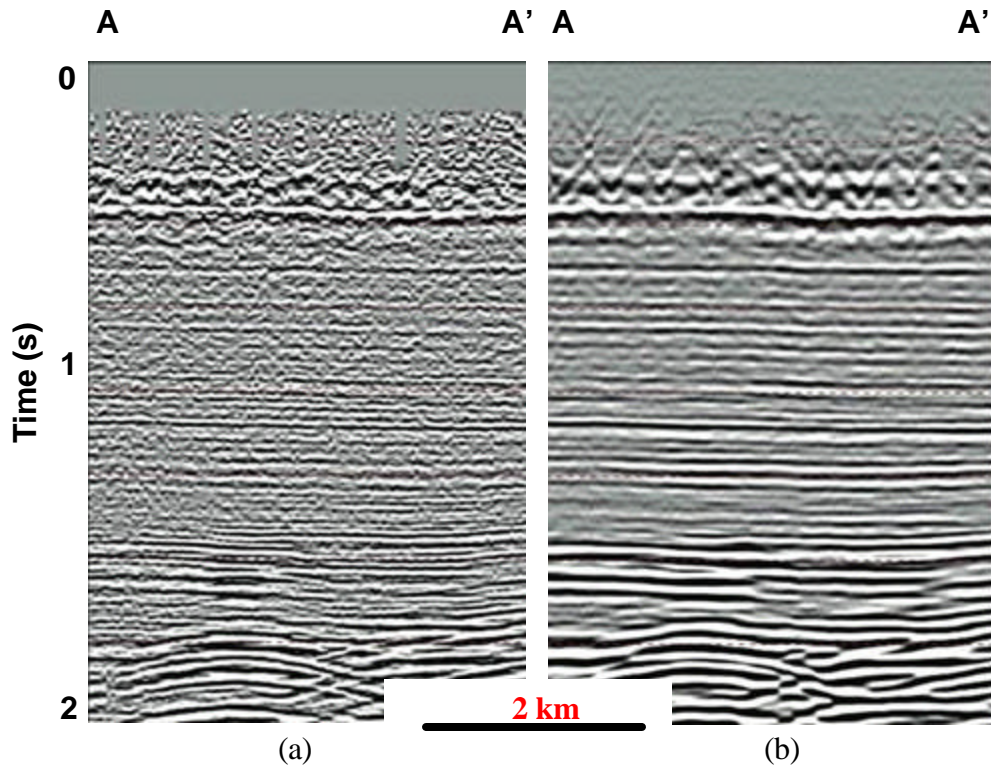


**FIG. 2.12.** Brute stack with spectral balancing (a) before and (b) after F-xy filter.

While this method of applying residual statics is sensitive to the errors in NMO velocities, it is easy to use iteratively with velocity analysis (Ronen et al., 1985). After the first pass of velocity picking and applying deconvolution, I created the pilot for the residual statics calculations, ran STAT3D, which stores the static calculations in the trace headers, and applied the calculated static shifts to the data. The second pass of velocity analysis on the data with the improved S/N ratio was then applied. The result looked much improved with sharper reflections and better alignment of the arrivals (Figure 2.13).

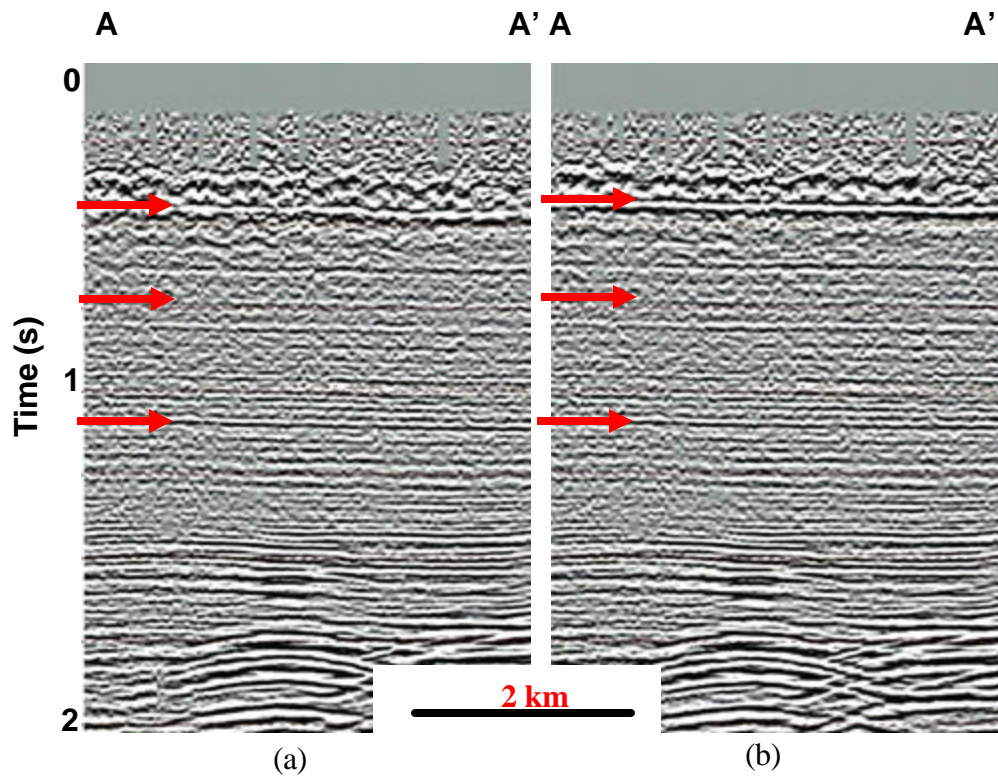
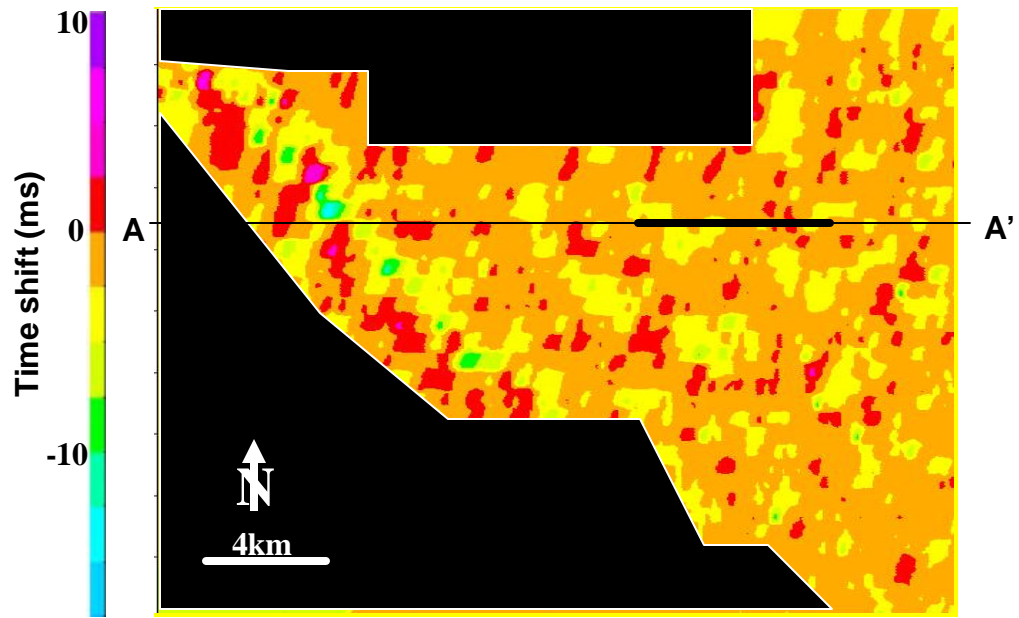
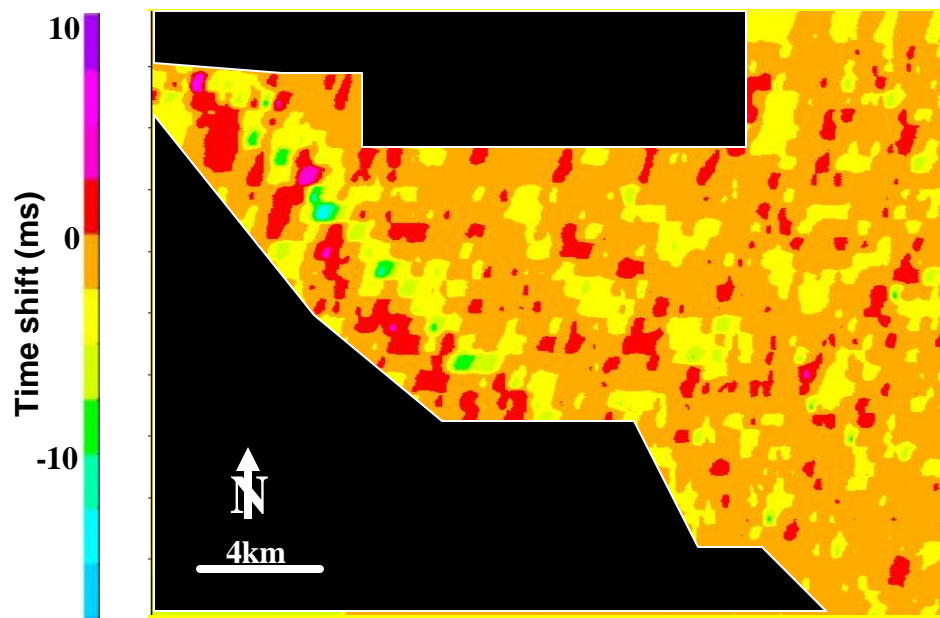


**FIG. 2.13.** Comparison of the brute stack after SPEQ (a) before and (b) after residual statics. Arrows highlight better continuity reflections.

The values of the residual statics converge within a few iterations (Figures 2.14, 2.15). Two iterations were sufficient.

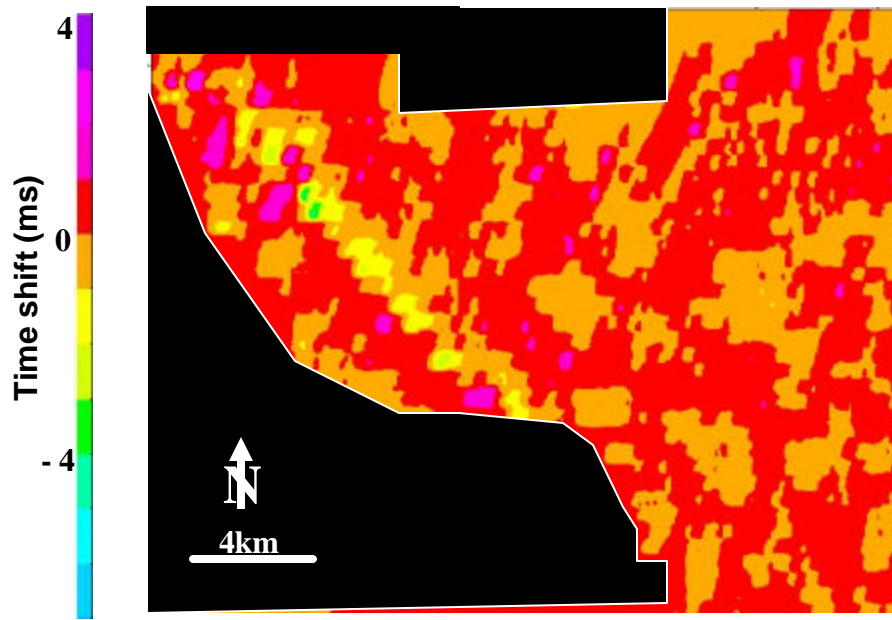


(a)

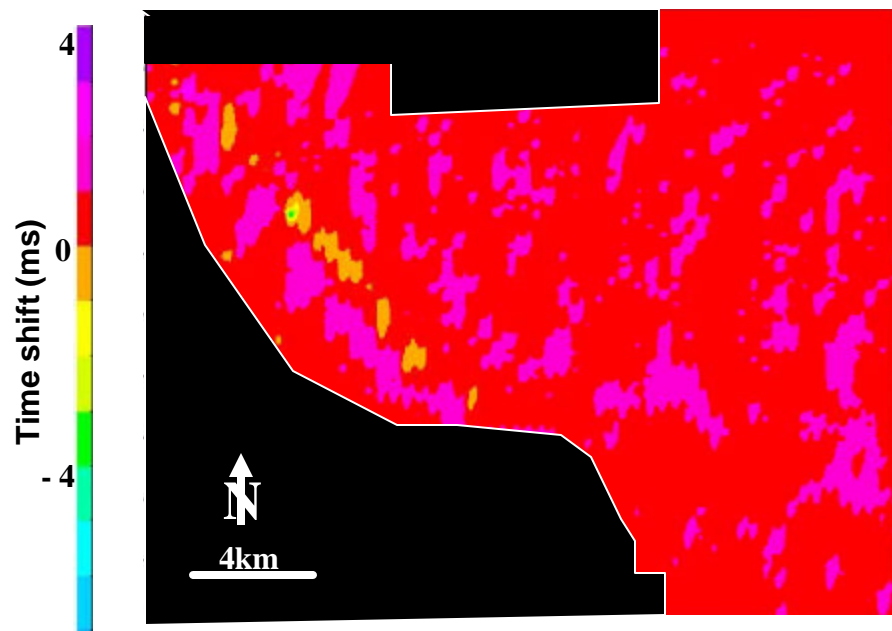


(b)

**FIG. 2.14.** Residual static correction in the first iteration for: a) shot and b) receiver. The residual static corrections for shots and receivers are in the range of -10 to 10 ms. Since the values are very high I applied the statics and did velocity analysis afterwards. The AA' line is the position of the inline from Figure 2.13 and Figure 2.12.



(a)



(b)

**FIG. 2.15.** Residual static correction in the second iteration for: a) shot and b) receiver. The residual static corrections for shots and receivers are in average range from -2 to 2 ms. Since the values are very low I did not attempt a second set of velocity analysis.

## 2.7. Velocity Analysis

Stretching is a frequency distortion in which events are shifted to lower frequencies. Due to stretching, stacking of CDP gathers with large offsets contaminates the shallow events. This problem can be solved by muting those stretched zones and applying the filters in order to improve data quality (Neidell, 1980). Since the Maljamar-Vacuum data had a very poor signal-to-noise ratio in shallow areas, I wanted to use a less harsh mute in order to have more defined shallow events. The stretched zone appears as a low-frequency zone in the shallow section. I also reduced the size of my supergathers from 20 to 11 gathers to improve lateral resolution (Figure 2.16).

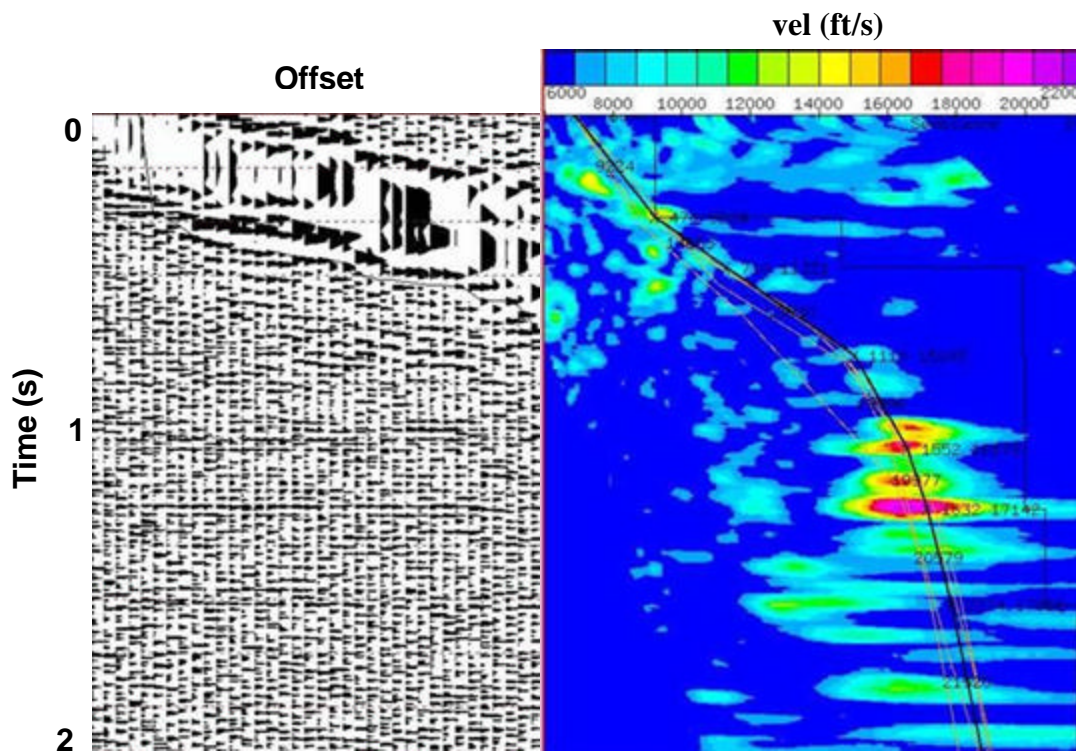
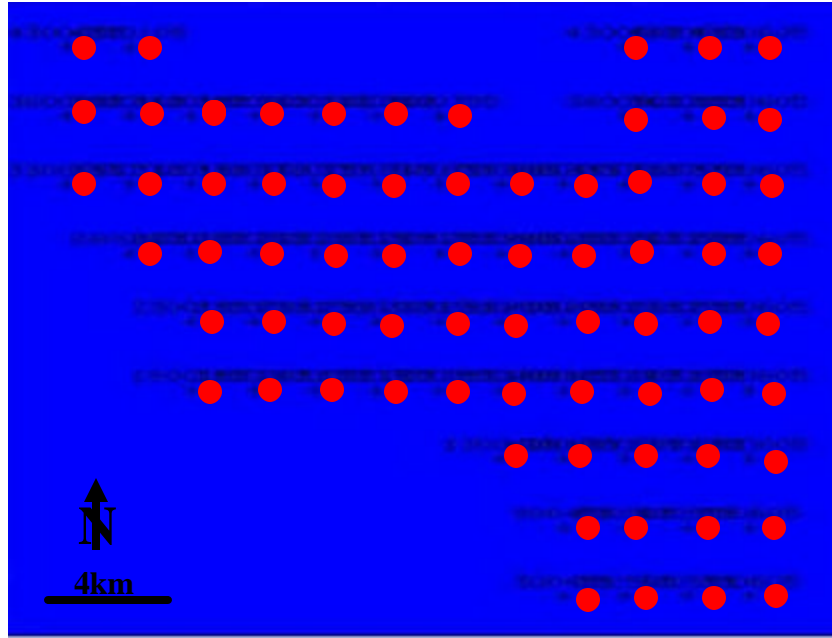


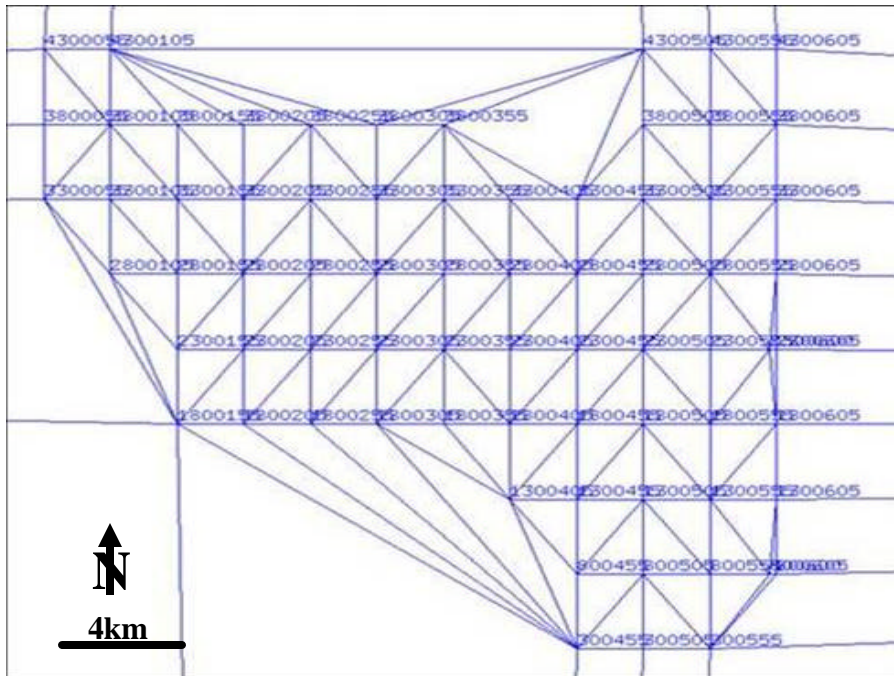
**FIG. 2.16.** The supergather with the calculated coherency on the right and applied NMO correction. Velocity values start at 2.2 km/s and reach up to 7 km/s.

After the first iteration of residual statics and new velocity analysis on a finer 50 x 50 CMP's grid (Figure 2.17) I was not satisfied with the mute in the shallow areas, so I

spent some time creating my own mute for particular gathers. Then, after stacking the data with the new velocities to obtain a satisfactory shallow image, I decided to apply a second iteration of residual statics with the results of a previous run as a starting point. Once again I generated a pilot trace using the improved velocities for NMO correction, and reran the module STAT3D. Since the residual shifts were very small, I did not go into velocity analysis again and concluded that I could proceed to the isotropic migration. In Figure 2.18 I show the improved quality of the stack with the new stacking velocities that I picked.



(a)



(b)

**FIG. 2.17.** Positions of the velocity picks (a) red dots at the surface and (b) triangulation.

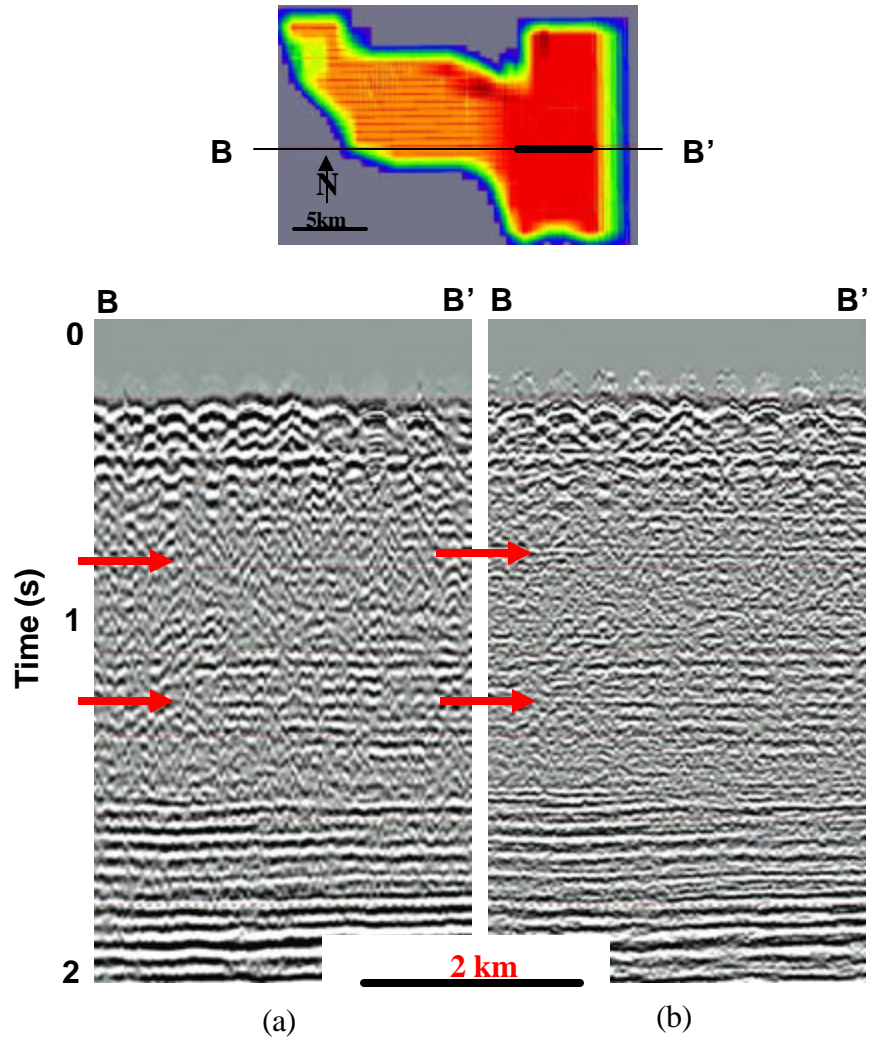


**FIG. 2.18.** Stacked section a) before and b) after a second iteration of velocity analysis. Red arrow indicates improved reflections around the target zone. Above is the fold map with the line location.

### 3. ANISOTROPIC PROCESSING

#### 3.1. Introduction

Anisotropy describes the change in velocity with direction (Yilmaz, 2001). The most common anisotropy model of sedimentary formations is transverse isotropy (TI) with arbitrary orientation of the symmetry axis (Grechka, 2002). Horizontally layered sediments are considered to be vertical transverse isotropy (VTI) media if they have a vertical symmetry axis (Figure 3.1).

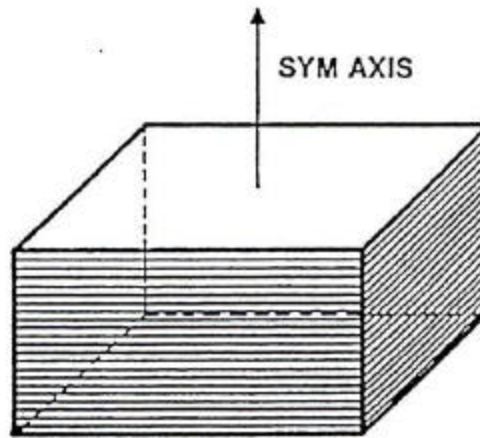


**FIG. 3.1.** VTI media with vertical symmetry axis (after Mavko, 1999).

The main physical reason for TI symmetry is the intrinsic anisotropy of sedimentary formations (primarily shales) and periodic fine layering (Grechka, 2001) (Figure 3.2).

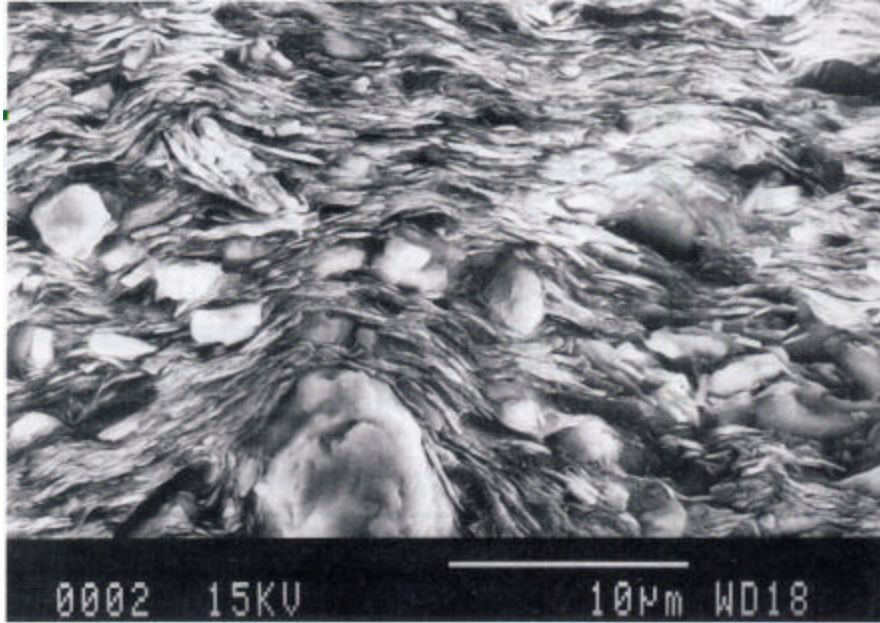


**FIG. 3.2.** Microscopic vertical section through shale (after Thomsen, 2002).

Velocity estimation is the most difficult step in imaging seismic data for anisotropic media (Grechka, 2002). Conventional migration usually assumes an isotropic earth. Ignoring anisotropy in prestack depth migration may cause defocusing and mispositioning of events as shown in Figure 3.3. Steeply dipping reflectors are more sensitive to migration anisotropy velocity errors (Larner and Cohen, 1993). In this chapter I will estimate the importance of including anisotropy in the analysis of the Maljamar survey.

By definition the velocity for TI media is constant in any direction perpendicular to the axis of symmetry (Yilmaz, 2001).

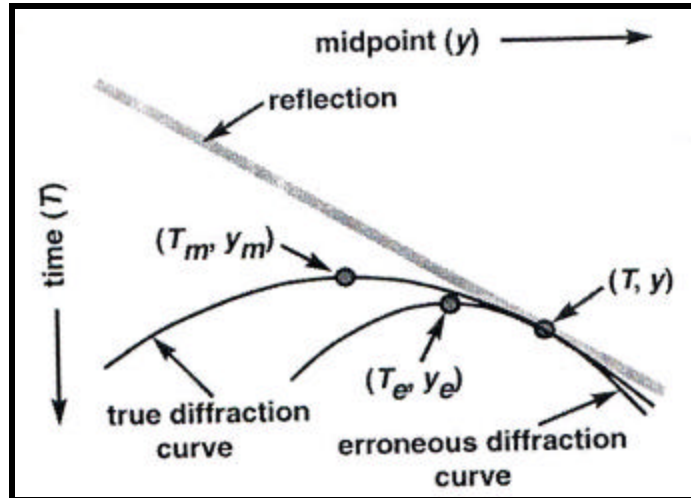


**FIG. 3.3.** Schematic time section showing the relationship between the unmigrated position  $(T, y)$  on a sloping reflection, the position  $(T_m, y_m)$  to which it should migrate and the position  $(T_e, y_e)$  at which it is actually imaged when the data are migrated with an erroneous velocity function (after Larner and Cohen, 1993).

There is considerable previous work pertaining to problems associated with imaging structures in anisotropic media. Thomsen (1986) points out the fundamental inconsistency of trying to image a potentially anisotropic subsurface using the assumption of isotropy. Larner and Cohen (1993) and Alkhalifah and Larner (1994) document migration errors in TI media. Isaac and Lawton (1997) demonstrate the influence of imaging TI media with standard isotropic processing and show as a result large errors in the lateral position of a simulated reef edge. Isaac and Lawton (1999) show dramatic positioning errors of horizontal reflectors below TI media with a rotated symmetry axis. Vestrum et al. (1999) compare the apparent position of structures below dipping overburden after applying isotropic and anisotropic migrations (Figure 3.4).

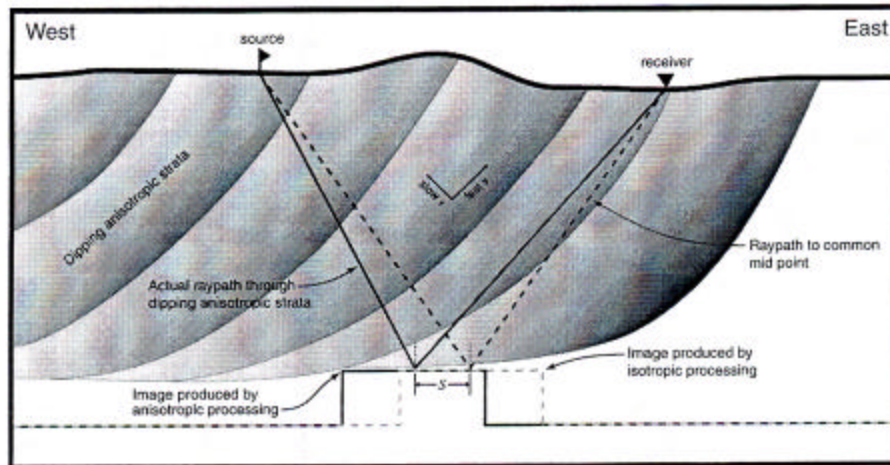


**FIG. 3.4.** Comparison between isotropic and anisotropic processing and the expensive result of misimaging (after Vestrum et al., 1999).

### 3.2. Velocity Analysis

The expected reservoir in the Vacuum-Malजार survey is at 0.75 s. Since shale is present in this zone, and since I have offsets up to 3350 m, I need to determine if I need to account for anisotropy in my processing.

Unfortunately, the target zone is strongly influenced by shallow noise effects—ground roll contaminates the inside traces while head waves contaminate the outside traces. In order to analyze anisotropy in this shallow area, I further investigated filtering the data.

If anisotropy is expected, one begins by estimating the velocity of the near traces, where the effect of anisotropy is minimal (Appendix A). To do so, I took the CMP gathers from the previous step described in Chapter 2, and applied a deeper mute to be sure that I am in the range of near to mid-offsets, where  $x < z$ . I then estimated  $V_{nmo}$  as I did earlier in the processing flow.

I then estimated the  $\eta$  (Appendix A) parameter which is used in the far offset imaging. However, prior to picking the  $\eta$  function, I had to obtain an improved S/N ratio.

I began by generating supergathers consisting of 20 x 20 inline and crossline CMP gathers, and picked velocities every 100 CMP's (Figure 3.5). The quality of the signal increased, but not enough, particularly in the shallow parts.

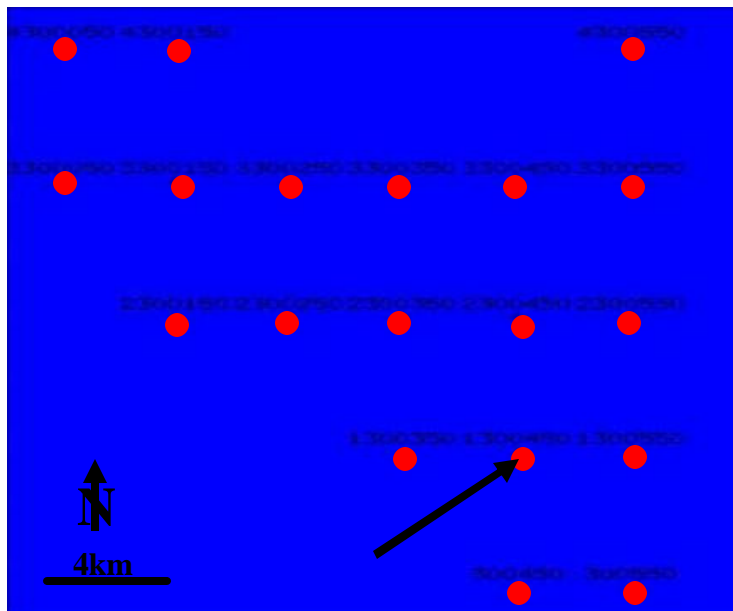


**FIG. 3.5.** Position on the 0 time slice of the supergathers for ? picks. The black arrow shows the gathers that will be displayed on Figure 3.6.

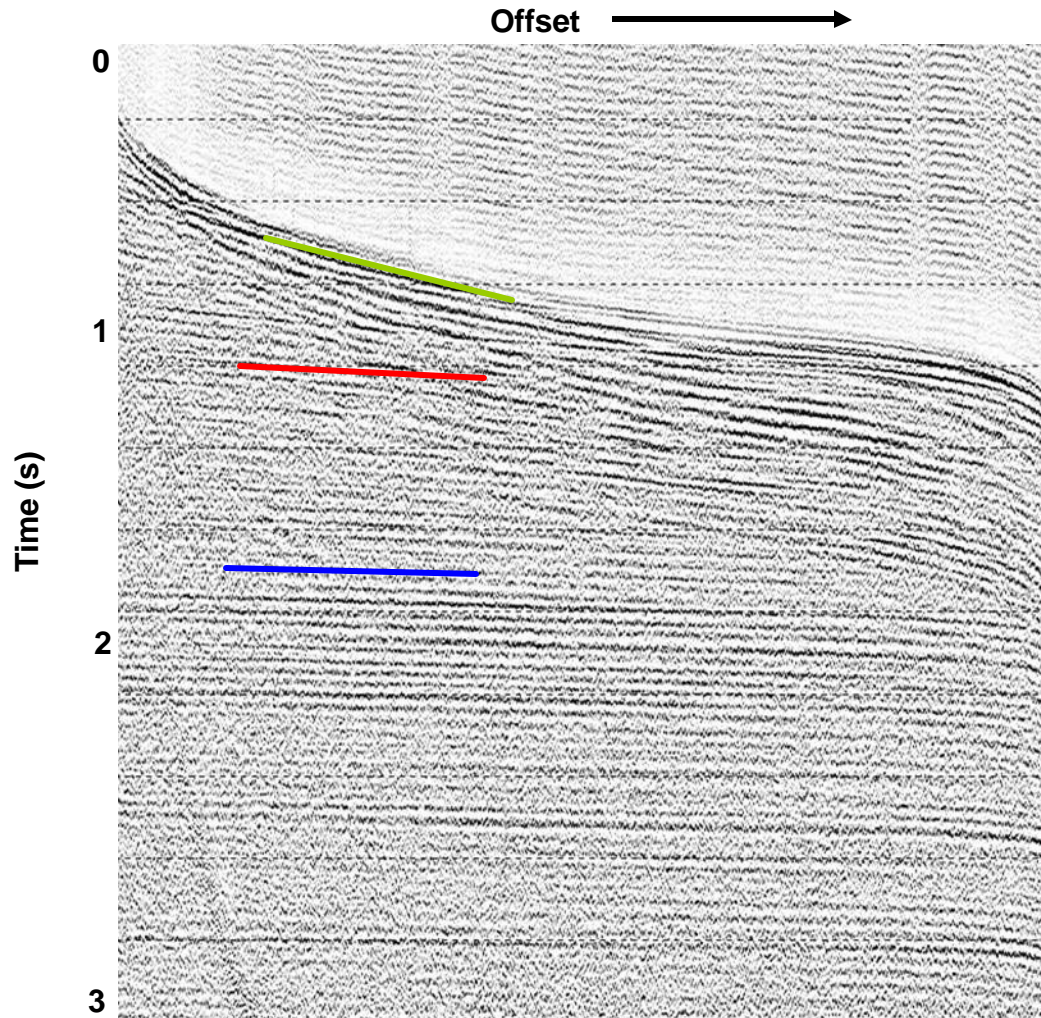


**FIG. 3.6.** A supergather containing approximately 2000 traces. Irregular moveout is due to irregular trace separation. The green line indicates head waves, while the red line indicates reflections of interest. The blue line indicates a deep reflection that is easy to recognize.

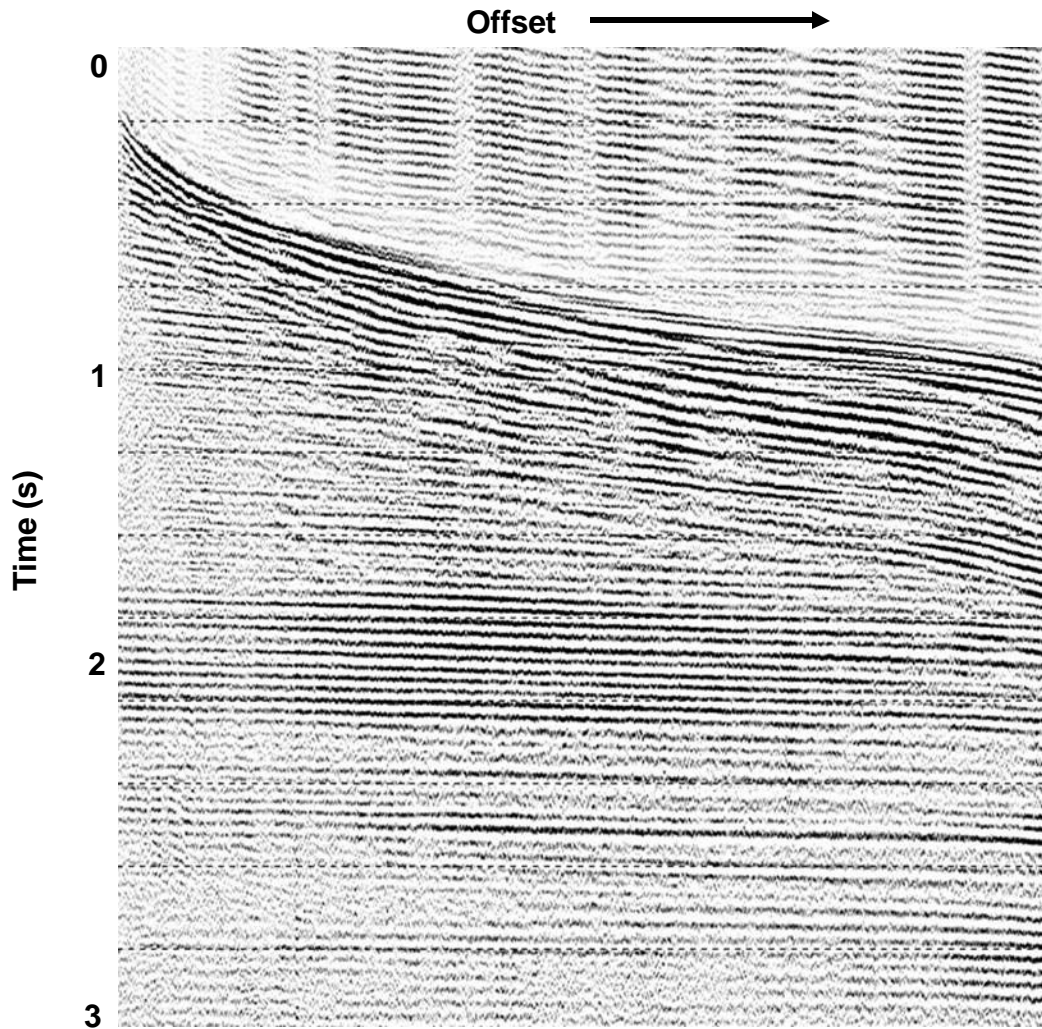


**FIG. 3.7.** Supergathers shown in Figure 3.6 after reflection enhancement using  $f_{xy}$  spatial prediction filter. Refractions are still strong.

First, I attempted to enhance the signal using  $f_{xy}$  spatial prediction filter (FX-decon). This filter is designed to use the traces from both sides of the central trace in the range of data to create the spatial filter that enhances the predictable energy. The filter transforms the data into the  $f$ - $xy$  frequency domain. Each frequency is independently analyzed for signal using a deconvolution-type algorithm. Figure 3.7 depicts the outcome,

and while there is improvement, both the reflection signal and refraction noise are preserved.

Since I was satisfied with a signal to noise ratio of below 1 s, I divided each gather into two parts: shallow and deeper. I tested several filters on the shallow part, but was unsuccessful in flattening the refractions. I, therefore, resorted to a simple Butterworth filter. Since head waves are a low frequency phenomenon, a band-pass Butterworth filter (40-120 Hz) eliminates them and, unfortunately, the corresponding low-frequency component of the signal (Appendix B). I then merged lower and upper portion to start picking  $\tau$  (Figure 3.8).

I picked  $\tau$  from these filtered supergathers and found values of  $\tau=0.15-0.3$  at 0.6-0.8 sec., close to the zone of interest (Figure 3.9). Once the  $\tau$  field was picked (Figure 3.10), I had the two parameters necessary for anisotropic migration.

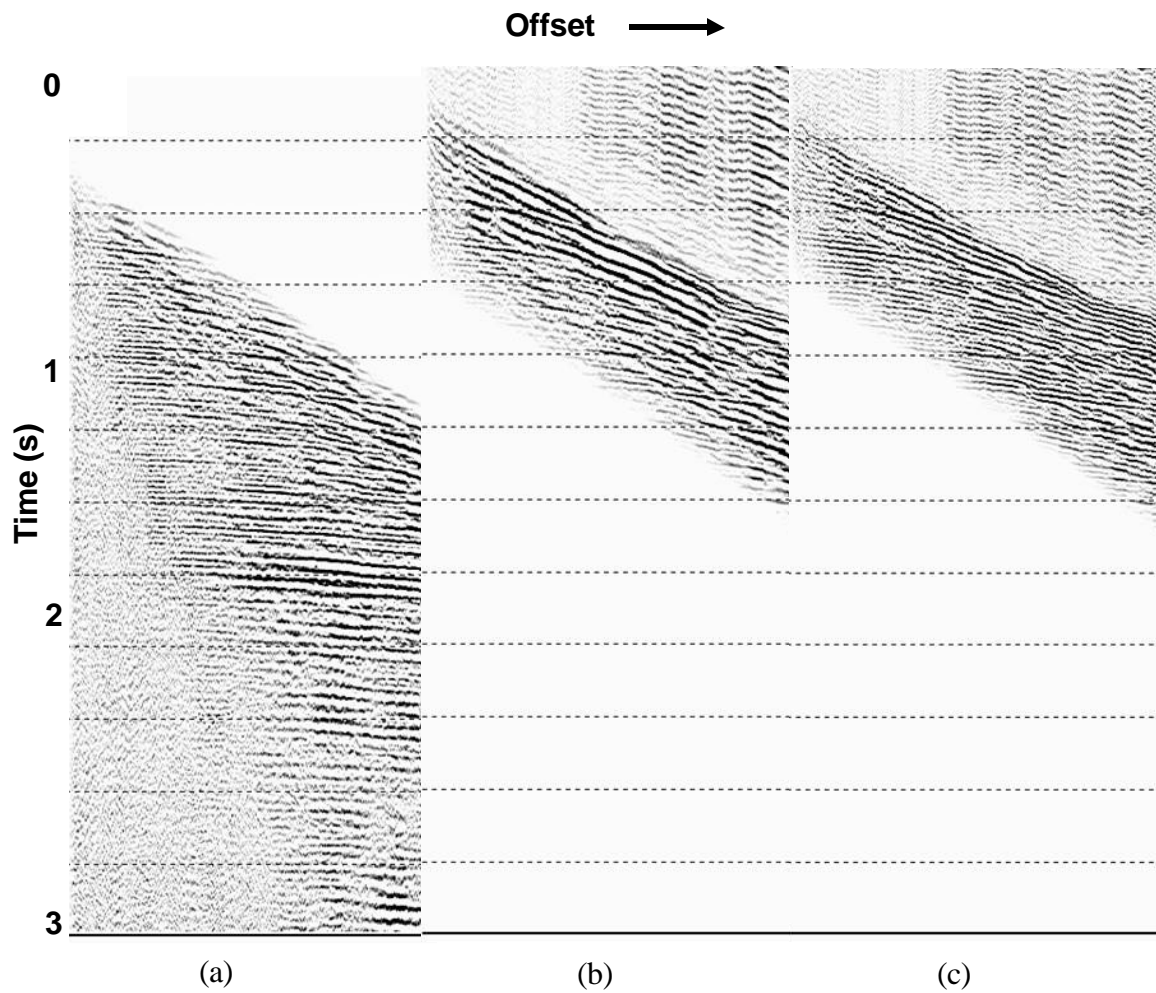


**FIG. 3.8.** Separation of a supergather into (a) a deeper section relatively uncontaminated by head waves and (b) a shallower section contaminated by head waves. (c) band-pass Butterworth (40-120 Hz) filtered version of (b) allowing shallower reflections to be seen.

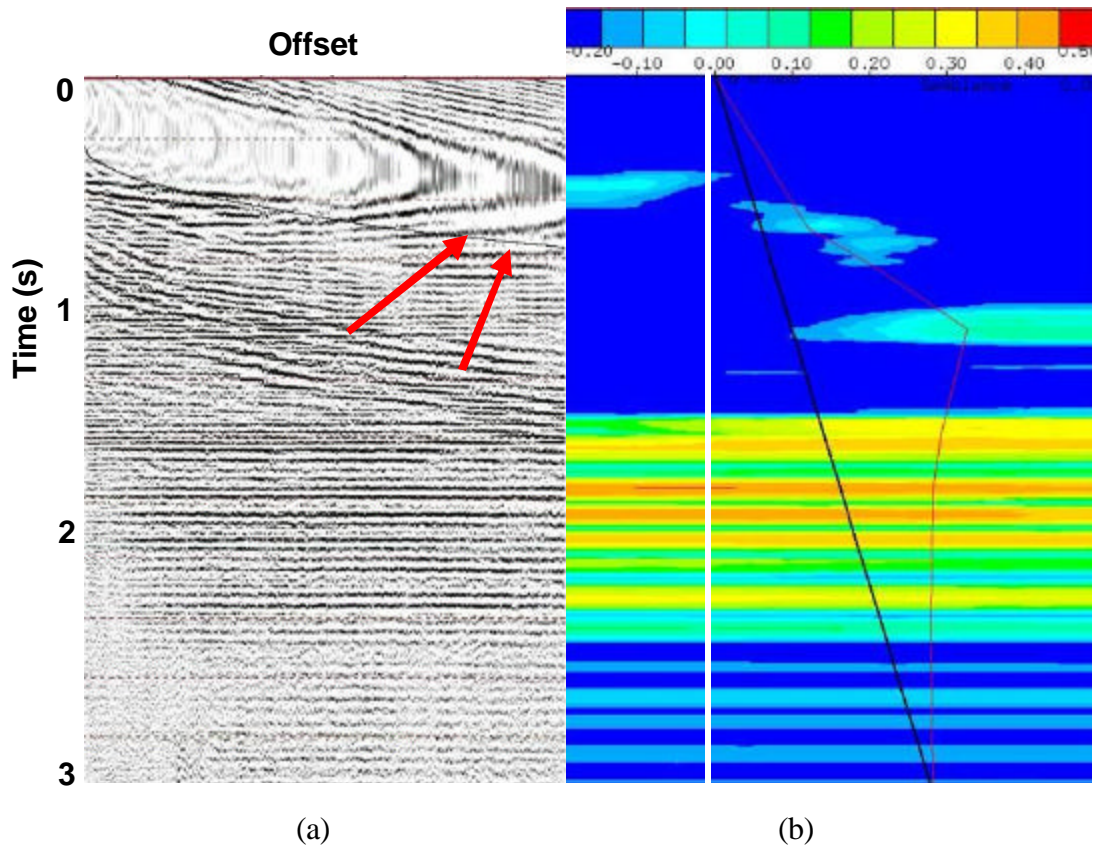


**FIG. 3.9.** (a) Supergather of 2000 traces before  $\tau$  was picked. The red arrows point out the “hockey stick” effect on the far offsets. (b) Presents  $\tau$  semblance. The black straight line illustrates that  $\tau$  field was not picked, while the white vertical line shows  $\tau = 0$ . Horizontal color bar represents the range of  $\tau$  values present ( $-0.2 < \tau < 0.5$ ).

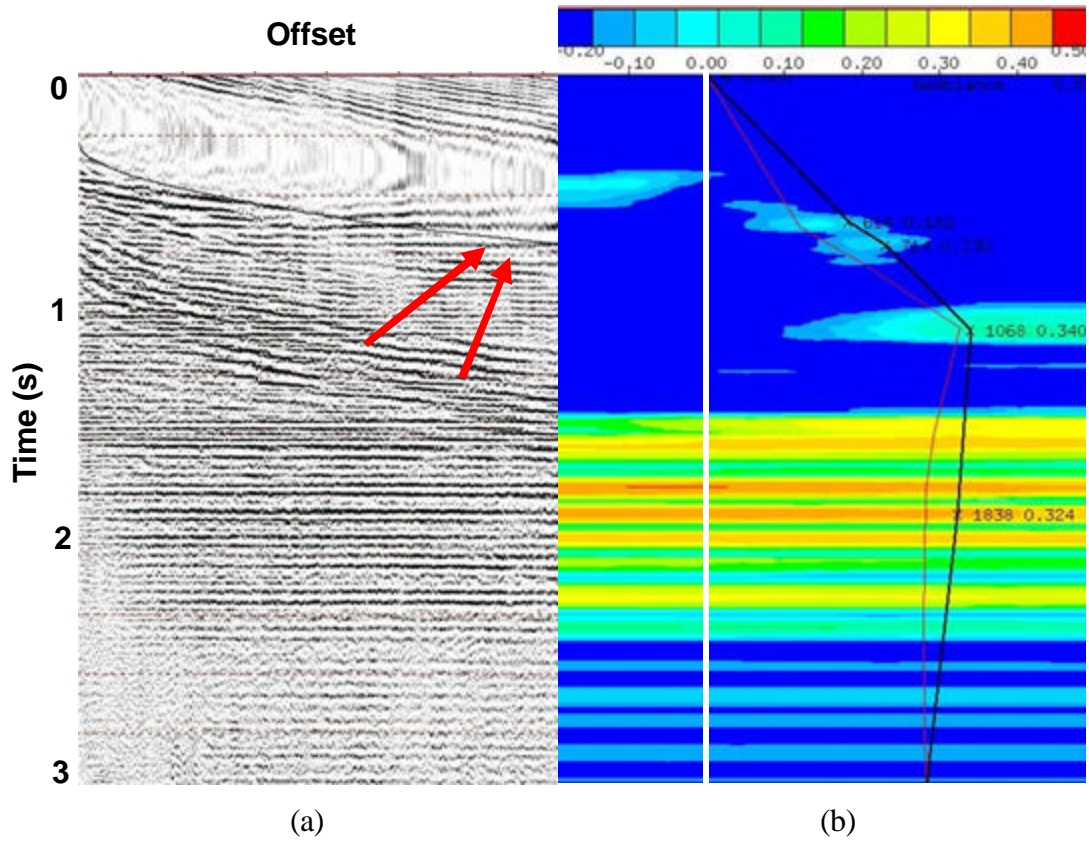


**FIG. 3.10.** (a) Supergather of 2000 traces after flattening using  $\tau$ . The red arrows point to flattened events on the far offsets due to including  $\tau$ . (b) Shows  $\tau$  semblance. The black curved line depicts  $\tau$  values picked on this gather which are  $0.28 < \tau < 0.35$ , while the white vertical line shows  $\tau = 0$ . The horizontal color bar represents range of  $\tau$  values present ( $-0.2 < \tau < 0.5$ ).

## 4. MIGRATION

### 4.1. Introduction

Migration is the process that moves stacked seismic data into its correct position in both space and time. Even after NMO, events from dipping reflectors are plotted in the wrong place on the stacked section. These reflectors need to be moved “up-dip” along the hyperbola in order to put them in the correct place. The shape of this hyperbola depends on the velocity field. Prestack migration is a process that moves each sample to all possible reflector positions and creates the image using the principle of constructive and destructive interference.

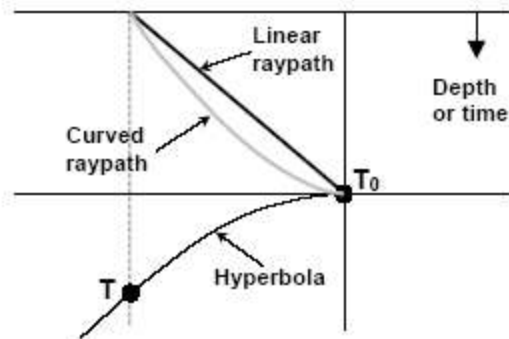


**FIG. 4.1.** Simplification of curved raypath to linear raypath using RMS velocities (after Bancroft et al., 1997).

Kirchhoff migration was applied to the Maljamar-Vacuum survey, summing energy along “diffractions” and placing that energy at the apex of the diffraction. Kirchhoff time migration approximates curvilinear with linear ray paths (Bancroft et al., 1997) (Figure 4.1) using the equation:

$$t_x^2 = t_0^2 + x^2/V_{\text{nmo}}^2, \text{ where: } t_x = \text{two-way arrival time,} \quad (4-1)$$

$t_0$  = two-way normal incidence time,

$X$  = offset distance, and

$V_{\text{nmo}}$  = stacking velocity.

Since I anticipated lateral velocity variations and structural complexities like minor faults, I predicted prestack time migration to do a better focusing job. I migrated the data using both isotropic and anisotropic algorithms.

#### 4.2. Isotropic Pre-Stack Time Migration

Kirchhoff migration in general provides good results for steep dips, handles velocity variations in time, and is computationally efficient. In the presence of severe lateral velocity variations, where velocity changes abruptly within a gather, the stacking process may degrade rather than enhance the data.

I will try to improve the signal using prestack time migration.

Before applying pre-stack time migration (PSTM) I had to create a 3D velocity field by interpolating the discretely picked vertical functions picked from velocity spectra. RMS velocities from Figure 4.2 were used to create a velocity model for PSTM.

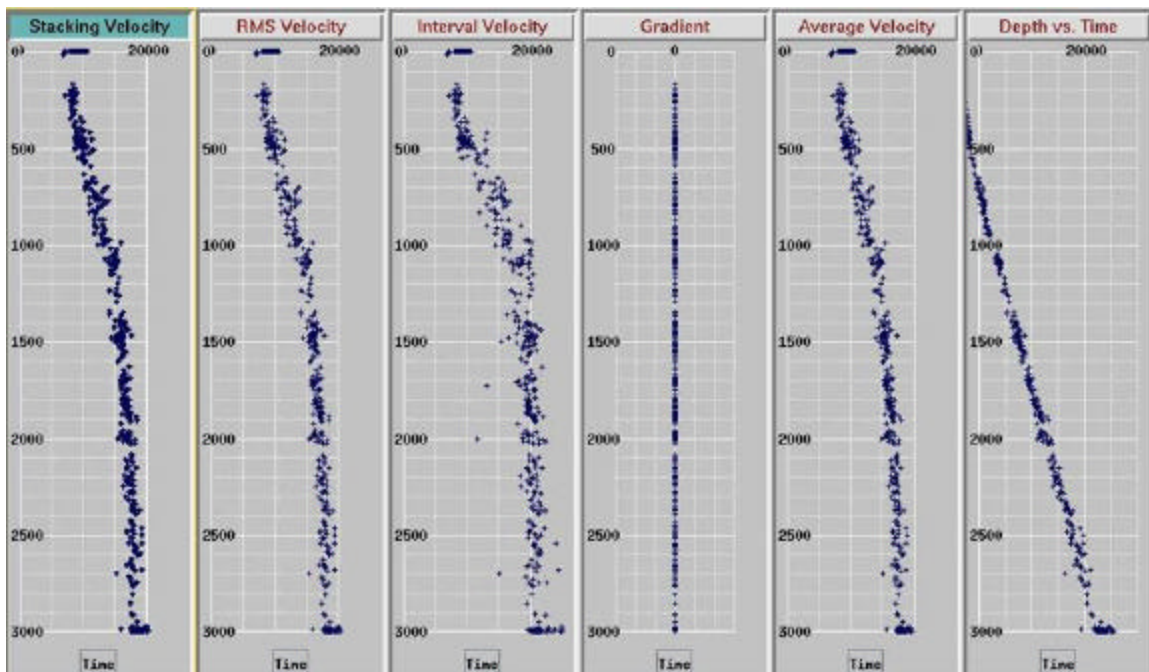
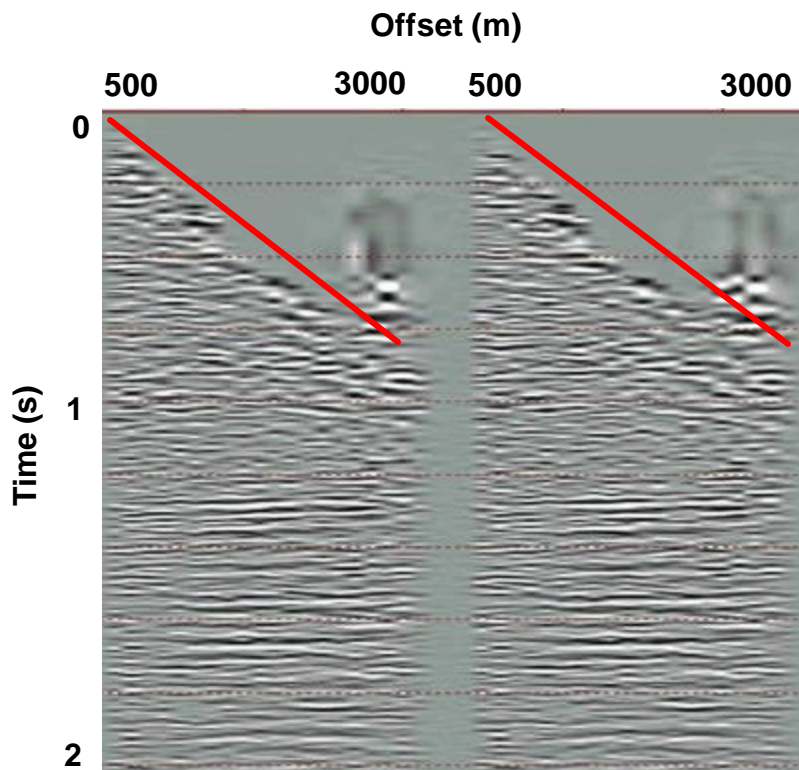


FIG. 4.2. A representative velocity functions derived from Focus in order to create the RMS velocity volume used for PSTM.

Ideally, each offset should be equally sampled on the earth's surface prior to migration. Since my data were not evenly sampled in space I had to apply weights to my model. When the shape of the survey is irregular as in Maljamar, it is difficult to accurately interpolate missing data. In this case it is necessary to apply summation weights. Each sample that contributes to the migration sum is separately weighted according to neighboring traces and the output migrated trace (Zheng et al., 2002). This procedure balances the output amplitudes, partially correcting for irregularities in the acquisition geometry (Canning et al., 1998). After adjusting the necessary parameters I ran the migration with a 2ms sampling rate. This took 11 days to complete, using a sunV880 single processor. In order to speed up the migration I resampled the data to 4 ms which improved the efficiency.

My initial impression of the migrated gathers (Figure 4.3) was that the long offsets became stretched in the shallow section. Stacking these gathers had a blurring effect on the data, as illustrated in Figure 4.4a.



**FIG. 4.3.** Representative PSTM common image point gathers. Events above the area indicated by red line were stretched and had to be muted for the stacking purpose.

To remove these artifacts I muted the stretched events (Figures 4.4a, 4.6a, and 4.8a), restacked the migrated gathers (Figures 4.4b, 4.5b, 4.6b, 4.7b, and 4.8b) and normalized each output sample by the number of input samples (Zheng et al., 2002). This gave a much improved and more focused result, as illustrated in Figures 4.4b, 4.6c, 4.8c, and 4.9b which display 3 different lines.

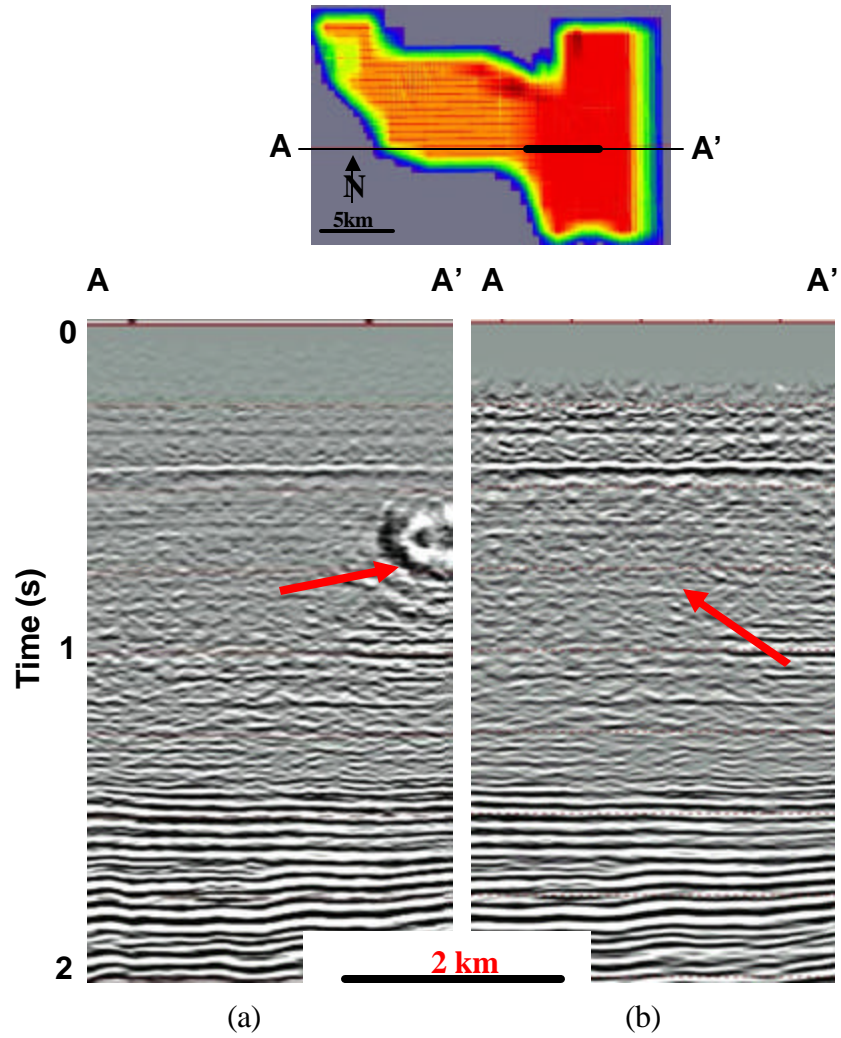


**FIG. 4.4.** PSTM section (a) before and (b) after far offset mute using normalization during the stacking. The red arrow on (a) indicates low frequency artifacts due to stretching on the far offsets. The red arrow on (b) points in the direction of linear noise that has leaked through the migration.

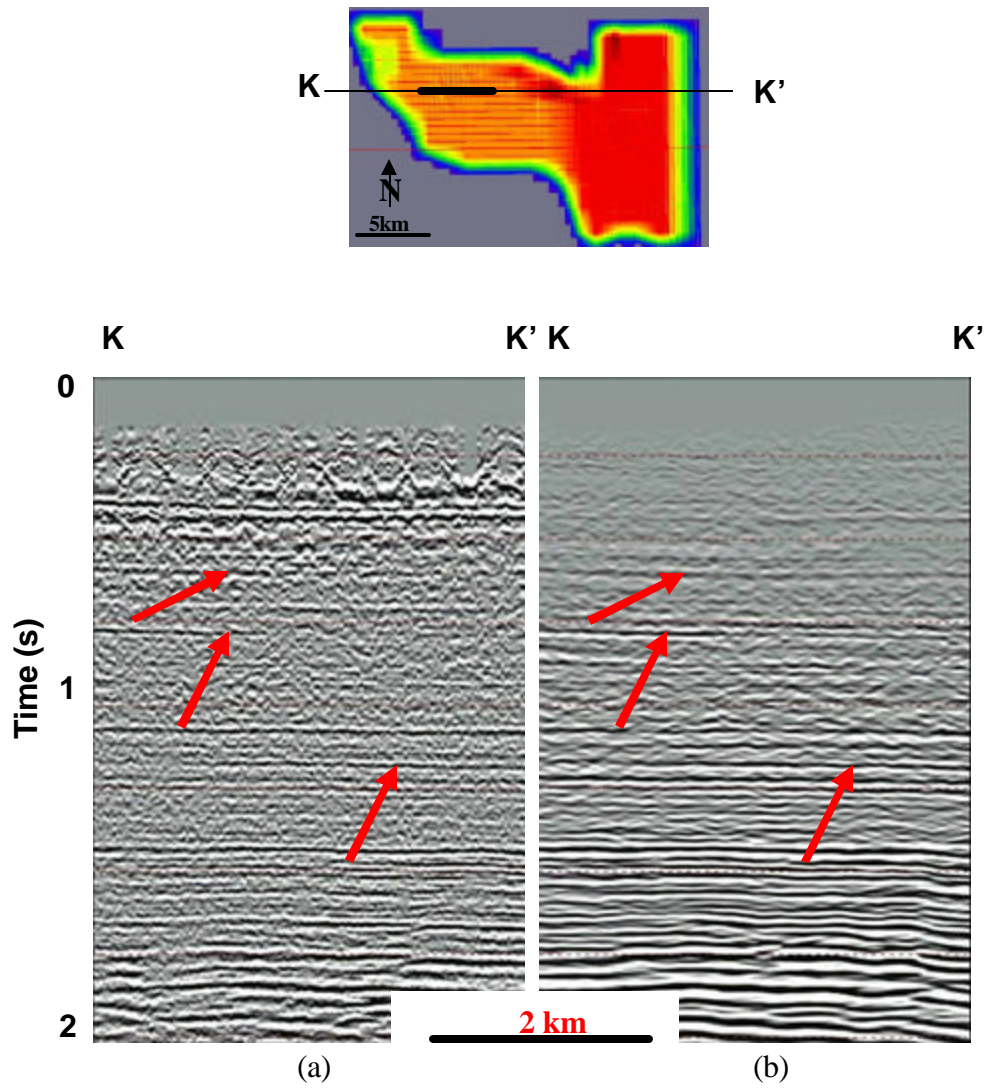


**FIG. 4.5.** Stacked section (a) before PSTM and (b) after PSTM with the mute applied. The red arrows indicate sharper events after migration.

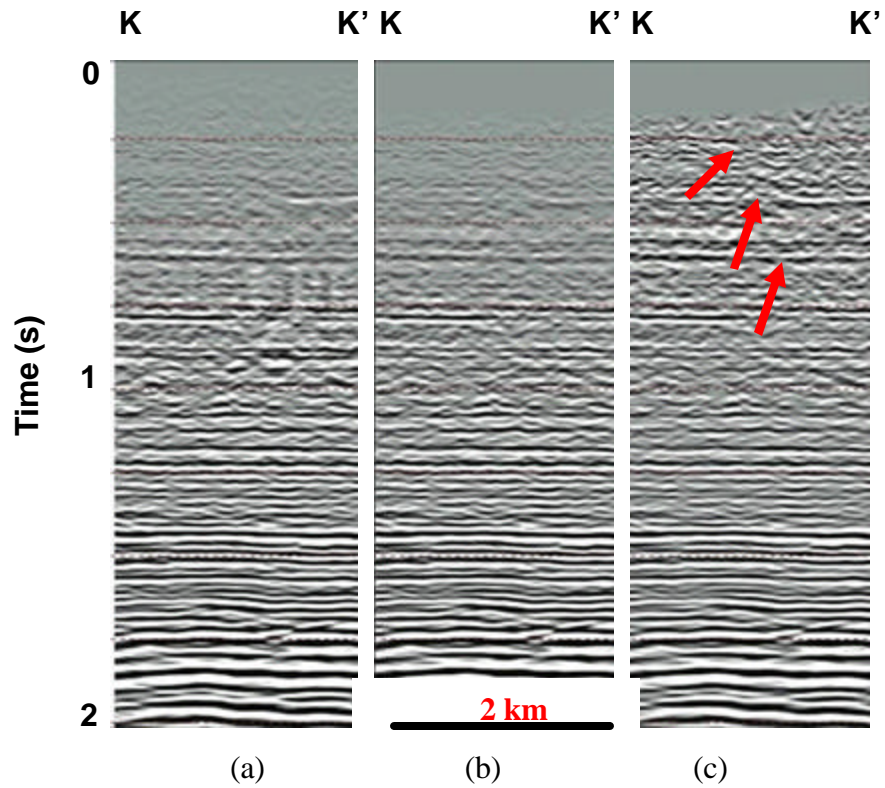


**FIG. 4.6.** Stacked section (a) original PSTM, (b) with mute to remove stretched events and (c) using the normalization procedure already explained in the text. The arrivals indicated by red arrows are much stronger on (c). The red arrows indicate sharper events after migration. The position of the section in the field is displayed on Figure 4.5.

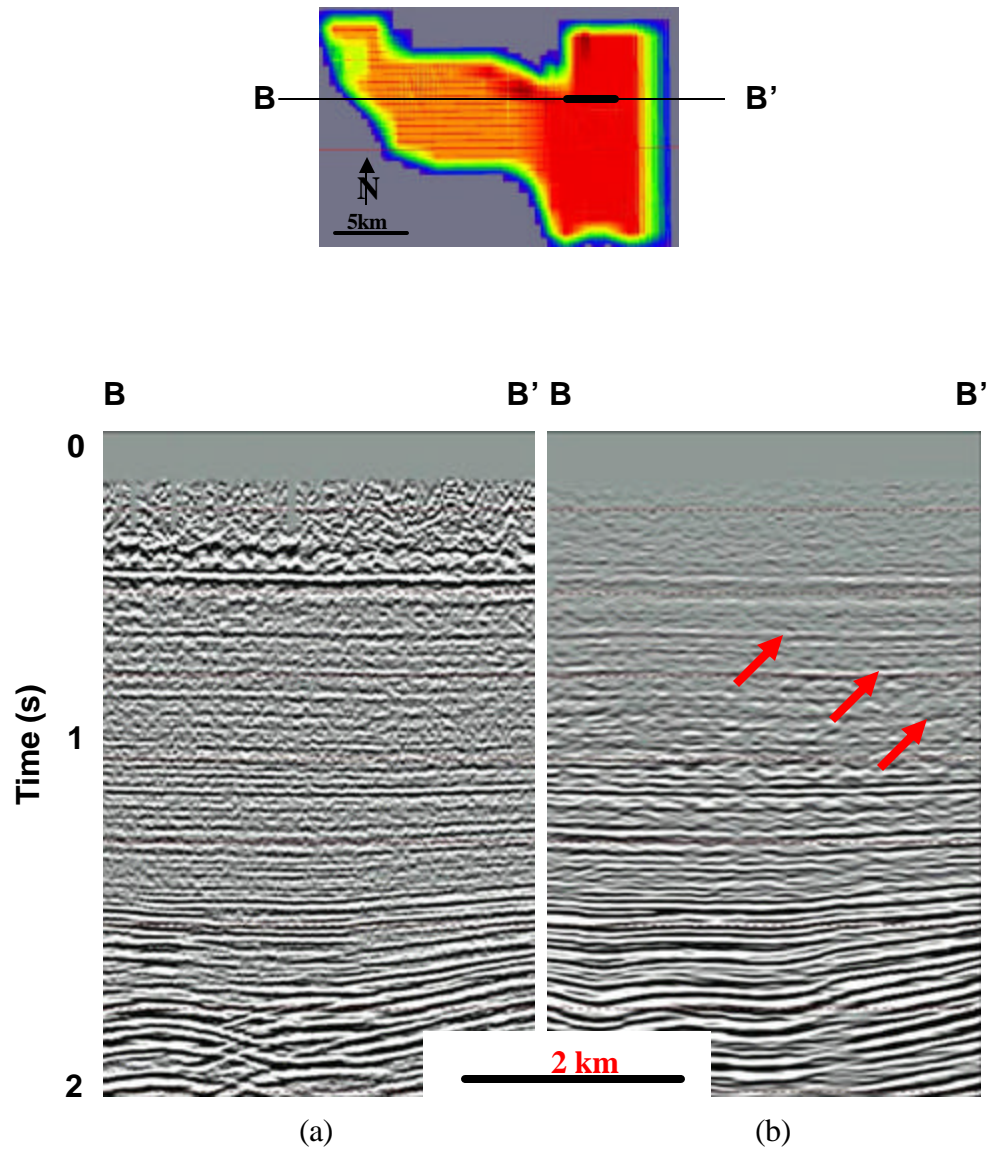


**FIG. 4.7.** Stacked section (a) before PSTM and (b) after PSTM with the mute applied. The red arrows indicate sharper events after migration.

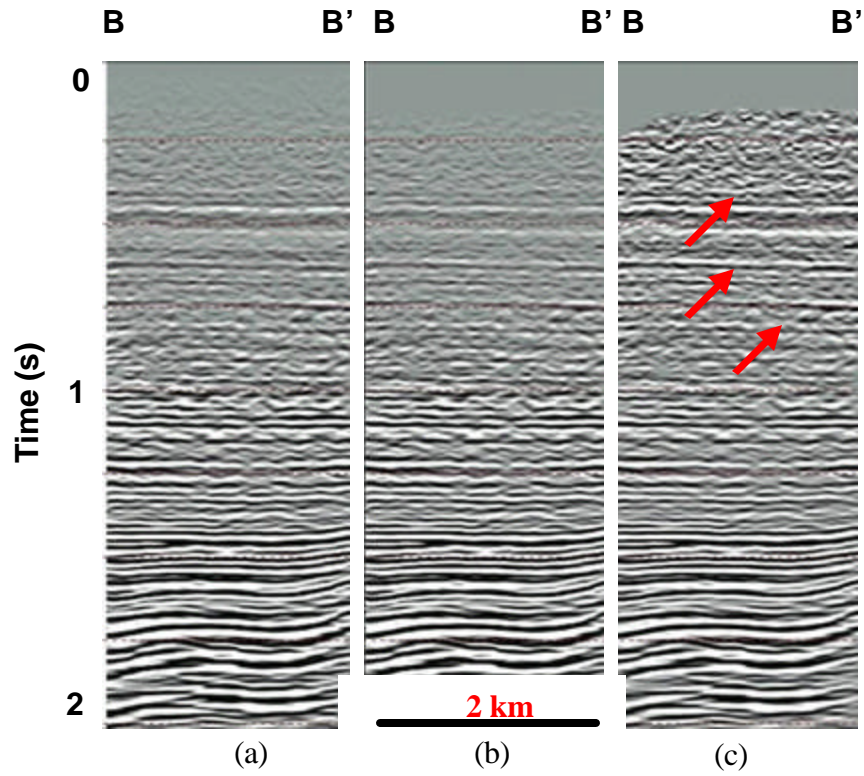


**FIG. 4.8.** Stacked section (a) original PSTM, (b) with new mute to remove stretched events and (c) using the normalization procedure already explained in the text. The arrivals indicated by the red arrow are much stronger on (c). The red arrows indicate sharper events after migration. The position of the section in the field is displayed on Figure 4.7.

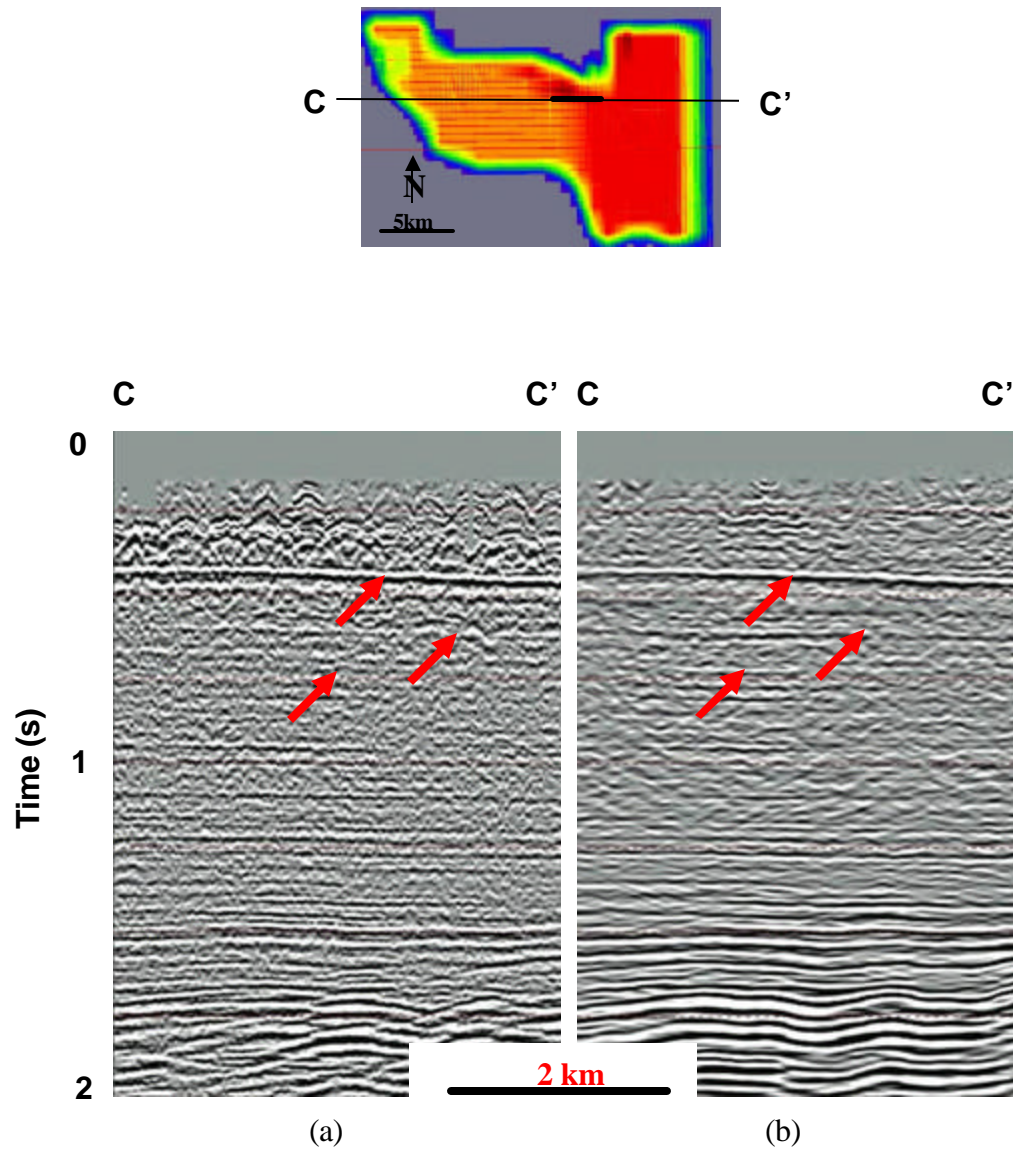


**FIG. 4.9.** Stacked section (a) prior to PSTM and (b) post PSTM including normalization and mute. The red arrows indicate events sharpened after migration (b).

After the first iteration of migration I picked the residual velocity, represented by finer moveouts that could be fixed by picking again on the coarse velocity grid. Since the velocities did not change dramatically, I decided not to apply a second pass.

Finally, I cosmetically muted the extent of my migrated volume to represent the extent of my acquisition (Figure 4.10).

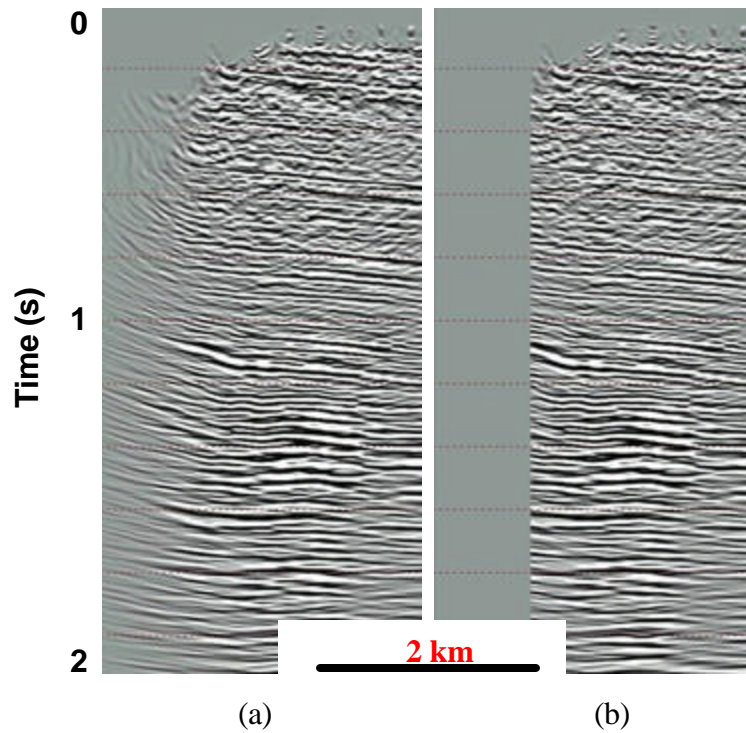


**FIG. 4.10.** Trace editing using Focus program AREA3D to eliminate migration “smiles” at the edge of the survey: (a) before and (b) after editing.

### 4.3. Anisotropic Pre-stack Time Migration

In order to test the validity of improvements attributed to accounting for anisotropy, I had to pick a fourth order velocity parameter,  $\eta$  (Appendix A). Constrained by the time taken to run these migrations, resample the data to 4 ms resulting in a 6 day migration period.

Comparing the stacks from the isotropic and anisotropic migration (Figure 4.11, Figure 4.12, Figure 4.13, and Figure 4.14), I note that both displays improved vertical and lateral resolution. In particular, I note there is a marked improvement in both, the continuity of events and the enhanced focus of the reflectors in the shallow section..

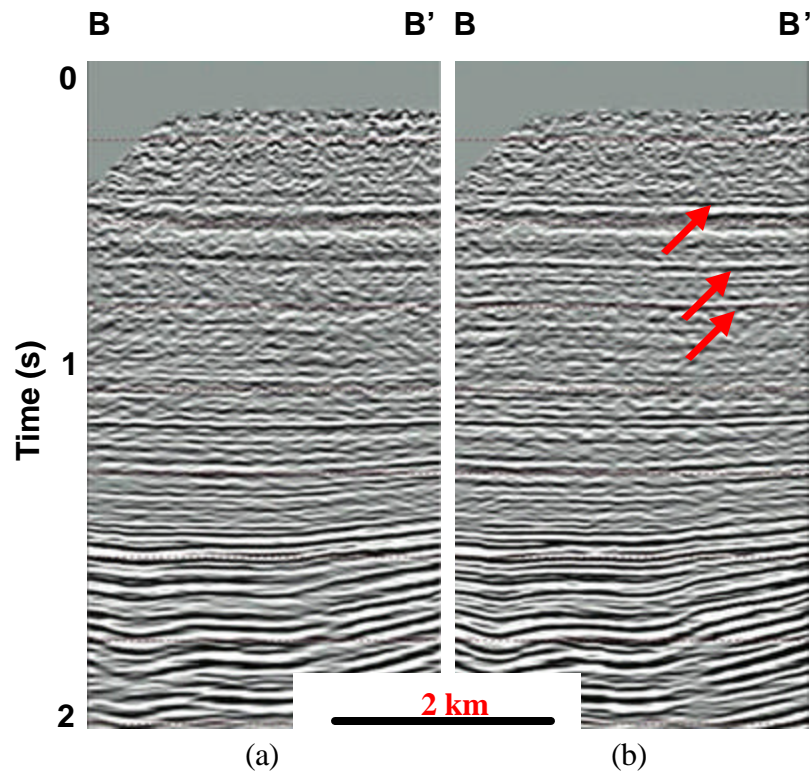


**FIG. 4.11.** PSTM stack (a) after isotropic migration and (b) after anisotropic migration. The location of the stacked section is the same as in Figure 4.7. The red arrows on (b) highlight how specific reflectors have been “sharpened”.

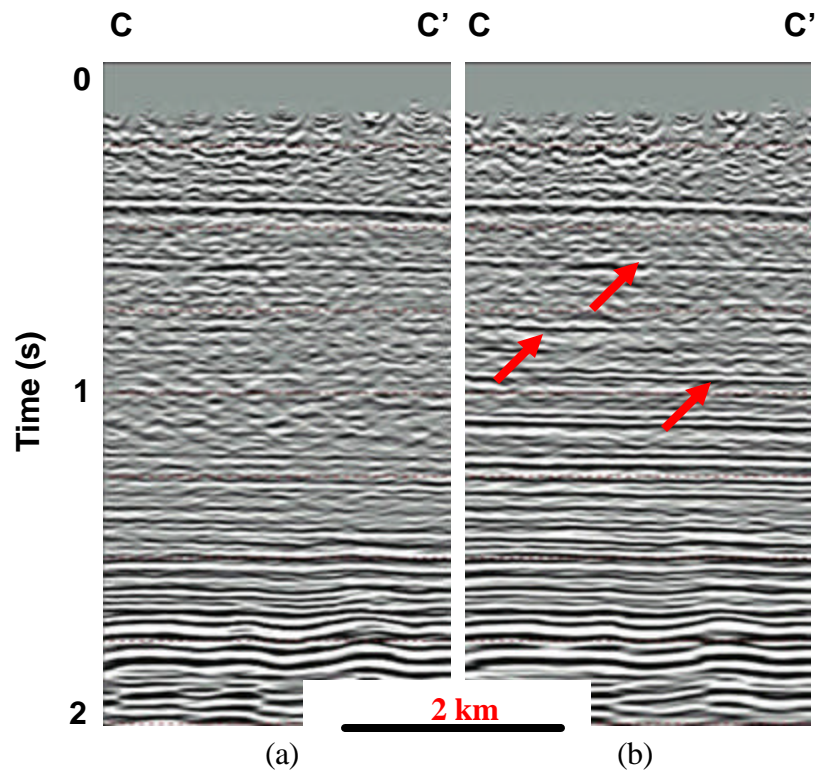


**FIG. 4.12.** PSTM stack after (a) isotropic migration and (b) anisotropic migration and normalization. The location of the stacked section is the same as in Figure 4.9. The red arrows on (b) highlight how specific reflectors have been “sharpened”.

In Figures 4.11 and 4.12, I applied both the same mute prior to stacking procedure due to the same stretching problem, and normalization during stacking. Further analysis of the gathers showed the reflections were flat and that they not require any residual ? picks or any additional migrations runs.

In order to see better where the problems of anisotropy start, I made stacks of 3 sets of offset ranges: 0-1000 m, called “near”, 1000-2000 m, called “mid” and 2000-3000 m, called “far”. The stretching mute used in both earlier stacks is the same one used in these. Results are shown on the Figures 4.13, 4.14, and 4.15.

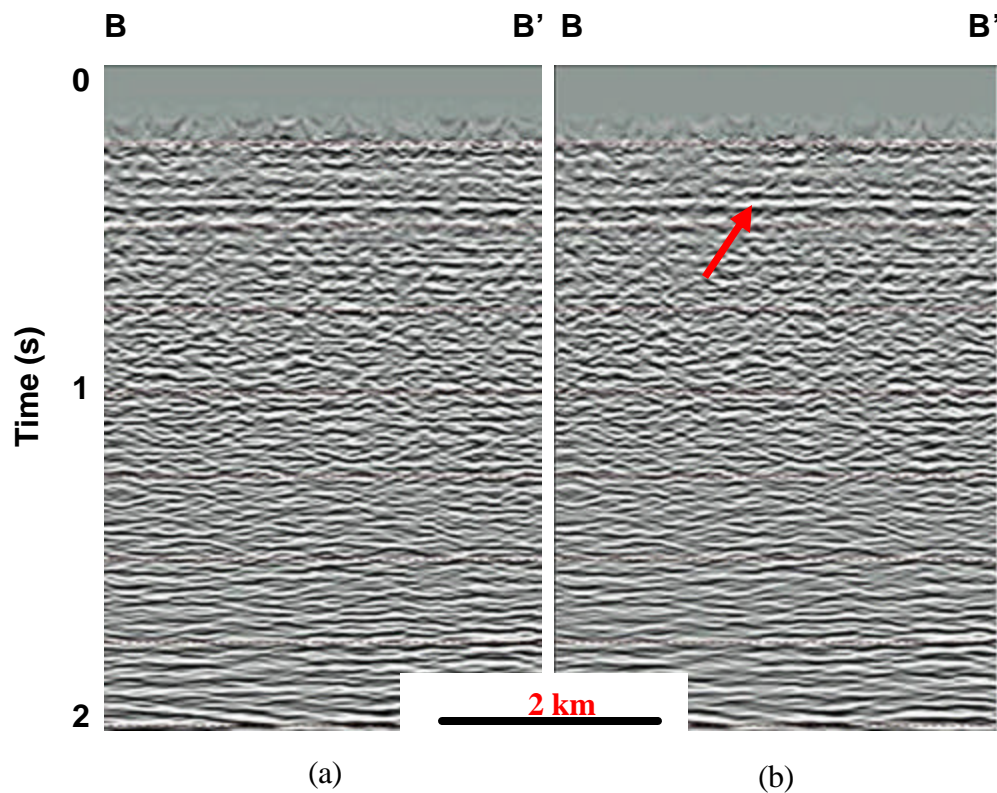


**FIG. 4.13.** Stacked section with: (a) isotropic near offset range 0-1000m, (b) anisotropic near offset range 0-1000m. Position of the stack section is the same as in Figure 4.7. Near offsets contain very little information about the shallow portion due to the high noise level. The red arrows indicate the arrivals that could be of interest.

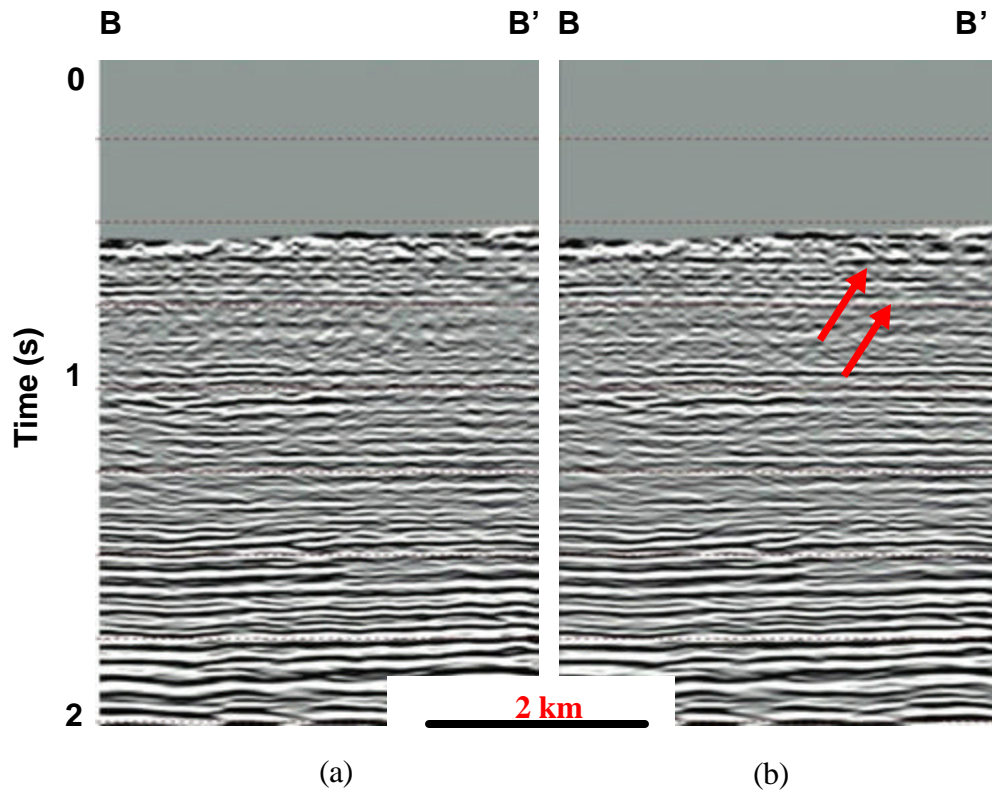


**FIG. 4.14.** Stacked section with: (a) isotropic mid offset range 1000-2000m, (b) anisotropic mid offset range 1000-2000m. Position of the stack section is the same as in Figure 4.7. Events of interest are highlighted on the mid offset. The red arrows indicate the arrivals that could be of interest.

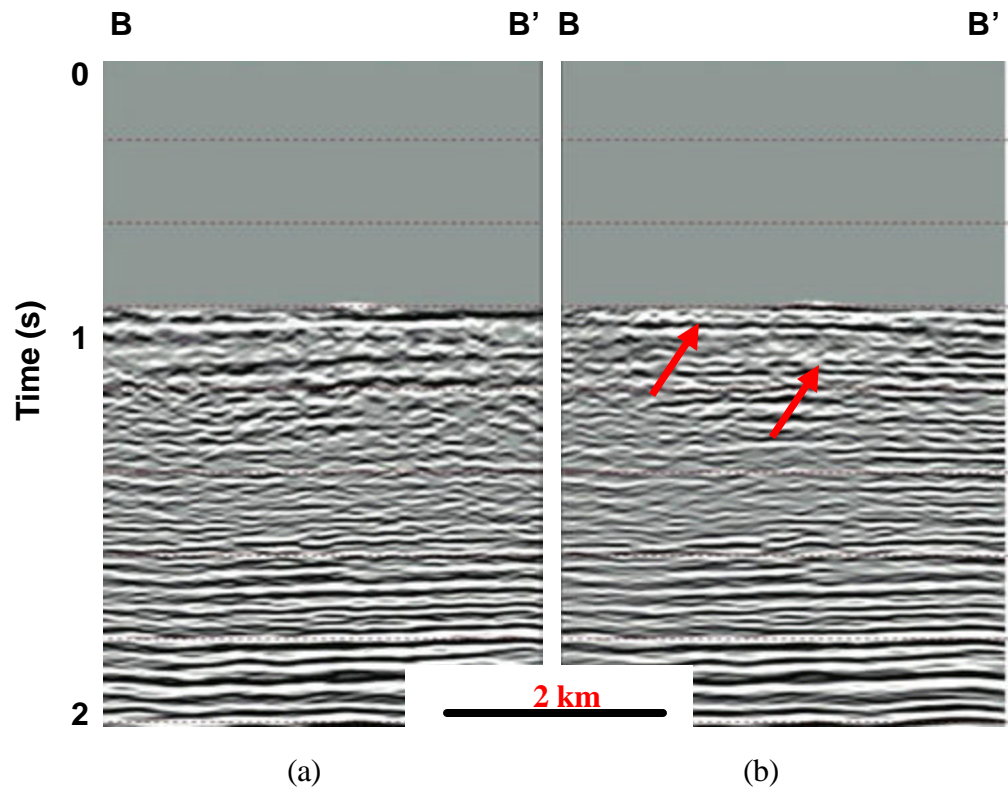


**FIG. 4.15.** Stacked section with: (a) isotropic far offset range 2000-3000m, (b) anisotropic far offset range 2000-3000m. Far offset section does not image the shallower part (below 1 s). The red arrows indicate the arrivals that could be of interest.

#### 4.4. Testing

After testing both types of the migration, I elected to examine different filtering and cosmetic applications, with a review to enhancing the quality of the trial stacks.

First, I tried running window dip filtering (WNFIL) on the seismic data. The results of testing various filter lengths and weights are shown on Figure 4.16. The filter design is depicted in Appendix B.

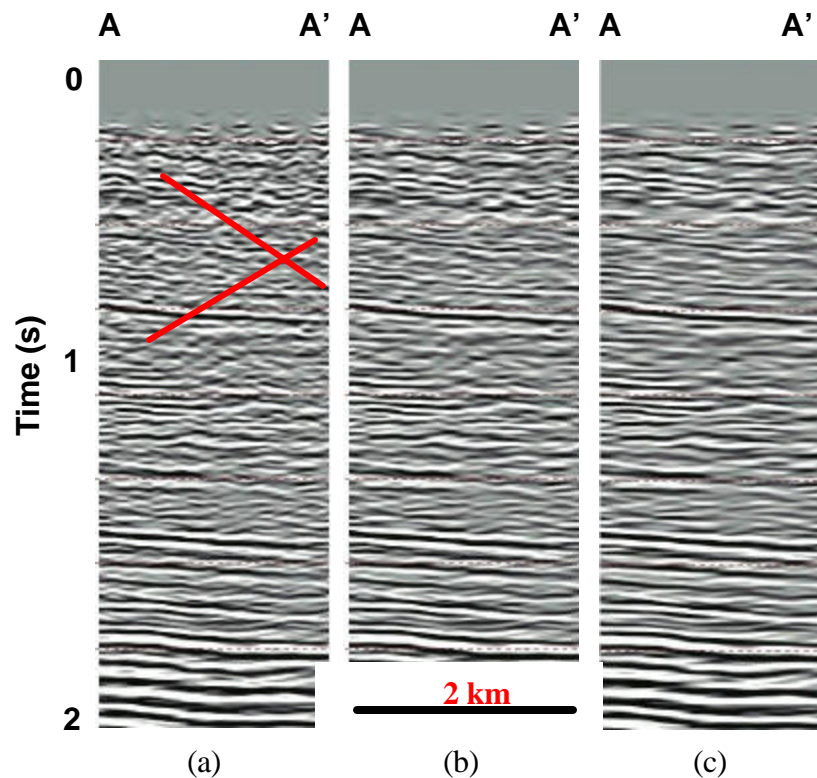


**FIG. 4.16.** Stacked section isotropic PSTM generated using running window filter of: (a) 3 traces (b) 5 traces, and (c) 7 traces. It seems that (c) has the least of dipping crossing events indicated by the red crossing lines on (a). Section (c) is much clearer than other two. The orientation of this section is given on Figure 4.4. However, only half of AA' is displayed here.

The second filter I tested was  $f$ -xy spatial prediction filter (FX-decon), which I used previously in Chapter 2 to precondition the static corrections. The results are highlighted in Figure 4.17.

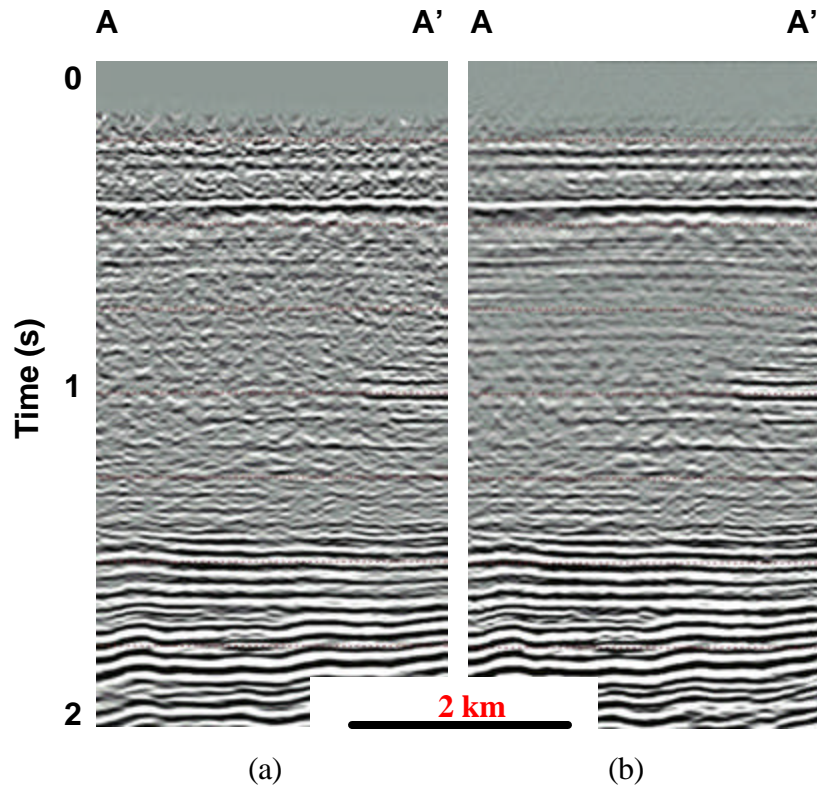


**FIG. 4.17.** Stack isotropic PSTM section: (a) before and (b) after FX decon. The resultant stack is smoother, yet a large amount of data is removed. The location of the stack is given on Figure 4.4.

The third attempt to improve data appearance incorporated a module called DIGISTK. This module belongs to signal enhancement programs and works as a semblance-weighted filter. The first step is to run SIGNAL which estimates the coherent components of original traces that are aligned in localized regions of space and time. The original traces are then stacked with the SIGNAL traces. The only parameter that DIGISTK uses is weights (WT). Weights dictate how much the signal trace combined with the original one will influence the stack. In this case I used negative weights in order to rid

the data of coherent noise (Focus Help, 2005). The trace summation is the result of the following calculation:

$$(1-WT) \times \text{original trace} + WT \times \text{signal trace.} \quad (4-2)$$

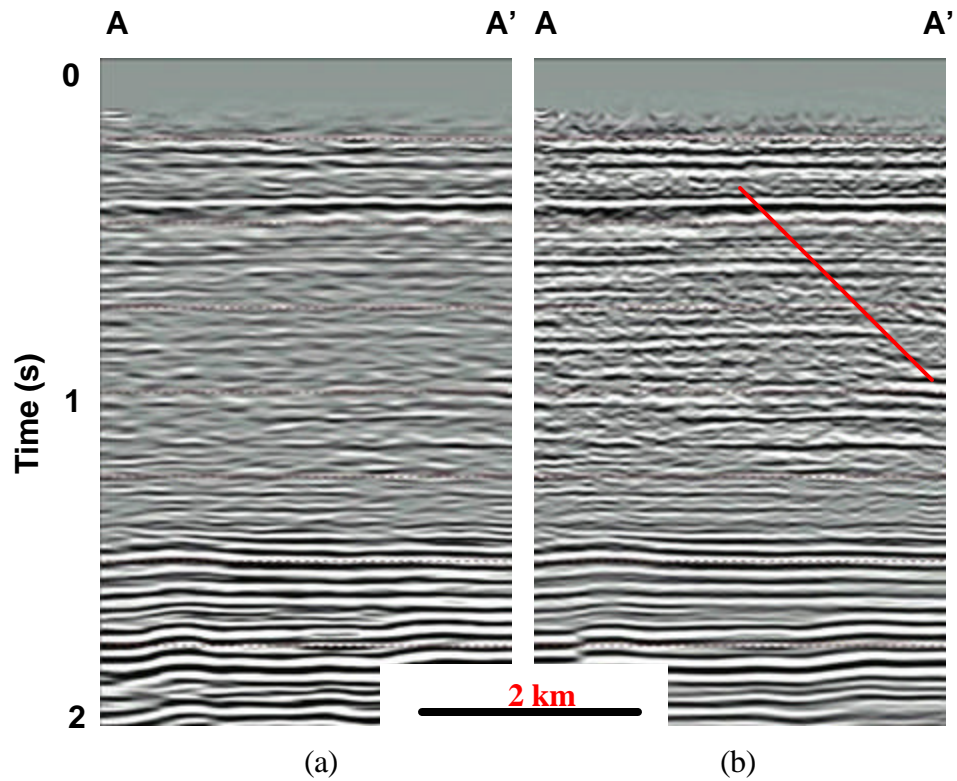


**FIG. 4.18.** Stack section from isotropic PSTM with (a) running window filter including 7 traces, and (b) semblance-weighted filter. (b) Has a huge amount of details and reduced coherent noise, indicated by the red line, compared to the input (Figure 4.17a). The location of the stack is given on Figure 4.4.

Examination of Figure 4.18. clearly shows that semblance-weighted filter gives better results than running window filter. To validate this observation, I will show the Line AA' before and after semblance-weighted filter in Figure 4.19.

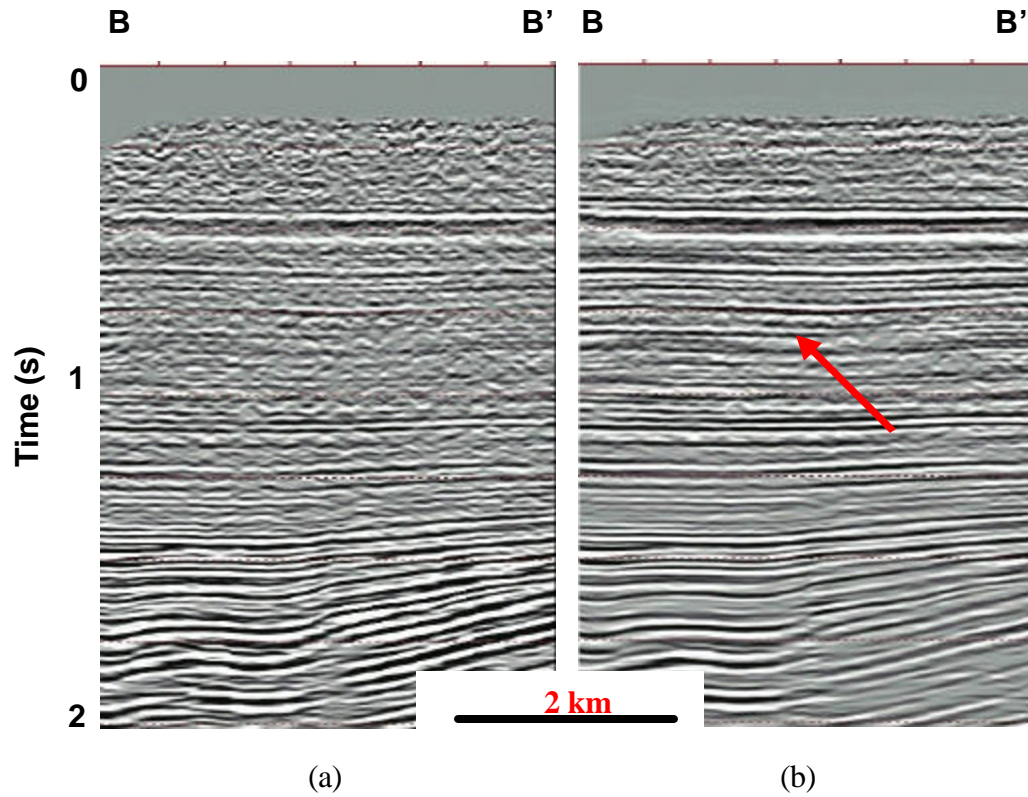


**FIG. 4.19.** Stacked isotropic PSTM section with mute and normalization (a) before and (b) after semblance-weighted filter. Reflection events are clearer and coherent noise is minimized, but not eradicated (red arrow). The location of the stack is given on Figure 4.7.

After semblance-weighted filter application noise was still present and I applied spectral balancing filter, band-pass filter (6, 12, 48, 72Hz) and F-xy spatial prediction filter in order to optimize original sharpening. The outcome is shown in Figure 4.20. Since the processing results were satisfactory, I was ready to proceed with loading the data into the interpretation software package - GeoFrame.

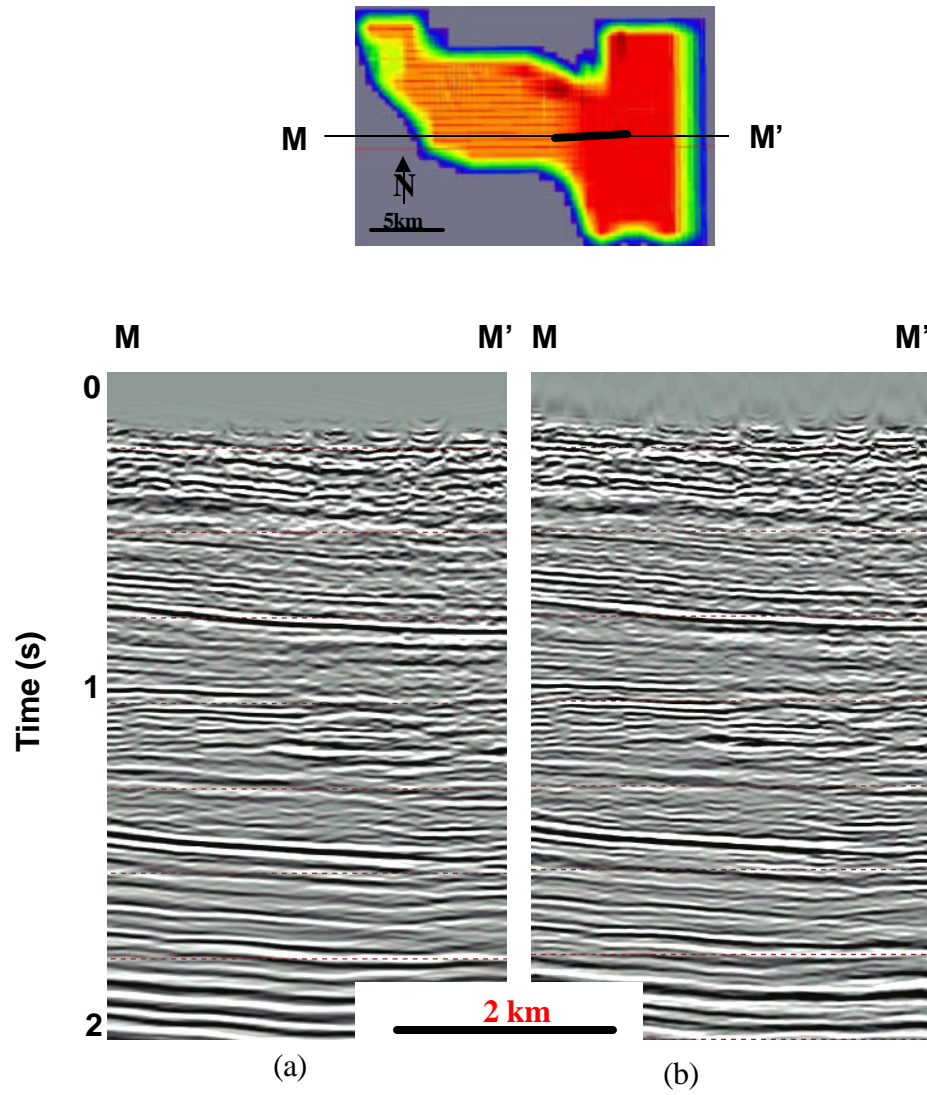


**FIG. 4.20.** Stacked isotropic PSTM section with semblance-weighted filter and applied in succession: (a) spectral balancing, (b) F-xy filter. S/N ration slightly improves.

All enhancement processes presented in this section were applied to both isotropic and anisotropic data sets. Appendix B details parameters used in these testing.

## 5. SEISMIC ATTRIBUTES

### 5.1. Introduction

Seismic attributes represent any measure of seismic data that helps to better visualize or quantify features of interpretation interest. Seismic attributes can be divided into different categories. Volumetric attributes generate a value for each sample of the input data cube. Taner et al., (1979) calculates complex trace attributes including instantaneous envelope, phase, and frequency using the Hilbert transform. Castagna (2003), calculates spectral components of seismic wavelets, while Chopra and Marfurt (2006) use multitrace (geometric) attributes such as coherency, reflector dip/azimuth, coherent energy gradients and curvature. Roberts (2001) addresses surface related attributes by dividing them into three main categories: surface associated, surface derived and surface rendered attributes (Figure 5.1). The “surface associated” attributes are simply slices through precomputed volumetric attribute cubes, while “surface derived” attributes are calculations performed directly on the horizon picks.

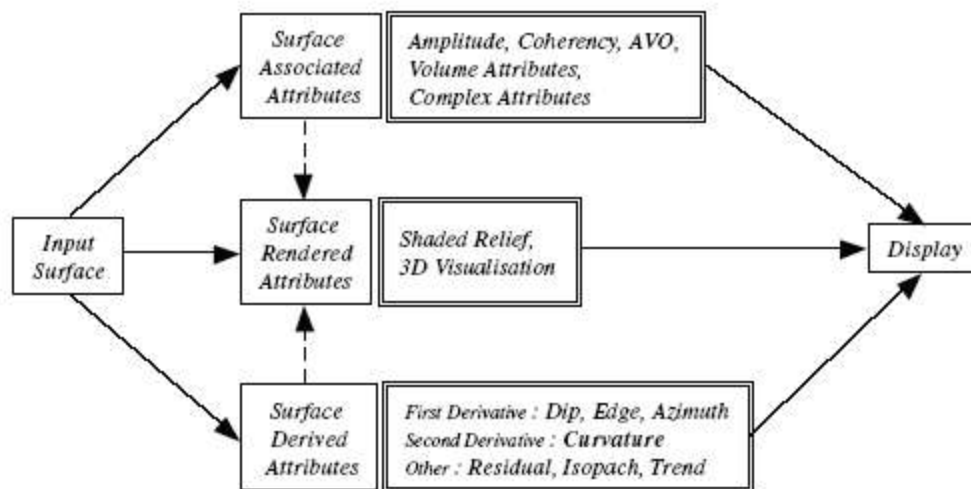
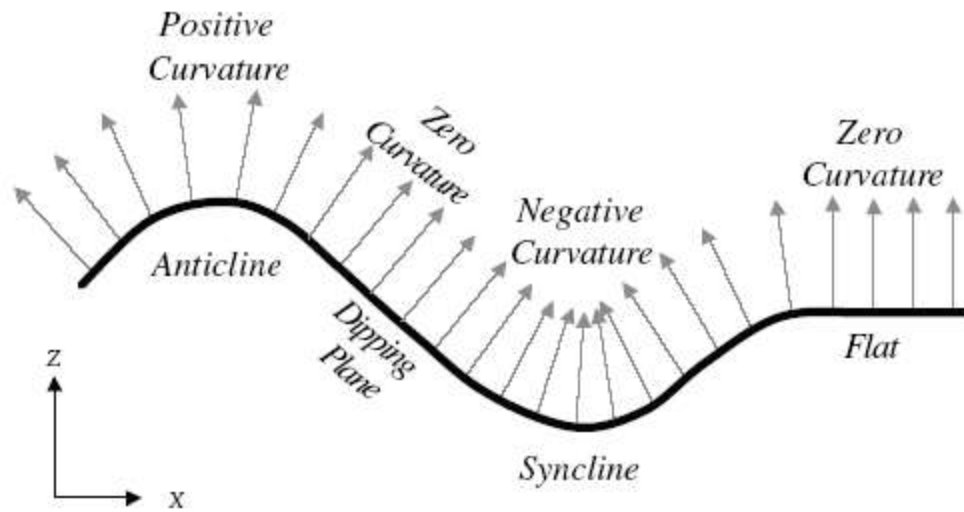


FIG. 5.1. Classification of surface-related attributes (after Roberts, 2001).

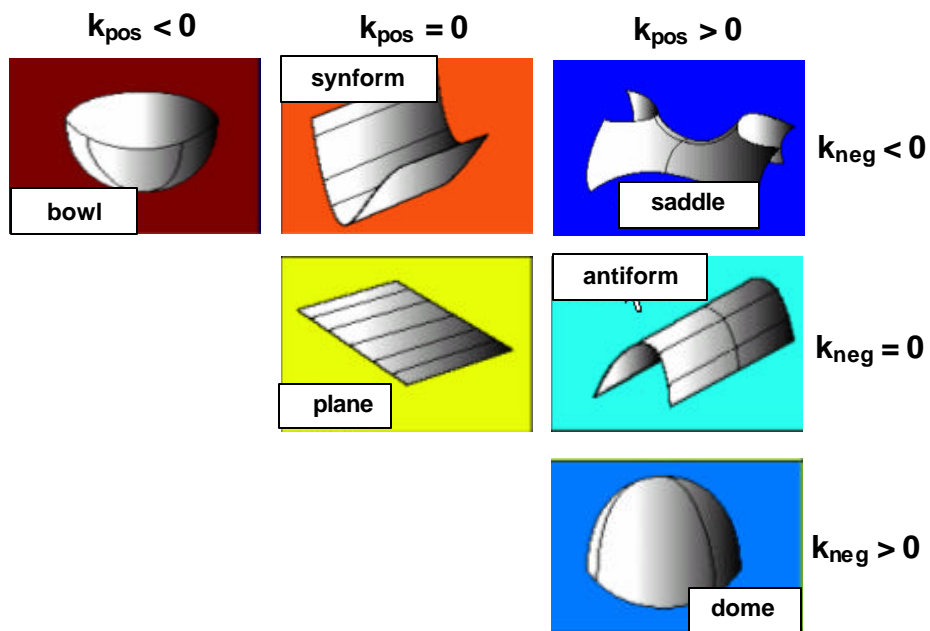
Seismic attributes are sensitive to seismic acquisition and processing and can be used after each processing step as a QC procedure. Seismic data quality directly impacts attribute calculations. The sensitivity of the geometric attributes to seismic data quality can help choose improved processing parameters and flows. In this thesis, I will focus on the application of multitrace attributes.

Coherency presents a measure of similarity between the traces. 3D coherency volumes can be used in the interpretation of subtle structural and stratigraphic features. Most important to this work, faults and channels (as well as acquisition footprints and other data “features”) are easily seen by a processing geophysicist without a great deal of interpretation experience. Furthermore, generation of volumetric attributes is only a fraction of the cost of DMO prestack time migration. Coherency volumes may be generated after different stages of the processing to evaluate processing parameters and to determine that each processing step improves the resolution of geological features that are easily seen on uninterpreted time slices. In this manner, the processor can reexamine key processing steps if the attribute results are not satisfying. Acquisition footprint can be detected, especially on shallow time slices using the same procedure.

Curvature measures change in reflector dip and azimuth. Volumetric curvature calculations are computed from volumetric estimates of dip and azimuth (Al Dassary and Marfurt, 2005). Like coherence, curvature is very sensitive to seismic processing, in particular to errors in velocity in the shallow section that induce artificial domes and bowls. Curvature is sensitive to shape, as illustrated in Roberts (2001) image of 2-D curvature as Figure 5.2a and Bergbauer et al (2004) image of 3-D curvature as Figure 5.2b.



(a)



(b)

**FIG. 5.2.** Sign convention for curvature attributes in: (a) 2-D and (b) 3-D. Zero curvature is in the flat or dipping areas, negative in synclines and positive in anticlines. As we can see from the picture, curvature carries the shape information (after Roberts, 2001 and Bergbauer, 2003).

## **5.2. Maljamar-Vacuum Results**

I generated geometric attributes using code written by colleagues at AGL at the University of Houston. I analyzed two seismic input volumes: one isotropic and one anisotropic. Comparisons of the results of isotropic versus anisotropic velocity analysis and migration are shown on the Figures 5.3 - 5.16.

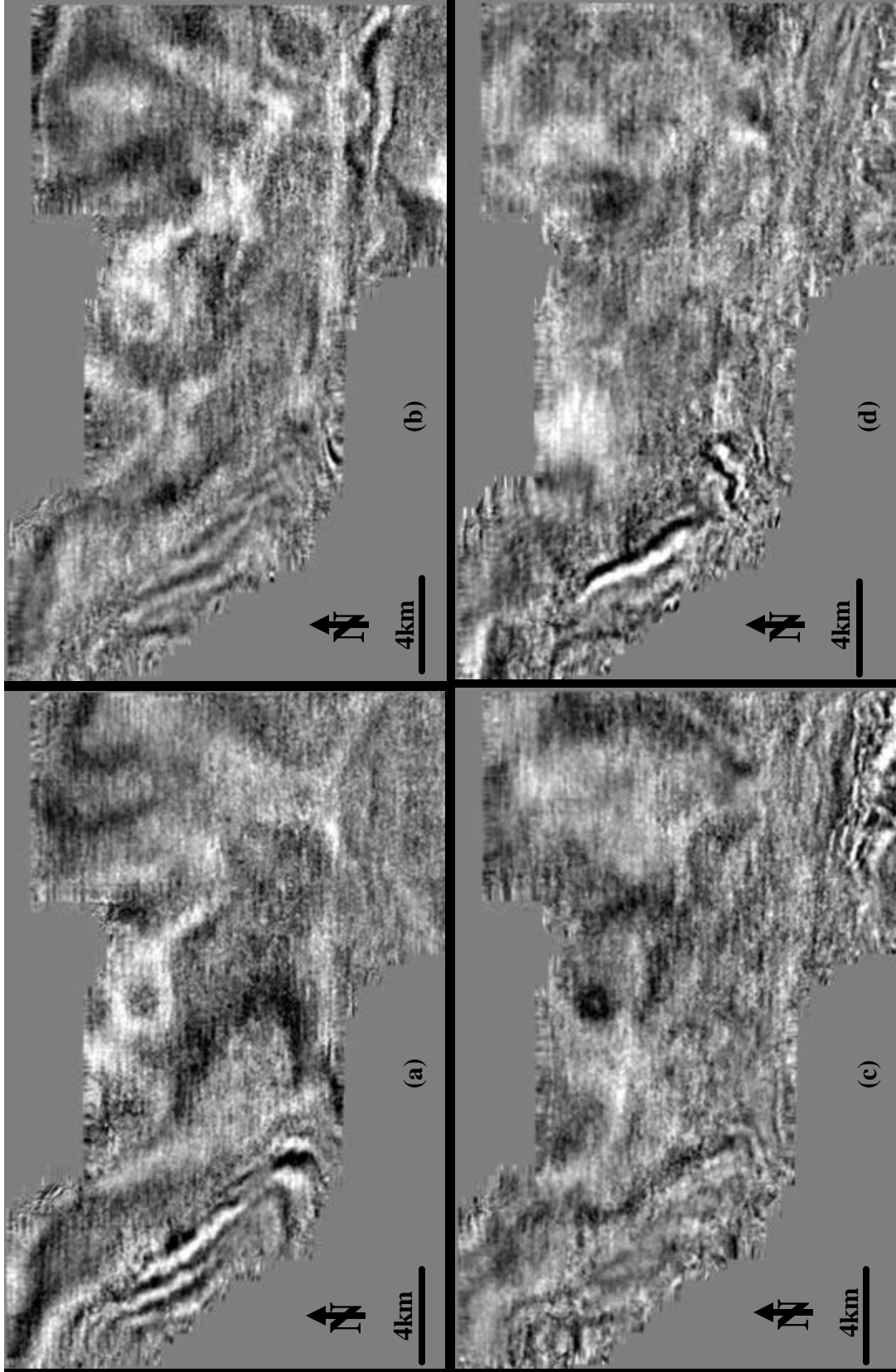


**FIG. 5.3.** Isotropic PSTM time slice: (a) 0.7 s, (b) 0.8 s, (c) 0.9 s and (d) 1 s.

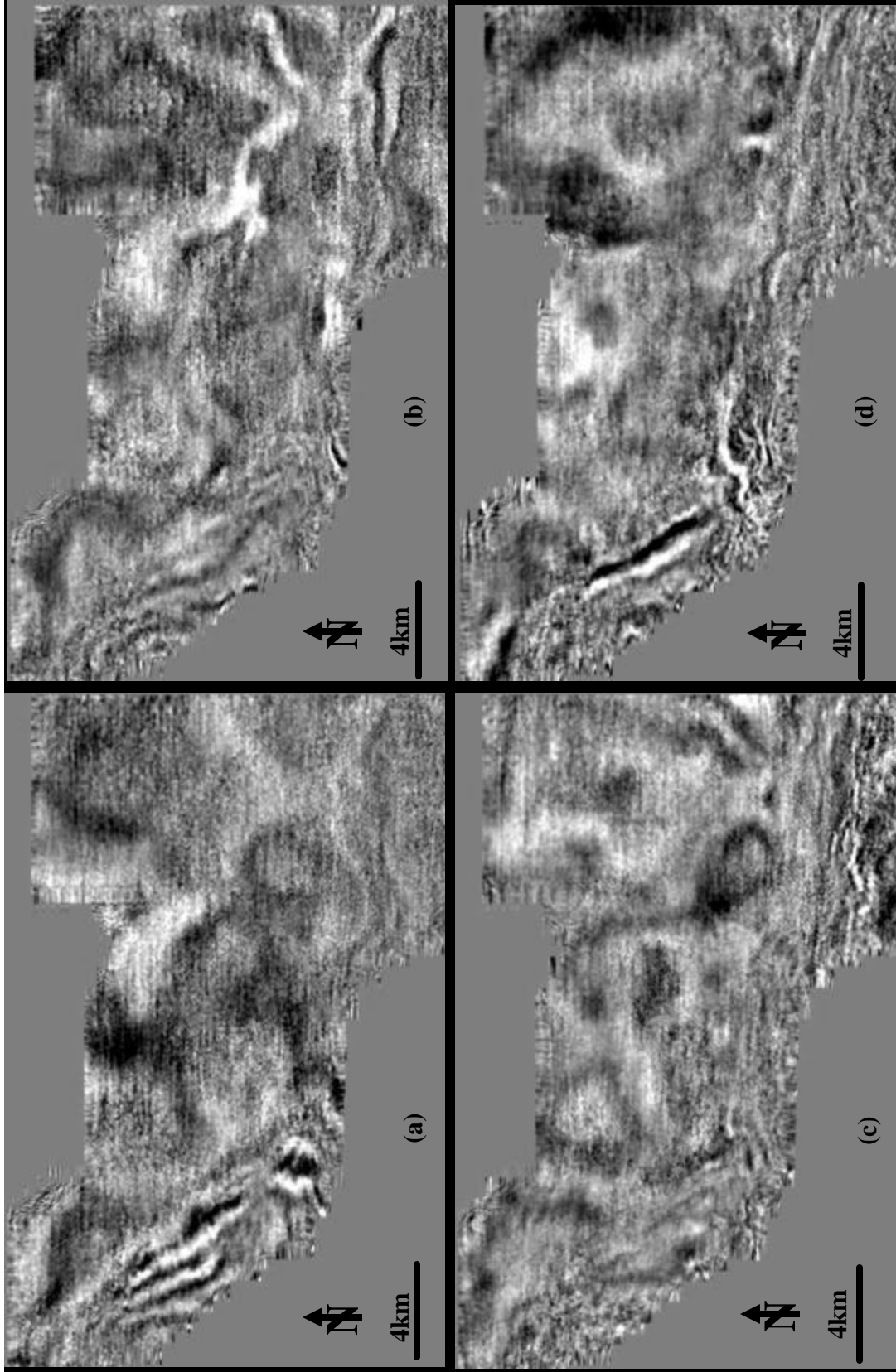
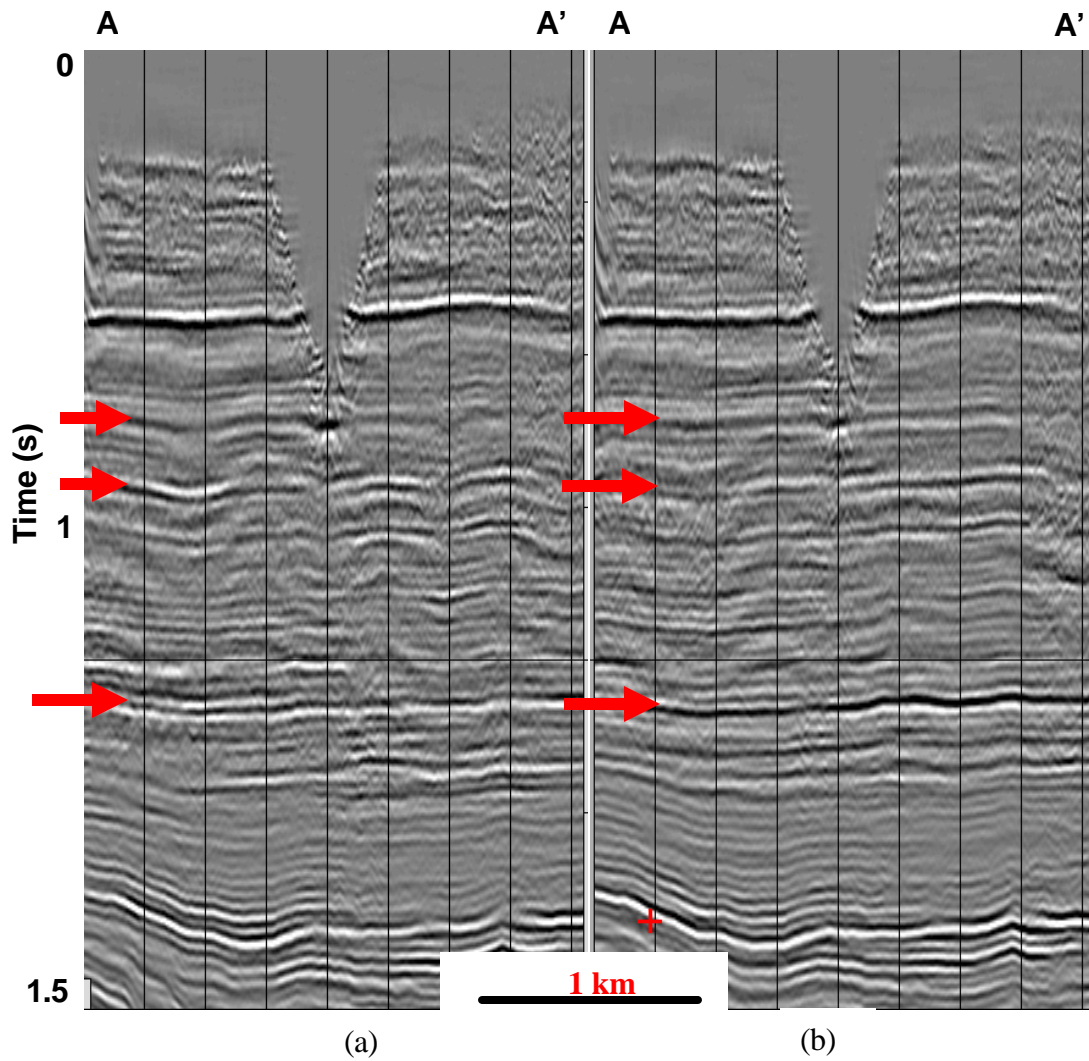
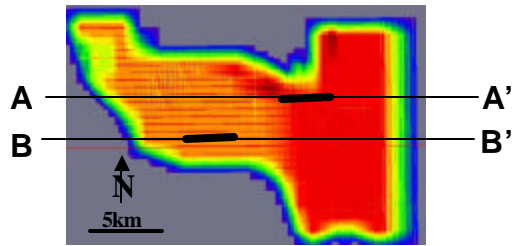
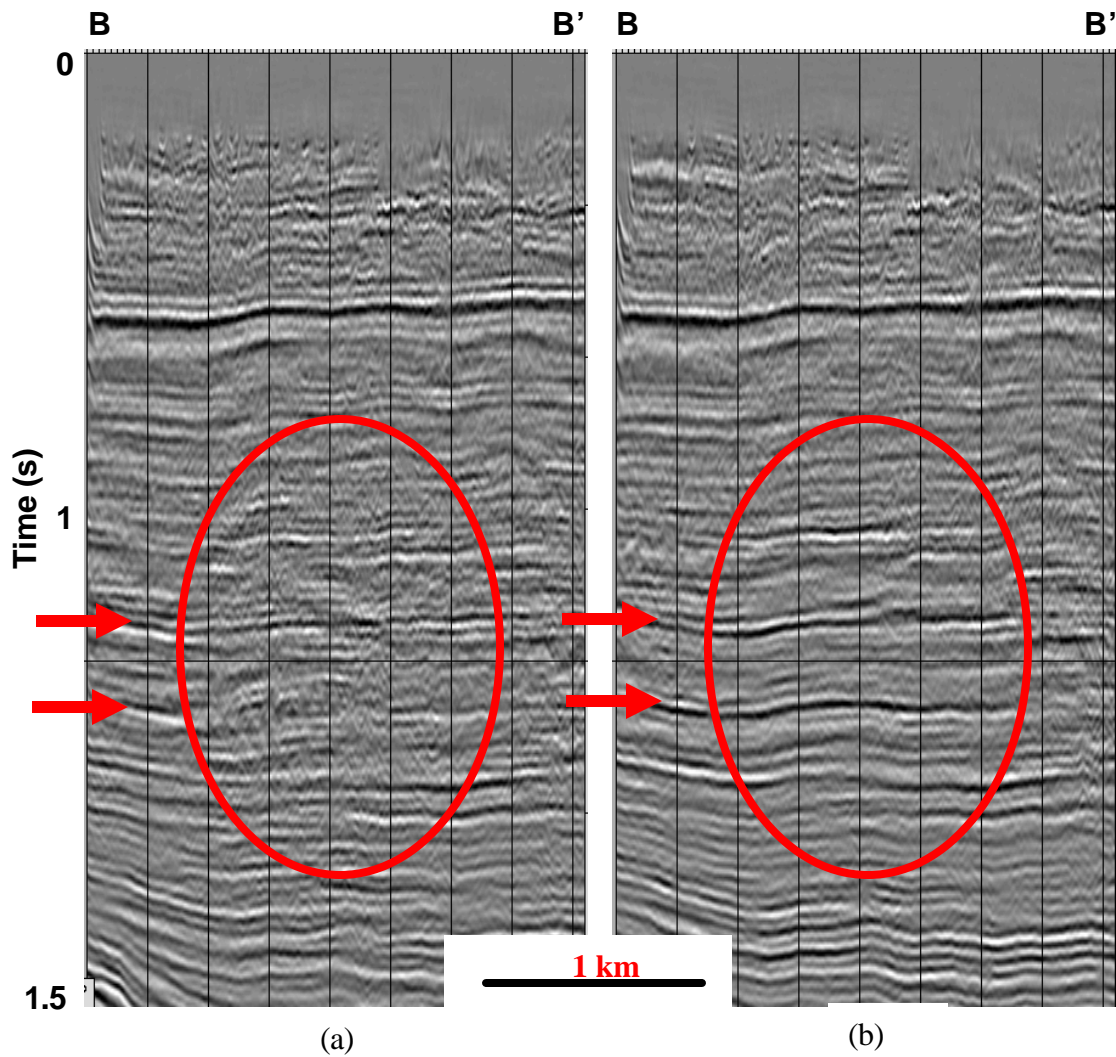


FIG. 5.4. Anisotropic PSTM time slice: (a) 0.7 s, (b) 0.8 s, (c) 0.9 s and (d) 1 s.

Acquisition footprint appears as a rectilinear pattern on both the isotropic and anisotropic images, but it is slightly stronger on the isotropic images at 1 s. On the shallow time slices the fold is low. However, the structure is significantly different at the target level at 0.7 s and 0.8 s. This structural difference is due to velocity. Comparing Figure 5.3d and 5.4d, the Southwest part of the survey at 1 s has an anisotropic time slice with much improved lateral resolution. Examining Figure 5.8 shows that the isotropic velocity analysis and imaging introduced structure, which does appear on the anisotropic images. While the real structure at 1.5 s shows continuous events, the false structure at 0.7 s and 0.8 s in Figure 5.5a shows discontinuous reflectors that fade in and out with the structure. These same events are flattened and more continuous in Figure 5.5b. In Figure 5.6, I show the impact of using more traces in generating the final prestack time migrated image with an anisotropic algorithm.



**FIG. 5.5.** PSTM vertical section AA': (a) isotropic, (b) anisotropic. The red arrows highlight the more continuous horizons produced by the anisotropic imaging.



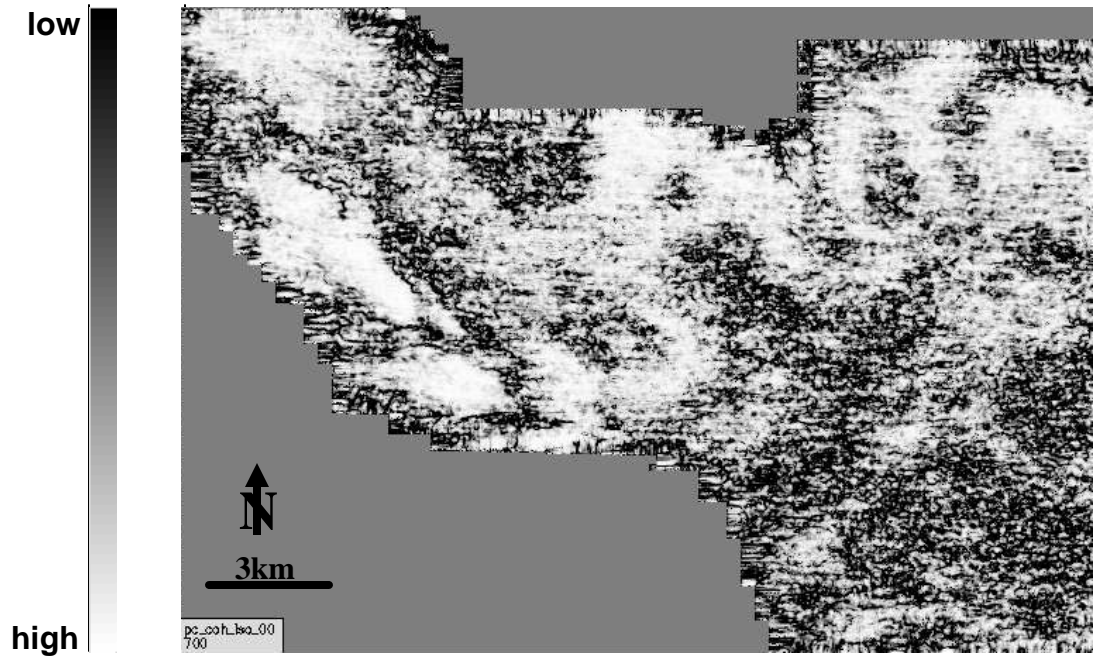
**FIG. 5.6.** PSTM vertical section BB': (a) isotropic, (b) anisotropic seismic data section. The red arrows indicate that horizons are more continuous in (b) than in (a). The red circles indicate areas that are noisier, probably due to the lower fold (limited offsets) of the final isotropic prestack time migration. Section (b), however, shows reduced noise. The aliased steeply dipping noise on (a) is a consequence of unresolved ground roll which create artifacts. The aliased noise leaks into the stack as a spatially periodic event, can also show itself as a footprint (Chopra, 2000).

The acquisition footprint is based on source/receiver spacing and orientation. The coarser the acquisition grid lines the more severe the footprint. Since the geometry in the land situation is fairly regular, the footprint mimics grid periodicity. Fold variation represents the simplest form of the acquisition footprint. Traces with lower fold will appear to be noisier after normalization. In addition, each bin has a different distribution of offsets and azimuths and according to the CMP stack of all the traces in bins, we are able to see bin-to-bin amplitude variations that can produce an acquisition footprint, which Hill (1999) calls “offset driven” acquisition footprint.

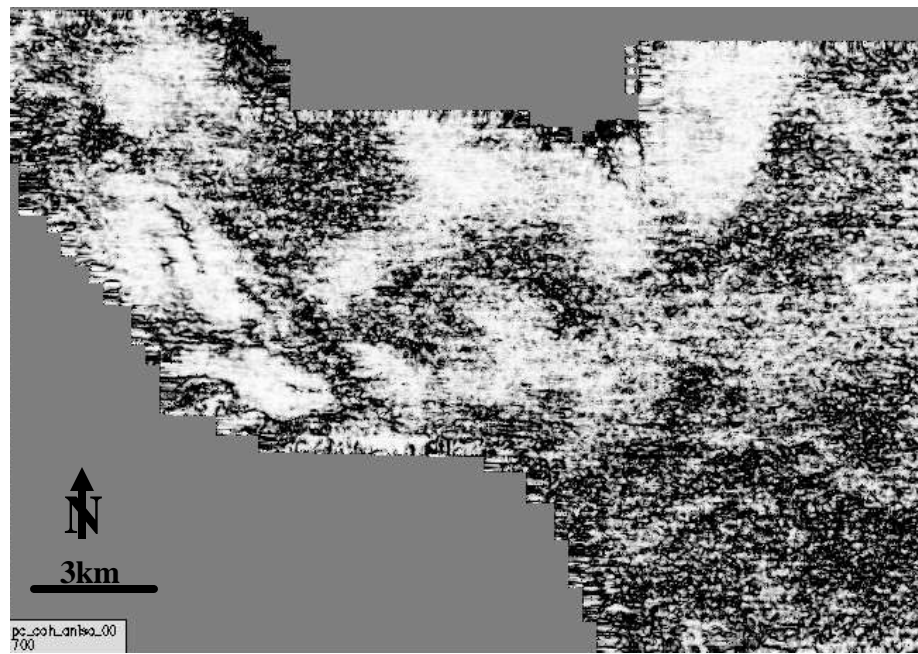
Footprint is dependant not only on the details of acquisition geometry but also on the processing flow (Marfurt et al., 1998). Footprint tends to heal with depth. After errors in velocity, the most prominent acquisition footprint problem comes from ground roll that leaks through the post migration stack (Figure 5.6).

It is evident that in the shallow lower fold part of the Maljamar section (Figure 5.3a) that acquisition footprint is strong and much more obvious on the lower fold isotropic than on the higher fold anisotropic section (Figure 5.4a).

While in general acquisition footprint heals with depth, it can be present in deeper parts of the section if the reflectivity is low (Cordsen, 2004).

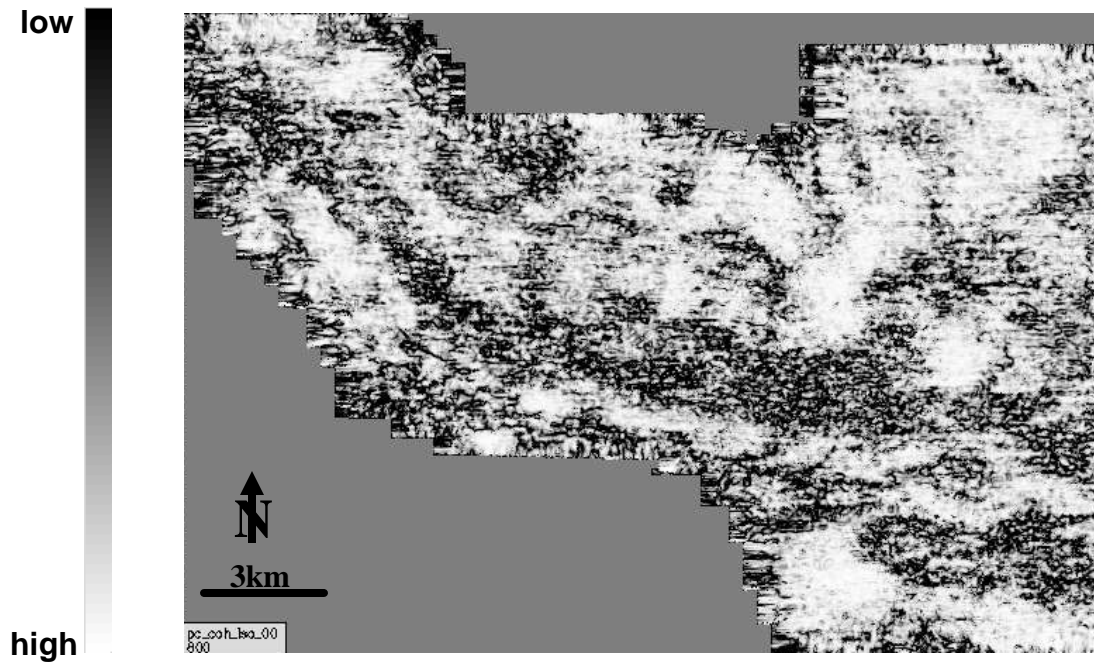


(a)

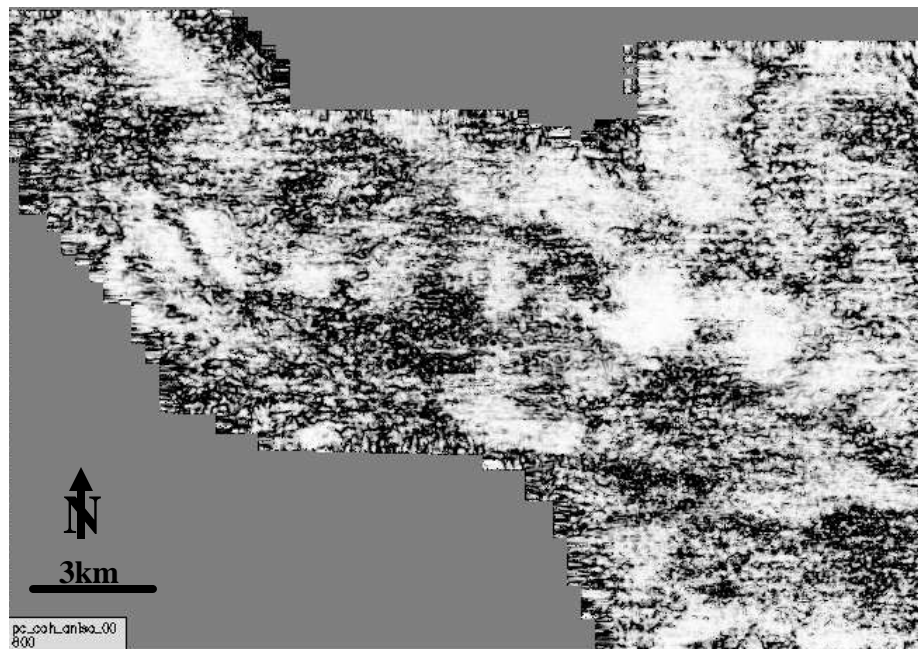


(b)

**FIG. 5.7.** Coherency attributes at 700 ms: (a) isotropic and (b) anisotropic.



(a)



(b)

**FIG. 5.8.** Coherency attributes at 800 ms: (a) isotropic and (b) anisotropic.

Coherency is an excellent tool for detecting footprint during processing (Chopra et al., 2001). As the previous displays show (Figure 5.7-5.8), anisotropic coherency (Figure 5.7b and 5.8b) is slightly better in reducing acquisition footprint and is better focused in different areas comparing to the isotropic one (Figure 5.7a and 5.8a).

Figures 5.10 to 5.13. illustrate corresponding time slices through the curvature volumes. The most positive and the most negative curvatures will be used for mapping lineation, such as folds, faults and flexures. It is also a useful tool for the rectangularized pattern of the acquisition footprint. In Figure 5.9 I wanted to highlight the influence of the acquisition pattern on curvature, so I overlaid the receiver (North-South) and source (East-West) directions onto the curvature map.

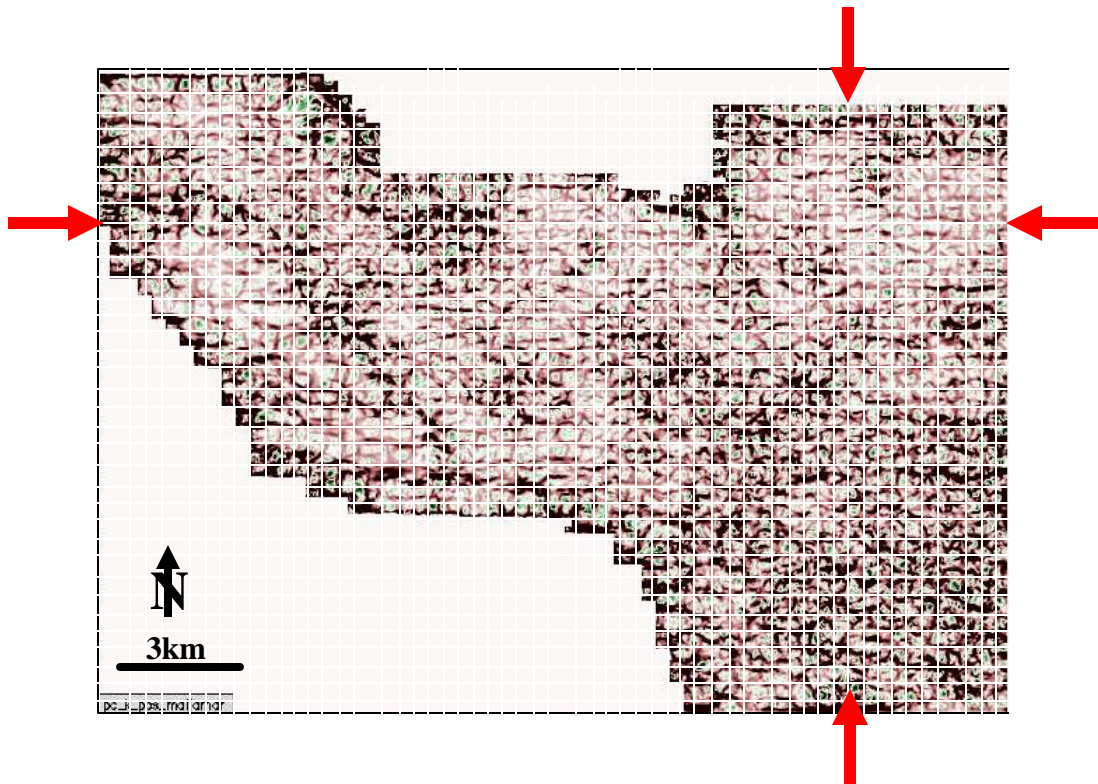
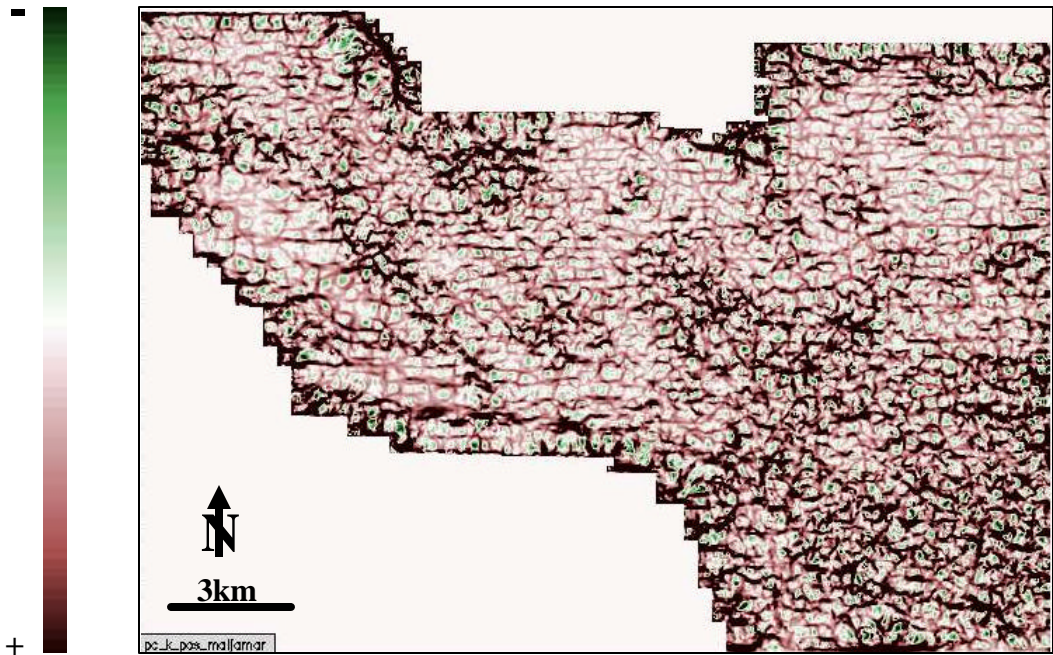
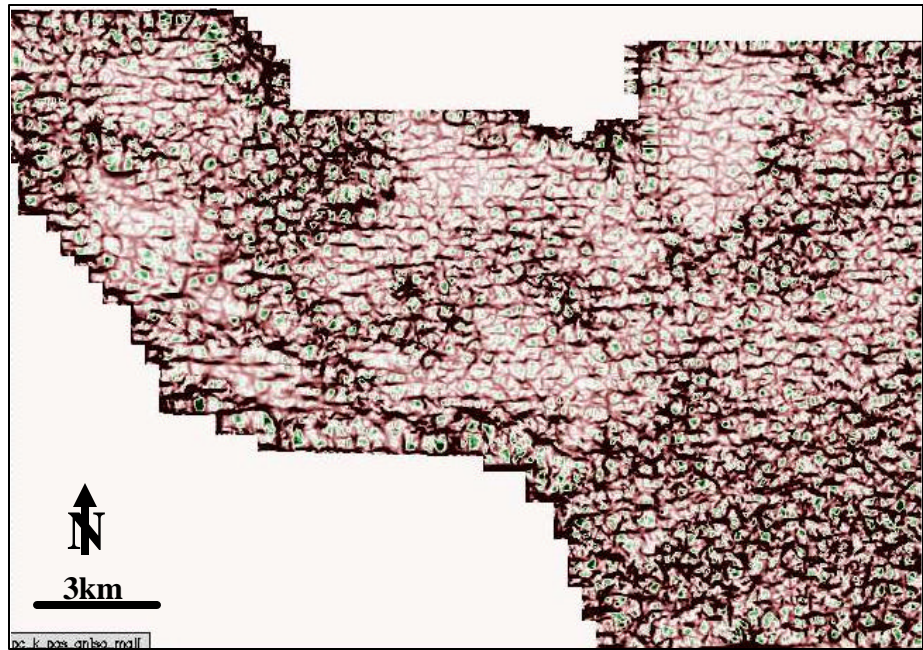


**FIG. 5.9** Positive curvature with source/receiver directions from Figure 5.10. The rectangular pattern of the curvature is overlapping with the geometry of the survey (red arrows) causing the “acquisition footprint”.

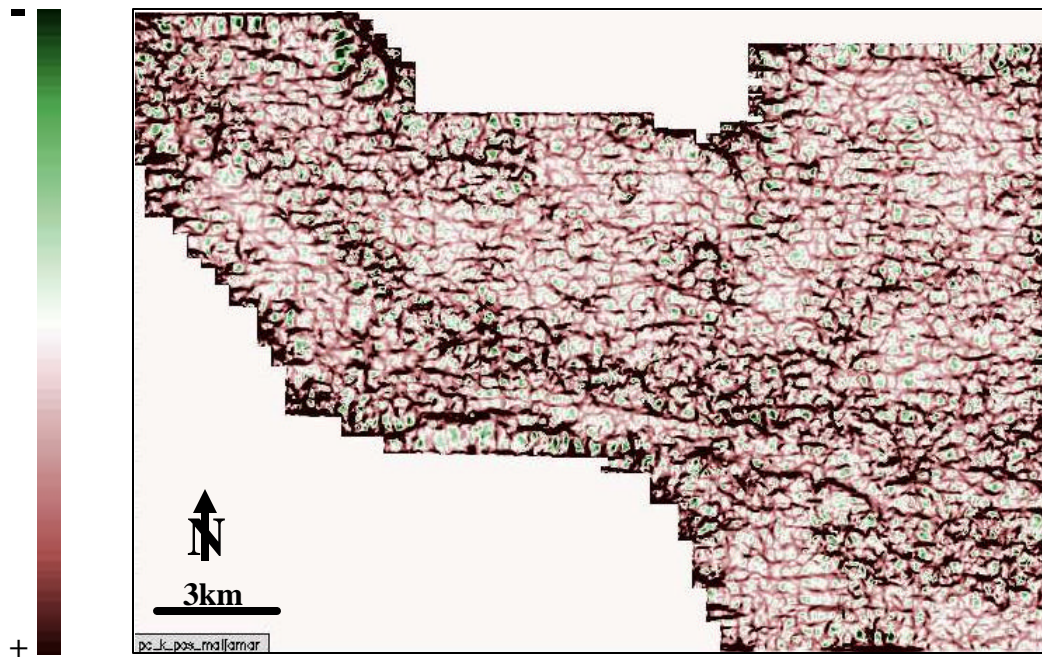


(a)

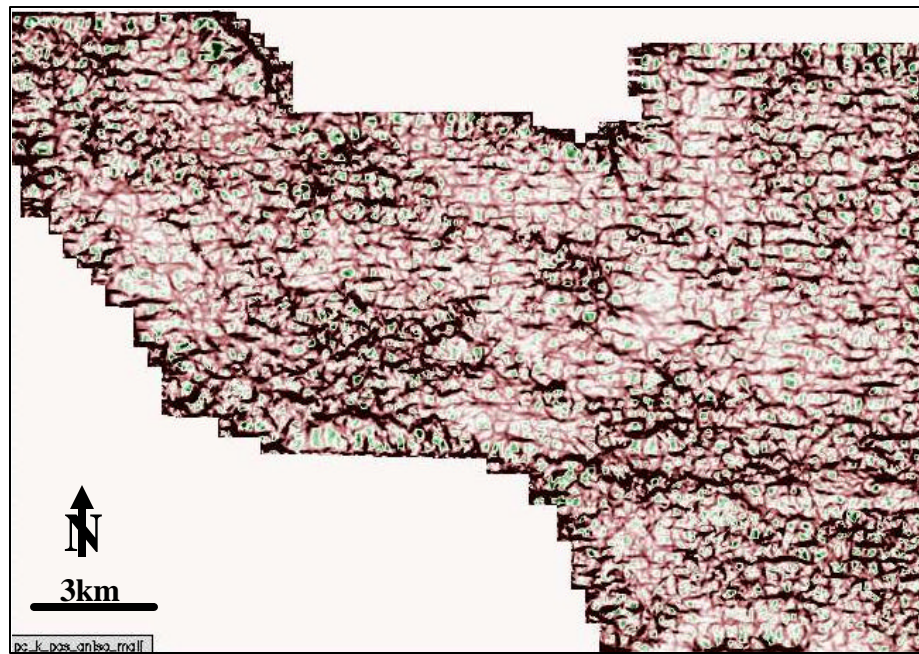


(b)

**FIG. 5.10.** Positive curvature at 700 ms: (a) isotropic and (b) anisotropic.

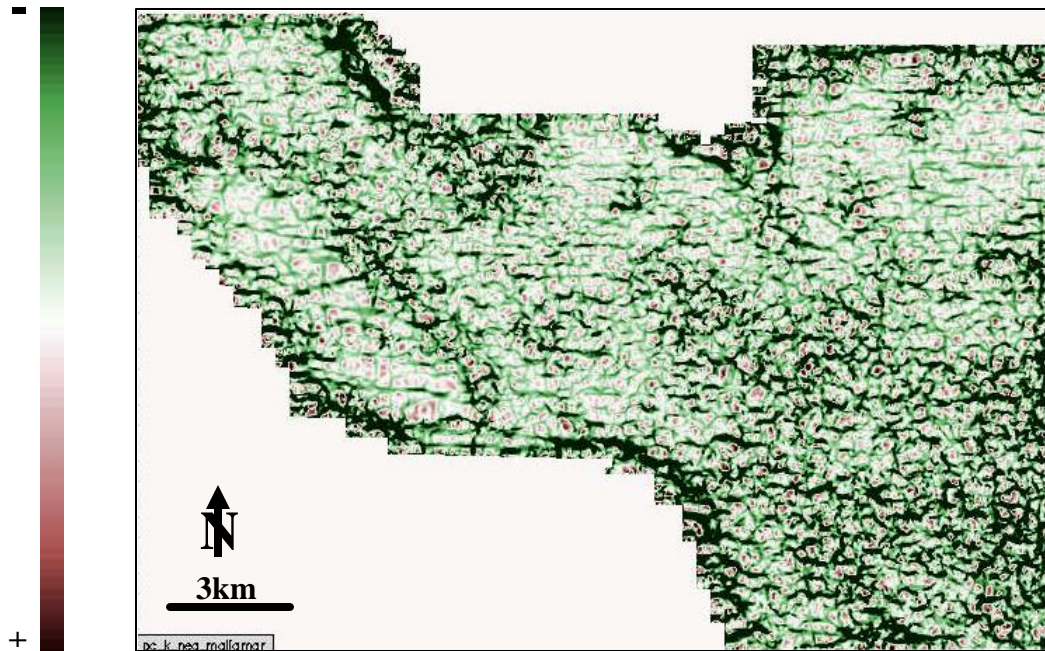


(a)

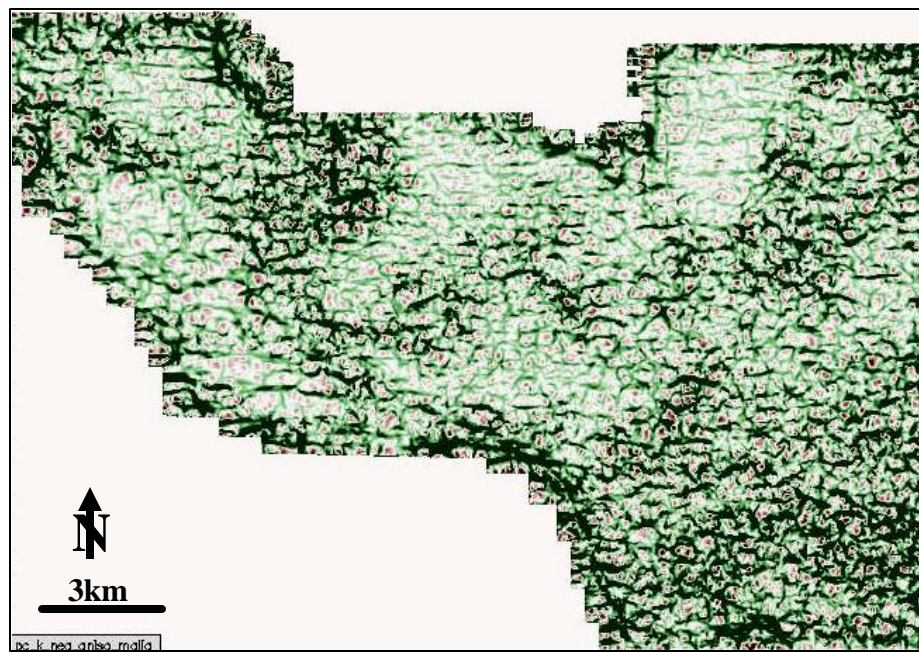


(b)

**FIG. 5.11.** Positive curvature at 800 ms: (a) isotropic and (b) anisotropic.

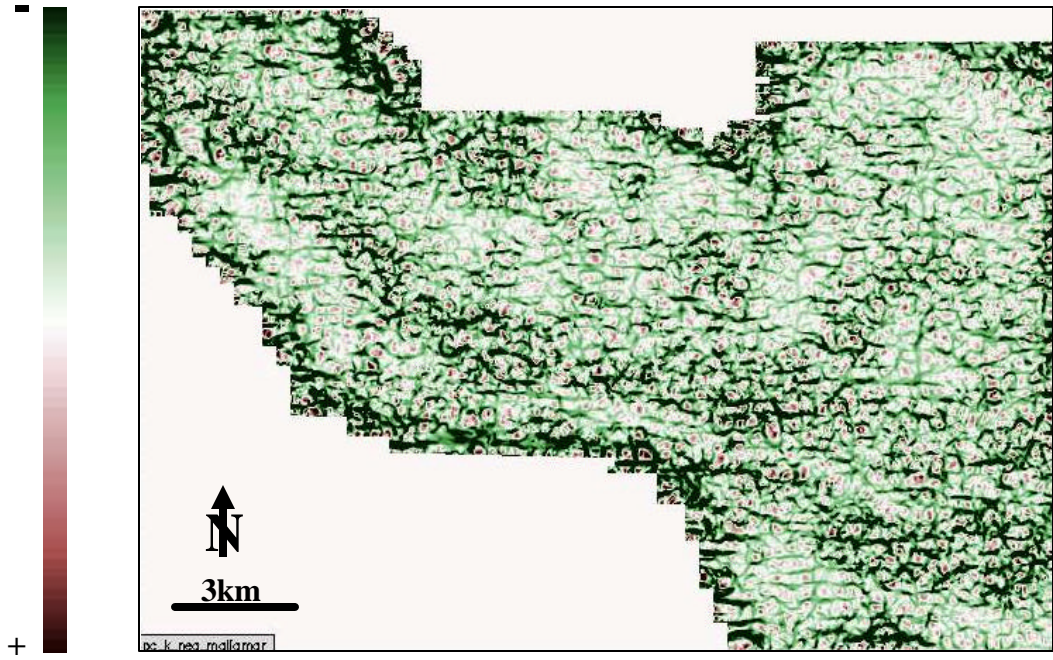


(a)

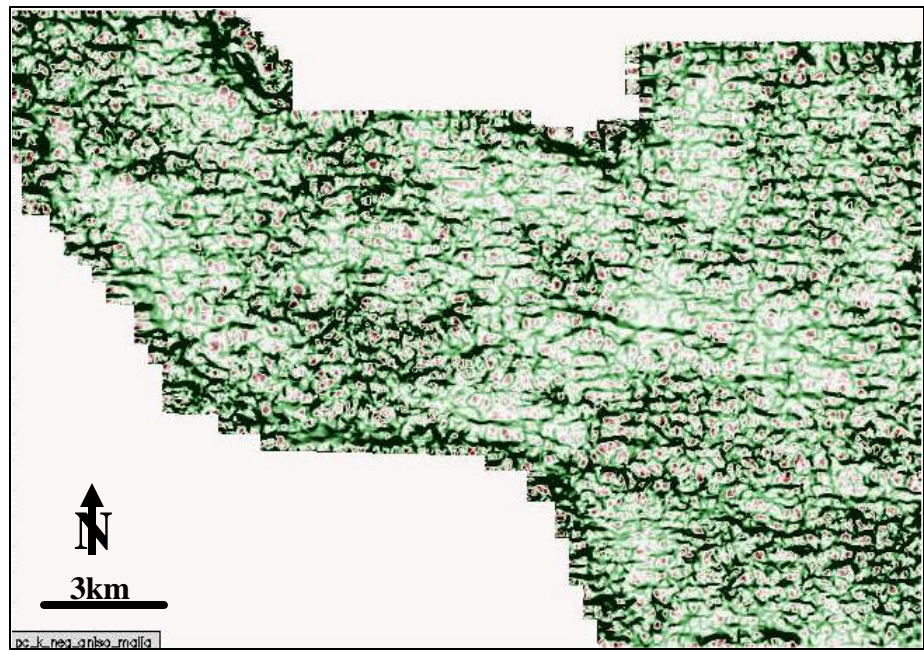


(b)

**FIG. 5.12.** Negative curvature at 700ms: (a) isotropic and (b) anisotropic.



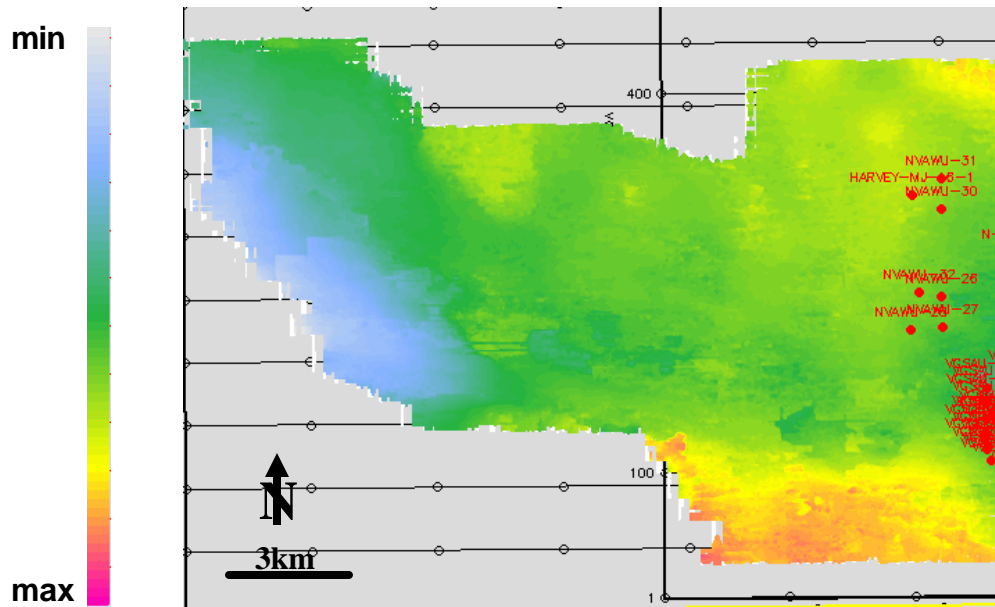
(a)



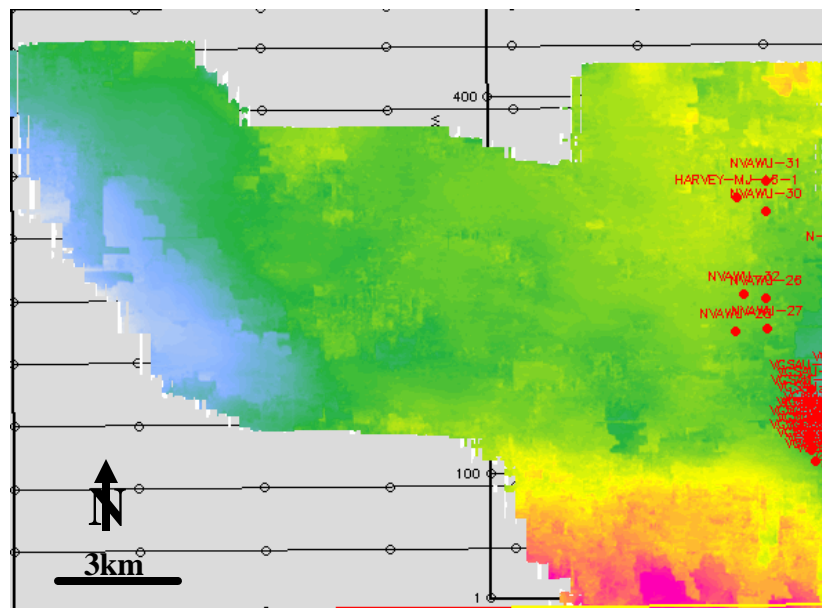
(b)

**FIG. 5.13.** Negative curvature at 800 ms: (a) isotropic and (b) anisotropic.

I chose one target time slice at 0.7-0.8 s called the Grayburg horizon, which is a relatively featureless horizon lining the platform. I interpreted the horizon on both volumes: isotropic and anisotropic, in order to compare the quality of resolution. Figures 5.14 to 5.16 display corresponding time/structure map of the horizon, horizon slice through amplitude and coherency along the horizon. Comparing isotropic (Figure 5.15a) and anisotropic (Figure 5.15b) volumes yield slightly large changes in amplitude. Including anisotropy leads to improved focusing and greater angles of incidence. By comparing the coherency slices, the anisotropy improves the resolution around the platform edge, highlights possibility of karst structures, and resolves channels, minor faults and fractures (Figure 5.16b).

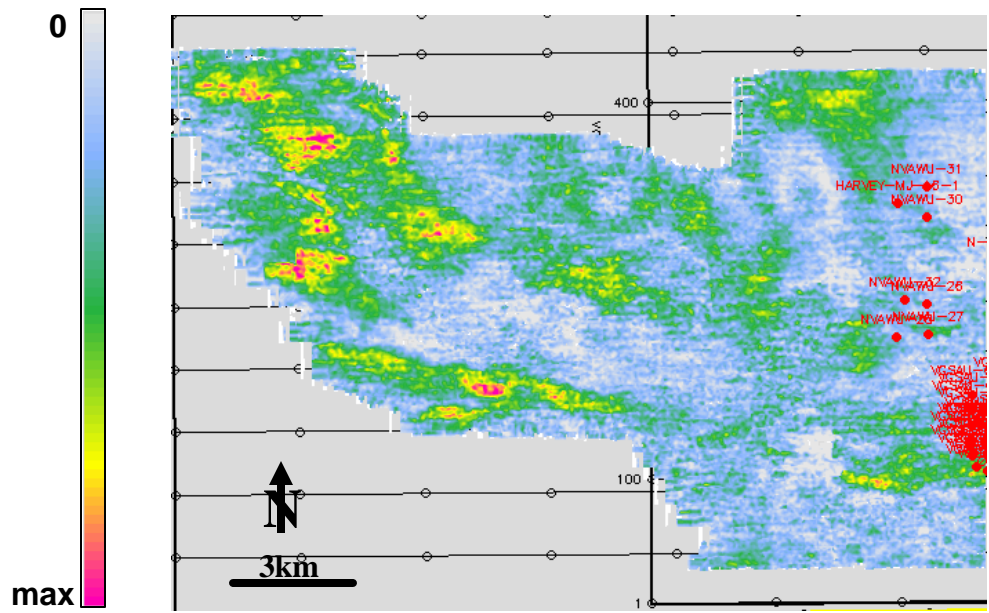


(a)

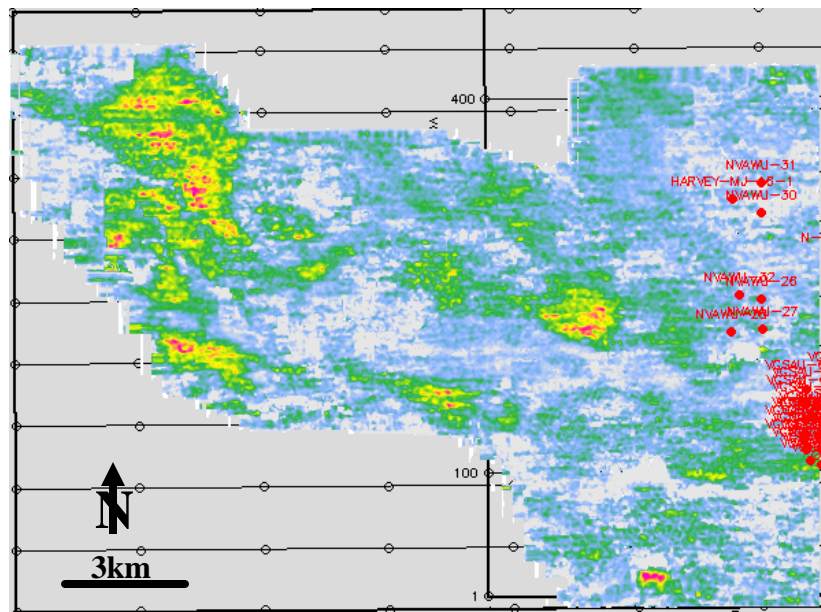


(b)

**FIG. 5.14.** Grayburg horizon time/structure map: (a) isotropic and (b) anisotropic.

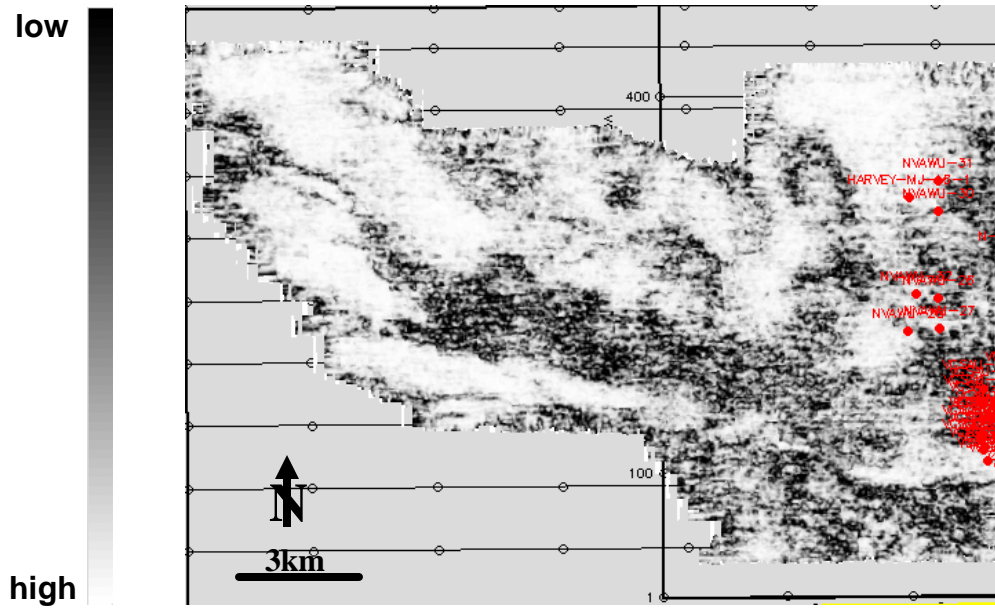


(a)

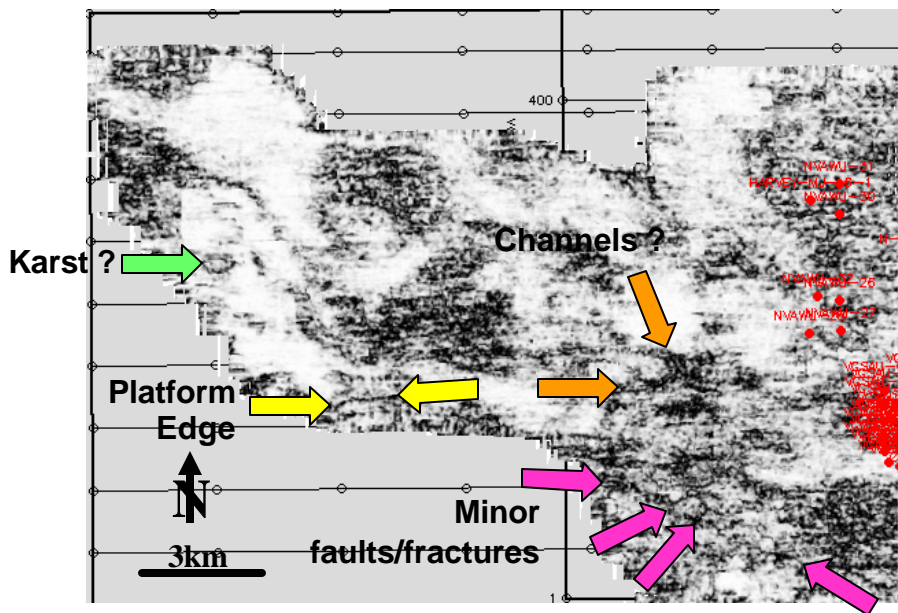


(b)

FIG. 5.15. Grayburg horizon slice through amplitude: (a) isotropic and (b) anisotropic.



(a)



(b)

FIG. 5.16. Grayburg horizon through coherency: (a) isotropic and (b) anisotropic.

## 6. RESULTS AND CONCLUSIONS

### 6.1. Results

The major result of accounting for anisotropy is to increase the fold of the data in the shallow target, thereby increasing the signal to noise ratio and the vertical and lateral resolution of the resulting image.

Processing and migration of 3-D land data demands a great deal of time, skill and patience. 3-D surveys often arrive without observer notes, information on previous processing flows, etc. Most of the man hours are spent on basic issues like: geometry QC, sorting, statics and evaluation of decon operators. One could spend a half their life on velocity picking and second half just picking eta. Most of the computer time is spent on dip moveout (DMO) and migration. A very patient MS candidate, with expert help, can indeed ‘master’ the processing of 3-D land data.

By accounting for transverse isotropy (TI), despite challenges, such as overcoming signal, incorporating anisotropy in the processing flow, I was able to increase the signal-to-noise ratio and reduce the amount of aliasing by including more traces in the migration stack. Including longer offset traces improved the velocity analysis and therefore and lateral resolution of the data. The data that I started with, significantly improved the quality, and I was able to detect some of the features that were not obvious on the isotropic result. The geological events on the vertical anisotropic sections became more accurate what I expected to see, knowing the structure of the area.

Seismic attributes show that an acquisition footprint is less subtle on the anisotropic than on the isotropic volume. Channels, platform edge, faults and fractures are also better focused with anisotropic processing. Velocity errors can result in creation of the false structure. Volumetric curvature is extremely sensitive to these false structures, which appear as another type of ‘acquisition footprint’, and can be used as a velocity QC tool.

The next step in improving these data set results is to run anisotropic pre-stack depth migration and compare the results with those presented in this work.

## REFERENCES

- Alkhalifah, T. and K. Larner, 1994, Migration error in transversely isotropic media: Geophysics, **59**, 1405-1418.
- Adams, J. E., 1965, Stratigraphic-tectonic development of Delaware Basin: AAPG Bulletin, **49**, 2140-2148.
- Alkhalifah, T. and I. Tsvankin, 1995, Velocity analysis for transversely isotropic media: Geophysics, **60**, 1550-1566.
- Acuna, C., 2000, 4D multicomponent seismic characterization of Glorieta-Paddock carbonate reservoir at Vacuum Field, New Mexico: MS Thesis, Colorado School of Mines, Golden, CO.
- Amaral, L.H., 2001, Shear wave azimuthal AVO analysis, Vacuum Field, New Mexico: MS Thesis, Colorado School of Mines, Golden, CO.
- Barry, K.M., D. A. Cavers, and C.W. Kneale, 1974, Recommended standards for digital tape formats, Digital tape standards, Society of Exploration Geophysicists.
- Blaylock, J.J., 1999, Interpretation of a baseline 4D multicomponent seismic survey at Vacuum Field, Lea County, New Mexico: MS Thesis, Colorado School of Mines, Golden, CO.
- Brittle, K., and L. Lines, 2001, Vibroseis deconvolution: an example from Pikes Peak, Saskatchewan: CSEG Recorder, **26**, no.5, 28-35.
- Bancroft, J. C., G.F. Margrave and H.D. Geiger, 1997: A kinematic comparisons of conventional processing, DMO-PSI, and equivalent offset migration (EOM): 67th

- Annual International Meeting Society of Exploration Geophysicists, Expanded Abstracts, 1575-1578.
- Canning, A. and G. H. F. Gardner, 1998, Reducing 3-D acquisition footprint for 3-D DMO and 3-D prestack migration: *Geophysics*, **63**, 1177-1183.
- Chopra, S., and K. J. Marfurt, 2006, 3-D seismic texture analyses, Society of Exploration Geophysicists.
- Chopra, S., G. Larsen, S. Pickford, 2000, Acquisition footprint- its detection and removal: *CSEG Recorder*, **14**, no.7, 16-20.
- Chopra, S., G., and S. Pickford, 2001, Acquisition footprint- its detection and removal: *CSEG Recorder*, **12**, no2, 5-8.
- Clinton, B., 2005, Staff Geophysicist, ConocoPhillips, Permian Oil Development, Personal communication.
- Cordsen, A., 2004, Acquisition Footprint Can Confuse: *AAPG Explorer*, March 2004.
- Castagna, J. P., S. Sun and R.W. Siegfried, 2003, Instantaneous spectral analysis: Detection of low-frequency shadows associated with hydrocarbons: *The Leading Edge*, **22**, 120-127.
- Chase, M. K., 1992, Random noise reduction by 3-D spatial prediction filtering: 62<sup>nd</sup> Annual International Meeting Society of Exploration Geophysicist, Expanded Abstracts, 1152-1153.
- DeVault, B., 1997, 3-D Seismic prestack multicomponent amplitude analysis, Vacuum Field, Lea County, New Mexico: PhD Thesis, Colorado School of Mines, Golden, CO.

- Focus Help, 2005, Paradigm Geophysical Proprietary Software, Houston, TX.
- Grimm, J., V. Aleksic, D. J. McVee. and S. R. Trickett, 2003, Prestack F-xy eigenimage noise suppression: Kelman Technologies Inc., Calgary.
- Galikeev, T., 2001, Pre-stack depth migration and attribute analysis of 3-D time-lapse P-wave data, Vacuum Field, Lea County, New Mexico: MS Thesis, Colorado School of Mines, Golden, CO.
- Garotta, R., 2000, Shear waves from acquisition to interpretation, Distinguished Instructor Series, Society of Exploration Geophysicists, Tulsa, OK, USA.
- Grechka, V., 2002, Multicomponent stacking-velocity tomography for TI media: *Geophysics*, **67**, 1564-1574
- Hill, S., M. Shultz and J. Brewer, 1999, Acquisition footprint and fold-of –stack plots: *The Leading Edge*, **18**, 686-695.
- Hills, J. M., 1984, Sedimentation, tectonism, and hydrocarbon generation in Delaware Basin, West Texas and Southeastern New Mexico: *AAPG Bulletin*, **68**, 250-267.
- Hileman, J., A. P. Embree and J. C. Pflueger, 1968, Automated static corrections: *Geophysical Prospecting*, **16**, 326-358.
- Issac, H. and D. Lawton, 1999, Image mispositioning due to dipping TI media: A physical seismic modeling study: *Geophysics*, **64**, 1230-1238.
- Isaac, H. and D. Lawton, 1997, Anisotropic physical modeling: *Foothills Research Report*, **3**, 15.1 – 15.26.
- Larner, K. and J. Cohen, 1993, Migration error in transversely isotropic media with linear velocity variation in depth: *Geophysics*, **58**, 1454-1467.

- Mavko, G., T. Mukerji, and J. Dvorkin, 1999, *The Rock physics handbook*: Cambridge University Press.
- Mattocks, B. W., 1998, *Borehole Geophysical Investigation of seismic anisotropy at Vacuum Field, Lea County, New Mexico*: PhD. Thesis, Colorado School of Mines, Golden, CO.
- Marfurt, K.J., R. M. Scheet, J. A. Sharp and M. G., Harper, 1998, Suppression of the acquisition footprint for seismic sequence attribute mapping: *Geophysics*, **63**, 1024-1035.
- Neidell, N.S., 1980, *Modern Methods of Seismic Data Processing*: Geoquest International, Inc., Houston.
- Neidell, N. S. and M. T. Taner, 1971, Semblance and other coherency measures for multichannel data: *Geophysics*, **36**, 482-497.
- Ota, S., 2001, *Integrated 3-D seismic analysis of Atoka Formation sandstone reservoirs, Vacuum Field vicinity, Lea County, New Mexico*: MS Thesis, Colorado School of Mines, Golden, CO.
- Pranter, M. J., N. F. Hurley, T. L. Davis, M. A. Raines and S. C. Wehner, 2004, Dual-lateral horizontal wells successfully target bypassed pay in the San Andres Formation, Vacuum Field, New Mexico: *AAPG Bulletin*, **88**, 99-113.
- Roberts, A., 2001, Curvature attributes and their application to 3D interpreted horizons, *First Break*, **19**, no.2, 85-99.
- Roche, S.L., 1997, *Time-lapse, multi-component, three-dimensional seismic characterization of a San-Andres shallow shelf carbonate reservoir, Vacuum Field, Lea County, New Mexico*: PhD Thesis, Colorado School of Mines, Golden, CO.

- Ronen, J. and J. F. Clarebout, 1985, Surface-consistent residual statics estimation by stack-power maximization: *Geophysics*, **50**, 2759-2767.
- Stein, S. and M. Wysession, 2003, *An introduction to seismology, earthquakes, and Earth structure*: Blackwell Publishing.
- Sherwood, J., W., C. and P. H. Poe, 1972, Continuous velocity estimation and seismic wavelet processing: *Geophysics*, **37**, 769-787.
- Sheriff, R., E., 2003, *Exploration Seismology: class notes for a Seismic Ray and Wave Theory course*, University of Houston, 51-54..
- Sheriff, R., E., 1984, *Encyclopedic Dictionary of Exploration Geophysics*: Society of Exploration Geophysicist, Tulsa, OK, USA.
- Taner, M.T., F. Koehler and R. E. Sheriff, 1979, Complex seismic traces analysis: *Geophysics*, **44**, 1041-1063.
- Thomsen, L., 1986, Weak elastic anisotropy: *Geophysics*, **51**, 1954-1966
- Thomsen, L., 2002, *Understanding seismic anisotropy in exploration and exploitation: Distinguished Instructor Series*, Society of Exploration Geophysicists, Tulsa, OK, USA.
- Talley, D.J., 1997, *Characterization of San Andres carbonate reservoir using four dimensional, multicomponent attribute analysis*: MS Thesis, Colorado School of Mines, Golden, CO.
- Taner, M.T., F. Koehler and K.A. Alhilali, 1974, Estimation and correction of near-surface time anomalies: *Geophysics*, **39**, 441-463.
- Taner, M.T., F. Koehler and K.A. Alhilali, 1969, Velocity spectra-digital computer derivation and applications of velocity functions: *Geophysics*, **34**, 859-881.

- Tsvankin, I., 2001, Seismic signatures and analysis of reflection data in anisotropic media: Handbook of Geophysical Exploration, Elsevier.
- Vestrum, R., D. Lawton and R. Schmidt, 1999, Imaging structures below dipping TI media: Geophysics, **64**, 1239-1246.
- Wiggins, R.A., K. L. Lerner and, R. D. Wisecup, 1976, Residual statics analysis as a general linear inverse problem: Geophysics, **41**, 922-938.
- Wehner, S. C., M. A. Raines, T. L. Davis and R. D. Benson, 2000, Dynamic reservoir characterization at Central Vacuum Unit: Society of Petroleum Engineers, 63134.
- Yilmaz, O., 2001, Seismic data analysis. Processing, Inversion and Interpretation of Seismic Data: Society of Exploration Geophysicists Series on Investigation in Geophysics, Tulsa, OK.
- Zheng, Y., S. Gray, S. Cheadle and P. Anderson, 2002, Factors Affecting AVO Analysis of Prestack Migrated Gathers: 64th Meeting European Association of Geosciences Engineers, G011.

## APPENDIX A: TRANSVERSE ISOTROPY-THEORETICAL BASIS

The wave equation is defined from the equation of motion and stress-strain relation to be:

$$\frac{\partial^2 u_i}{\partial t^2} = \frac{C_{ijmn}}{\mathbf{r}} \frac{\partial^2 u_m}{\partial x_n \partial x_j}. \quad (\text{A-1})$$

Hooke's Law assumes that each component of stress,  $t_{ij}$ , is linearly proportional to every component of strain,  $e_{mn}$ ,

$$t_{ij} = C_{ijmn} e_{mn}, \quad (\text{A-2})$$

where  $C_{ijmn}$  is the elastic tensor.

The elastic tensor,  $C_{ijmn}$ , completely characterizes the elasticity of the medium (Thomsen, 1986, 2002). The four indices of the elasticity tensor correspond to the two indices of stress and two indices of strain. Since stress and strain are symmetric, we can simplify our notation and rewrite the elastic tensor as a  $6 \times 6$  matrix  $C_{ab}$ , where:

<i>each index pair ij =</i>	11	22	33	23	13	12	
<i>maps into...</i>	↓	↓	↓	↓	↓	↓	
<i>a single index</i>	$\alpha = 1$	2	3	4	5	6	.

(A-3)

For an isotropic media, the components of the elastic tensor are related to Lamé's parameters  $\mathbf{l}$  and  $\mathbf{m}$ . For transverse isotropy (TI), the stress-strain matrix contains 5 independent elastic parameters:

$$C_{\alpha\beta} = \begin{pmatrix} C_{11} & C_{11}-2C_{66} & C_{13} & 0 & 0 & 0 \\ C_{11}-2C_{66} & C_{11} & C_{13} & 0 & 0 & 0 \\ 0 & 0 & 0 & C_{44} & 0 & 0 \\ 0 & 0 & 0 & 0 & C_{44} & 0 \\ 0 & 0 & 0 & 0 & 0 & C_{66} \end{pmatrix} \quad (A-4)$$

The solution of the wave equation for transverse isotropic media has three velocities dependent on the polarization with respect to the symmetry plane (one “P-velocity and two “S-velocities”) (Thomsen, 2002) (Figure A.1).

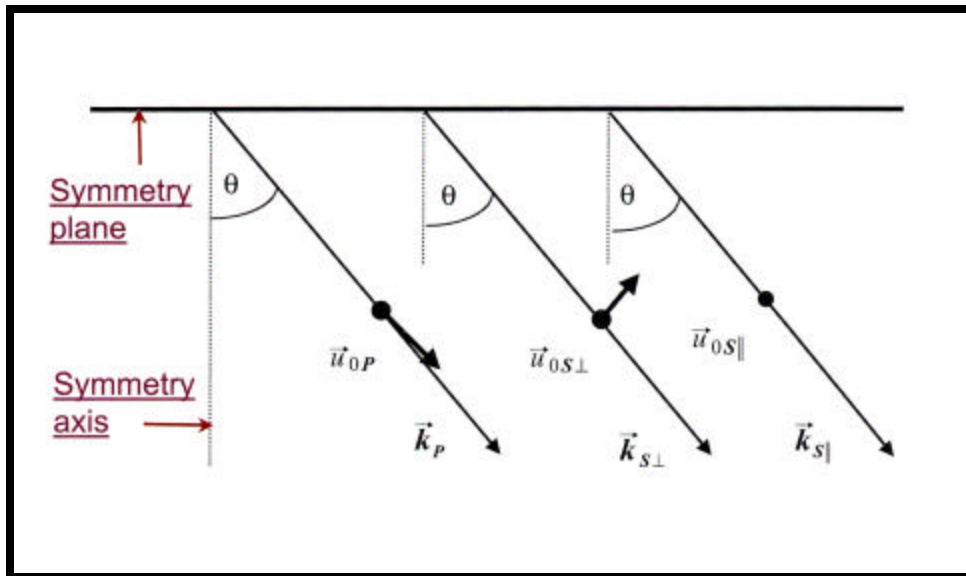


**FIG. A.1.** Every direction of propagation has a three wave types, mutually orthogonal, with different velocities (after Thomsen, 2002).

The five constants, in exploration seismology based on Thomsen (1986) work on weakly anisotropic media, are commonly called “Thomsen parameters”:

$$\mathbf{n}_p(0^\circ) = \sqrt{\frac{C_{33}}{\mathbf{r}}} = \mathbf{n}_{p\parallel}, \quad (\text{A-5})$$

$$\mathbf{n}_s(0^\circ) = \sqrt{\frac{C_{44}}{\mathbf{r}}} = \mathbf{n}_{s\parallel}, \quad (\text{A-6})$$

$$\mathbf{e} = (C_{11} - C_{33}) / 2C_{33}, \quad (\text{A-7})$$

$$\mathbf{d} = [(C_{13} + C_{44})^2 - (C_{33} - C_{44})^2] / 2C_{33}(C_{33} - C_{44}), \text{ and} \quad (\text{A-8})$$

$$\mathbf{g} = (C_{66} - C_{44}) / 2C_{44}, \quad (\text{A-9})$$

where,  $\mathbf{n}_p$  and  $\mathbf{n}_s$  are the velocities in the direction of the symmetry axis,  $\mathbf{e}$  is the horizontal P-wave anisotropy parameter,  $\mathbf{d}$  -near vertical P-wave polar anisotropy parameter and  $\mathbf{g}$  is S wave anisotropy in the direction of symmetry axis (S ||) (Sheriff, 2003). If we assume the anisotropy to be weak, Thomsen (1986) shows the velocities of plane waves traveling at the angle  $\mathbf{q}$  (polar angle) to the axis of symmetry to be:

$$V_p(\theta) = V_p(0^\circ) [1 + \mathbf{d} \sin^2 \theta + \mathbf{e} \sin^4 \theta], \quad (\text{A-10})$$

$$V_{s\perp}(\theta) = V_s(0^\circ) [1 + (V_{p0} / V_{s0})^2 (\mathbf{e} - \mathbf{d}) \sin^2 \theta \cos^2 \theta], \text{ and} \quad (\text{A-11})$$

$$V_{s\parallel}(\theta) = V_s(0^\circ) [1 + \mathbf{g} \sin^2 \theta]. \quad (\text{A-12})$$

Velocities in the direction perpendicular to the symmetry axis are:

$$V_p(90^\circ) = V_p(0^\circ)(1+e), \quad (\text{A-13})$$

$$V_{\underline{s}}(90^\circ) = V_s(0^\circ), \text{ and} \quad (\text{A-14})$$

$$V_{s\parallel}(90^\circ) = V_s(0^\circ)(1+?). \quad (\text{A-15})$$

From these equations (A-13 to A-15), we can derive  $e$  and  $g$  on the basis of velocities:

$$e = [V_p(90^\circ) - V_p(0^\circ)] / V_p(0^\circ), \text{ and} \quad (\text{A-16})$$

$$? = [V_{s\parallel}(90^\circ) - V_s(0^\circ)] / V_s(0^\circ). \quad (\text{A-17})$$

For weakly anisotropic media, 10-20 % (Garota, 2000), and for surface seismic acquisition the most interesting parameter is  $d$  because its contribution completely dominates the  $e$  contribution for quantifying anisotropy (Thomsen, 1986):

$$V_{p\text{nm}o} = V_p(0^\circ)(1+d). \quad (\text{A-18})$$

The  $V_{p\text{NM}O}$  is called the “short-spread” hyperbolic approximation moveout velocity, where all the rays are traveling nearly vertical. We can not actually detect the  $V_p$  or  $d$ , just  $V_{p\text{NM}O}$  from the surface data (Thomsen, 2002). Velocity anisotropy gives use deviations from hyperbolic moveout. Such hyperbolic velocity analysis is insufficient to recover the true vertical velocity,  $V_p(0^\circ)$  (Tsvankin and Thomsen, 1994).

I want to highlight the effect of long-spread, non-hyperbolic moveout ( $e?d$ ) in VTI where the offsets  $x > z$  are not muted as in conventional processing. The way to account for deviations from hyperbolic moveout is to add higher-order terms to the quadratic Taylor series for the squared traveltime. P-wave long-spread moveout in horizontally layered TI media can be expressed including the fourth-order term in the traveltime series:

$$t_x^2 = t_0^2 + x^2/V_{\text{nm}o}^2 + A_4 x^4, \quad (\text{A-19})$$

where the fourth order moveout term,  $A_4$ , is responsible for the magnitude of nonhyperbolic moveout.  $A_4$  can be expressed for P waves as:

$$A_{4, P} = -2\eta / (t_{P0}^2 V_{nmo}^4), \quad (A-20)$$

where  $V_{nmo} = V_p(0^\circ) \sqrt{1+d}$  is the NMO from horizontal reflection and  $\eta$  is the “anelipticity” parameter defined by Alkhalifah and Tsvankin (1995) as:

$$\eta = (e-d) / (1+2d). \quad (A-21)$$

The parameters previously mentioned,  $V_{nmo}$  and  $\eta$  are mainly responsible for the moveout in horizontal VTI media and sufficient to perform all conventional time-processing steps including prestack and poststack time migration (Tsvankin, 2005).

Nonhyperbolic moveout is not readily apparent on raw data, but it is very clear when the hyperbolic moveout on the near offsets has been removed. The shape of the moveout is commonly called a “hockey stick” because of its shape (Figure A.2) (Thomsen, 2002).

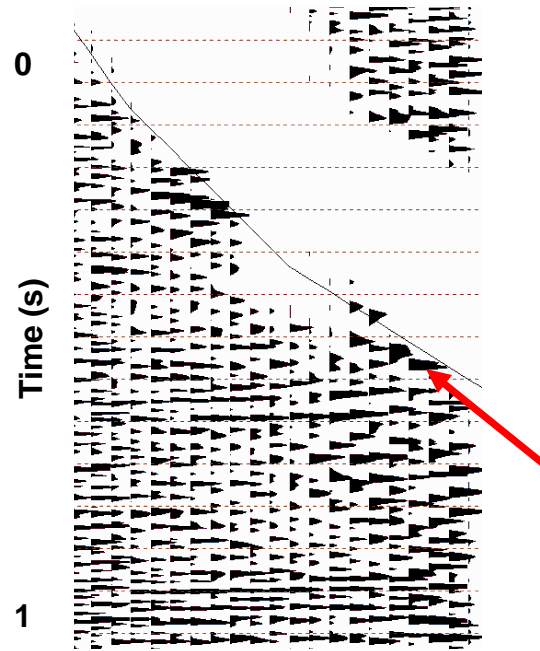
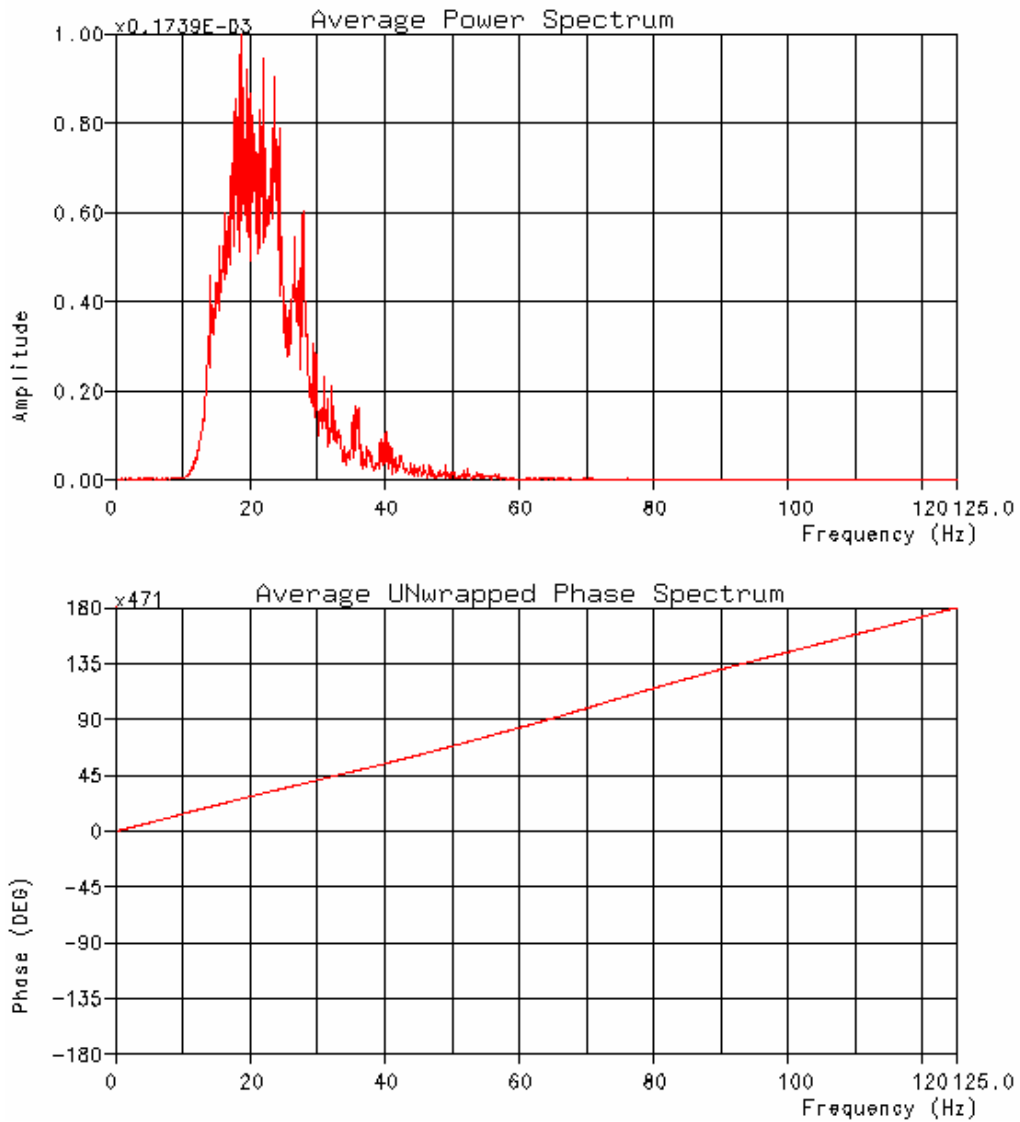


FIG. A.2. Hockey stick effect on the far offsets due to anisotropy.

## APPENDIX B: BASIC PARAMETERS USED

I have added this appendix so that others can reproduce, and hopefully, improve upon my processing flow. All screen captures are of Paradigm Geophysical's Proprietary Processing software "Focus".

Frequency content of the raw shot gather from Figure 2.1:



Surface consistent deconvolution using Focus program WSHAPE:

Parameters for WSHAPE:

- offset: 300
- WAVLEN: 2000
- WINLEN: 2000
- KEYDEF - Spatial Analysis Window Specification
  - PKEY: 2341
  - SKEYL: 0
  - SKEYH: 5882
- KEYDEF - Spatial Analysis Window Specification
 

SKEY	WSTART
[0]	778 882
[1]	1434 834
[2]	3068 990
[3]	5228 1162
[4]	5882 1356
- BUTTER - Butterworth Wavelet Parameters
  - PHASE: ZERO
  - FL: 10
  - SL: 18
  - FH: 60
  - SH: 36

Spectral balancing using Focus program SPEQ:

Parameters for SPEQ:

- AGCLEN: 500
- FGATES - Dimensions of Frequency Pass Bands
 

	L050	L00N	H10N	H150	REPEAT
[0]	5	10	20	25	1
[1]	20	25	30	35	1
[2]	30	35	40	45	1
[3]	40	45	50	55	1
[4]	50	55	60	80	1

F-xy filter (FXY) used for generation of pilot trace used in surface consistent statics:

62 FRMAX - Maximum frequency to include in the filter design

FXYDEC - Filter Design Specification

41	WINS	- Number of traces in design window (subline)
41	WINX	- Number of traces in design window (crossline)
5	FILS	- Number of traces in filter (subline)
5	FILX	- Number of traces in filter (crossline)
21	ADV5	- Number of traces for design window advance (subline)
21	ADVX	- Number of traces for design window advance (crossline)
800	WINT	- Design window length (ms)

SIGNAL - Location and Type of Data to Output

3	TYPE	- Type of data to output (SIGNAL/NOISE)
456	ISTLBL	- First CDPLBLS to output
4	LSTLBL	- Last CDPLBLS to output
666	ISTLBLX	- First CDPLBLX to output
0.1	LSTLBLX	- Last CDPLBLX to output
	ABF	- Fraction of unfiltered data added to filtered

Residual statics using Focus program STAT3D:

24 LIMIT - Maximum allowable static correction in ms (absolute value)

300000 WINDOW - Maximum number of traces to store in pilot buffer

LINE - Database line name

MSTAT NAME - Attribute name to identify statics stored in database

ALL FUNCT - Type of function calculated and stored (ALL/CORR/RST/STAT)

PILOT - Specify Pilot Trace Disk File

LABEL - Label of pilot trace file

Pilot for STAT3D

GATE - Define Correlation Time Gate(s)

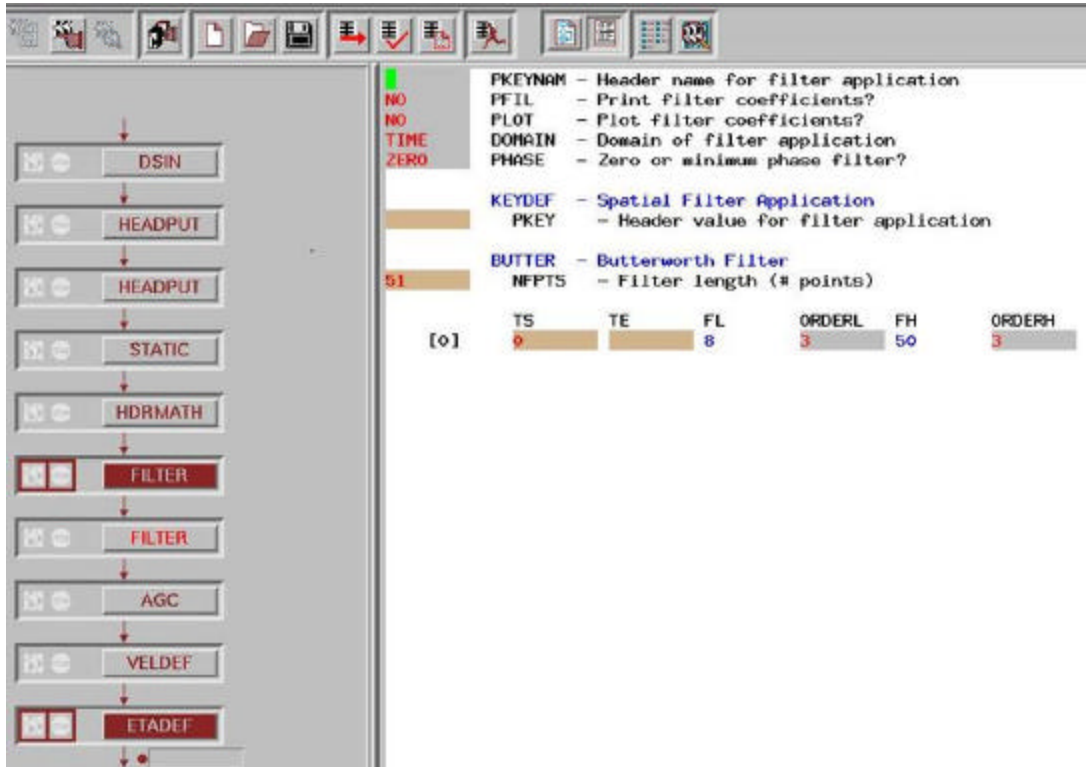
CDP PKEYNAM - Primary interpolation header name

	PKEYVAL	TSTART	TEND
[0]	1	800	2400

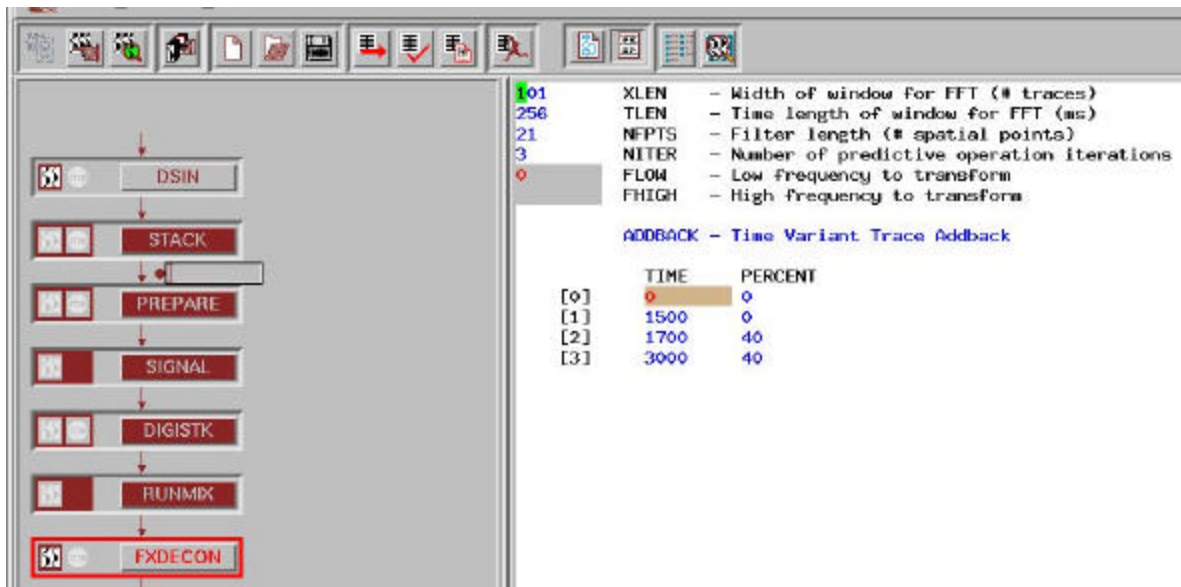
GROUP - Define Area to Compute Statics

3	FSUBLN	- Starting subline number for static computations
456	LSUBLN	- Ending subline number for static computations
4	FXLN	- Starting xline number for static computations
666	LXLN	- Ending xline number for static computations

Butterworth filter applied before velocity analysis. FL is low cut and FH high cut limit:



FXdecon:





Outside mute over offset of supergathers on the lower and upper parts of the gather in order to filter upper portion for picking ? (Figure 3.8a) :

The screenshot displays a software interface with a flowchart on the left and a parameter list on the right.

**Flowchart:**

- HDR/MATH
- REPEAT
- IF (diamond)
- SORT
- MUTE
- ELSEIF
- SORT
- MUTE
- MUTE
- MUTE
- MUTE
- MUTE
- STATIC
- RESAMP

**Parameter List:**

- OP
- OFFSET
- 200
- INT
- INT
- MUTE

**Definitions:**

- PKEYNAM - Primary header name for mute definition
- SKEYNAM - Secondary key name for mute definition
- RAMPLEN - Ramp length (ms)
- PKEYINT - Primary key interpolation (INT/NOINT)
- SKEYINT - Secondary key interpolation (INT/NOINT)
- MUTESW - Apply mute function?

**Options:**

- OFF - Inside or Trace End Muting
- PKEY - Primary header value

**Table:**

	SKEY	MTIME
[0]	155	482
[1]	9706	1684

**Options Overstrike**

Butterworth Filter applied prior to picking the anisotropy parameter, ?:

The screenshot displays a software interface with a flowchart on the left and a data table on the right. The flowchart starts with a 'REPEAT' block, followed by an 'IF' decision diamond. Below the 'IF' diamond, there are two paths: one leading to a 'SORT' block, then 'MUTE', and 'ELSEIF'; the other leading to another 'SORT' block, then 'MUTE', and three more 'MUTE' blocks. Both paths eventually lead to a 'STATIC' block and finally a 'RESAMP' block. At the bottom of the flowchart area are buttons for 'Copy', 'Move', 'Delete', 'Clear', 'Comment', and 'Undo'.

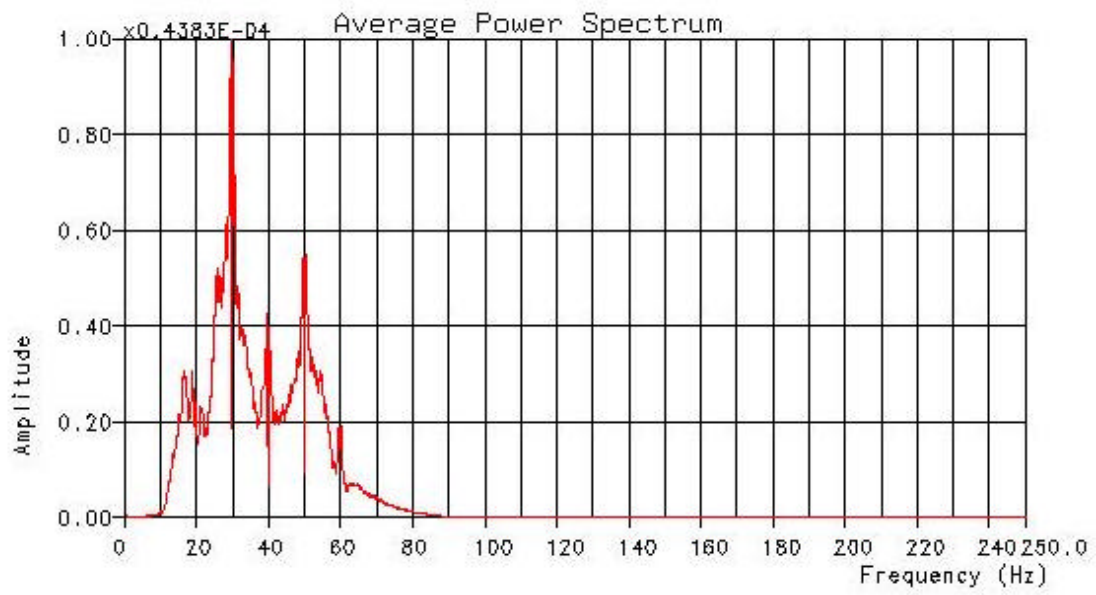
The data table on the right is titled 'BUTTER - Butterworth Filter' and lists parameters for filter application. The parameters are as follows:

	TS	TE	FL	ORDERL	FH	ORDERH
[0]	0		40	3	120	3

Additional parameters listed above the table include: PKEYNAM (Header name for filter application), PFIL (Print filter coefficients?), PLOT (Plot filter coefficients?), DOMAIN (Domain of filter application), PHASE (Zero or minimum phase filter?), and NFPTS (Filter length (# points)).

At the bottom right, there are 'Options' and 'Overstrike' labels, and a 'Help' section with 'KEYDEF - Spatial Filter Application' and 'BAND - Trapezoidal Filter'.

Frequency content of supergather according to whom the Butterworth range is established:



A representative list of (time, ?) pairs:

The screenshot displays a software interface with a flowchart on the left and a data table on the right. The flowchart consists of several steps: STATIC, RESAMP, ZMULT, KLTRANS, another STATIC, MUTE, FILTER, ENDIF, SORT, STACK, another SORT, and ETADEF. The data table on the right shows two 'HANDETA' entries, each with a list of parameters and a table of (TIME, ETA) pairs.

**Flowchart Steps:**

- STATIC
- RESAMP
- ZMULT
- KLTRANS
- STATIC
- MUTE
- FILTER
- ENDIF
- SORT
- STACK
- SORT
- ETADEF

**Data Table 1 (Line 30436):**

TIME	ETA
[0]	6 0
[1]	412 0.027
[2]	798 0.349
[3]	834 0.302
[4]	974 0.425
[5]	1584 0.022
[6]	2018 0.035
[7]	2316 0.042
[8]	2590 0.052
[9]	2998 0.044

**Data Table 2 (Line 30538):**

TIME	ETA
[0]	6 0
[1]	478 0.141
[2]	682 0.306

**Options:** Overstrike

**Help:** HANDETA - Stores a Time/Eta Table

**Insert:** HANDETA - Stores a Time/Eta Table

Isotropic and anisotropic migration parameters:

The screenshot displays the '3D Prestack TOTM' software interface with the following parameters and settings:

- CrossLine Output  Fine Internal Vertical Step
- Travel Time Approximation: **Hyperbolic**
- Anisotropy
- Geom. Weights  Offsets/Azimuths from DB
- Imaging Proofing Mode (Wavelet Based) **160 Hz**
- Stretch Filter Strength: **4 (medium)**
- Anti-Alias: **Triangular (Precise)** Strength: **4 (medium)**
- Target InLines: **1** - **464** Step: **1**
- Target CrossLines: **1** - **1034** Step: **1**
- Time [ms]: **0** - **3070** Step: **2.00**
- Apertures [ft]: InLine **10000** CrossLine **10000** At Time [ms] **1000**
- Maximum Input Offsets [ft]: InLine **10453** CrossLine **11000**
- Input Azimuth [deg]: **90** +/- **89**
- Create Output Gathers Target Lines Grouped by **1**
- Output Offsets [ft]: **0.0** - **12100.0** Step: **550.0**
- Miscellaneous: RAM [MB] **6000** CPUs **24** I/O Threads **1**
- Buttons: **Input File Info...** **Create Command Line...**
- Bottom Buttons: **OK** **Memory** **Can**

Running window filter (WNFILT):

The screenshot shows a seismic processing workflow in a software interface. The workflow consists of several steps: DSIN, RUNMIX, three HOLDIF blocks, WNFILT, SIGNAL, DSOUT, DIGISTK, RECALL, DSIN, and UNIFORM. The WNFILT block is highlighted in red. To the right of the workflow, a parameter list is displayed:

```
7 NTRACES - Number of traces in filter
ACROSS ENSESM - Lateral filtering within or across ensembles

FILTER - Filter Weight Parameters
repeats[0]
1 WEIGHT - Weight
repeats[1]
1 WEIGHT - Weight
repeats[2]
1 WEIGHT - Weight
repeats[3]
2 WEIGHT - Weight
repeats[4]
1 WEIGHT - Weight
repeats[5]
1 WEIGHT - Weight
repeats[6]
1 WEIGHT - Weight
```

Semblance weighted filter (DIGISTK):

The screenshot shows a seismic processing workflow in a software interface. The workflow consists of several steps: DSIN, SIGNAL, DIGISTK, and DSOUT. The DIGISTK block is highlighted in red. To the right of the workflow, a parameter list is displayed:

```
0.6 WT - Percentage of signal trace to combine with original trace
```

## SIGNAL

21

120	XGATE	- Gate width for correlation dip search (# traces)
-30	XINC	- Spatial gate moveup (# traces)
50	TGATE	- Time length of correlation dip search gate (ms)
5	TINC	- Time gate moveup (ms)
0.1	DIPMIN	- Minimum dip in dip scan (ms/XGATE traces)
0	DIPMAX	- Maximum dip in dip scan (ms/XGATE traces)
	DIPINC	- Dip increment in dip scan (ms/trace)
	MINCOH	- Minimum coherency
	LFILT	- Low frequency filter

## Signal Balancing:

SEONO  
TRACE  
SDECON  
MIN  
0.1

1

	PKEYNAM	- Primary interpolation header name
	SKEYNAM	- Secondary interpolation header name
	METHOD	- Method for wavelet estimation (TRACE/ENSEMBLE)
	OPER	- Type of operation (SDECON/PHACNV)
	PHASE	- Phase of the input wavelet (MIN/ZERO)
	WNOISE	- Percentage of white noise to be added
	<b>KEYDEF - Define Analysis Windows</b>	
	PKEY	- Primary interpolation key value
[0]	SKEY	TSTART TEND
	1	

## Band- Pass Filter:

PKEYNAM - Header name for filter application  
 NO  
 NO  
 TIME  
 ZERO  
 PFIL - Print filter coefficients?  
 PLOT - Plot filter coefficients?  
 DOMAIN - Domain of filter application  
 PHASE - Zero or minimum phase filter?  
 KEYDEF - Spatial Filter Application  
 1 PKEY - Header value for filter application  
 BAND - Trapezoidal Filter  
 BP  
 HANN  
 TYPE - Type of band filter  
 TAPER - Filter taper type  
 NFPTS - Filter length (# points)  
 TS TE F1 F2 F3 F4  
 [0] 0 6 12 48 72

F-xy filter:

62 FRMAX - Maximum frequency to include in the filter design  
 FXYDEC - Filter Design Specification  
 41 WINS - Number of traces in design window (subline)  
 41 WINX - Number of traces in design window (crossline)  
 5 FILS - Number of traces in filter (subline)  
 5 FILX - Number of traces in filter (crossline)  
 21 ADVS - Number of traces for design window advance (subline)  
 21 ADVX - Number of traces for design window advance (crossline)  
 800 WINT - Design window length (ms)  
 SIGNAL  
 1  
 464  
 1  
 650  
 OUTPUT - Location and Type of Data to Output  
 TYPE - Type of data to output (SIGNAL/NOISE)  
 1 ISTLBS - First CDPLBS to output  
 464 LSTLBS - Last CDPLBS to output  
 1 ISTLBLX - First CDPLBLX to output  
 650 LSTLBLX - Last CDPLBLX to output  
 ABF - Fraction of unfiltered data added to filtered data

Display for all the plots is used with 30 traces per inch and 3 inches per second.